LRP 555/96 September 1996

Invited and Contributed Papers
presented at the

**Joint Varenna-Lausanne International Workshop on "Theory of Fusion Plasmas" Varenna, Italy, August 26 - 30, 1996**

by the Theory Group

LIST OF CONTENTS

# Linear Study of Global Microinstabilities using Spectral and PIC methods.

S.Brunner, M.Fivaz, J.Vaclavik, K.Appert, T.M.Tran

Centre de Recherches en Physique des Plasmas
Association Euratom - Confédération Suisse
Ecole Polytechnique Fédérale de Lausanne
PPB – CH-1015 Ecublens/Switzerland

## Abstract

A spectral as well as a time evolution PIC code are presently being developed to solve the linearized gyrokinetic equations for studying global microinstabilities in toroidal geometry. In many ways these two methods are complementary and therefore allow for valuable cross-checking and validation of the different approximations made. This parallel approach forms a firm basis for future studies of non-linear evolution or higher dimensional systems.

## 1 Introduction

As a candidate for explaining anomalous transport in fusion devices, microinstabilities have been a field of extensive experimental and theoretical investigations. Particular interest is given to ion-temperature-gradient-driven (ITG or $\eta_i$) modes as they seem to play an important role in ion confinement. Over the past, investigations of this type of instabilities have considered increasingly complex systems. Starting with linear studies and reduced dimensions such as local dispersion relations [1]-[2] and ballooning representation [3]-[7], the basic understanding of slab- and toroidal-ITG instabilities was established. At present computational power allows for non-linear gyrofluid and gyrokinetic simulations [8]-[11] but which are still limited to flux tubes (radially local) or small configurations.

So even today linear studies are not outdated. For non-linear codes they allow valuable benchmarking of the linear stage of evolution and can provide information on possible channels of energy release and absorption. Furthermore, a linear calculation is the first systematic approach when considering additional physical effects such as non-adiabatic electrons, toroidal flow, reversed shear or shaping of equilibrium. Finally, linear codes are a useful tool for defining marginal stability.

Various studies have been performed on linear modes in toroidal systems for high toroidal wave numbers using ballooning representation (radially local). However the only published results on true global linear microinstabilities are based on one code by Marchand, Tang and Rewoldt [12]-[13] which is valid to second order in finite banana orbit width and contains no finite Larmor radius (FLR) effects. We have therefore undertaken

the development of two new global linear codes using respectively a spectral and a time evolution particle in cell (PIC) approach for solving gyrokinetic equations (GKE).

PIC and spectral methods are complementary in many ways. Pushing algorithms are basically straightforward and can therefore relatively easily be extended to more complicated problems such as realistic geometries and non-linear studies. But in linear runs, time evolution simulations provide only the highest growing mode and therefore can be considered as the practical approach to such a problem. Furthermore they can be limited with respect to short time scales. On the other hand, an eigenvalue calculation is naturally restricted to linear studies and needs more modeling to solve, so that simpler systems are usually considered. But spectral codes provide the full spectrum (at least the unstable modes) and can therefore be viewed as the analytical approach to a linear problem. Short time scales are no restriction in this case. This complementarity is useful for benchmarking: Asymptotically in time, the frequency, growth rate and field structure given by the time evolution PIC code must converge to the eigenfrequency and eigenmode relative to the highest growth rate of the spectrum. In this way, the limits of the different approximations can be defined. In addition, this complementarity allows one to cover a wider parameter space and give more information on a same problem.

The spectral approach is presented in Sec.II. The PIC method is briefly described in Sec.III and more extensively by Fivaz et.al. in these proceedings [14]. Results of comparisons and parameter scans are shown in Sec.IV.

# 2 Spectral Approach

Let us give a brief description of how the eigenvalue equation is derived keeping full FLR effects by using gyrokinetic theory.

## 2.1 Linearized, Electrostatic Gyrokinetic Equation

A collisionless plasma is considered. The linearized Vlasov equation for the fluctuating part $\tilde{f}(\vec{r},\vec{v},t)$ of the particle distribution function reads:

$$\left.\frac{D}{Dt}\right|_{u.t.p.} \tilde{f} = \left[\frac{\partial}{\partial t} + \vec{v}\cdot\frac{\partial}{\partial \vec{r}} + \frac{q}{m}(\vec{v}\times\vec{B})\cdot\frac{\partial}{\partial \vec{v}}\right]\tilde{f} = \frac{q}{m}\nabla\phi\cdot\frac{\partial}{\partial \vec{v}}F_M, \qquad (1)$$

where $\phi$ is the electrostatic (ES) potential of the perturbation, $\vec{B}$ the magnetic field of equilibrium and $F_M$ the local Maxwellian distribution with temperature $T$ and density $N$. $\left.\frac{D}{Dt}\right|_{u.t.p.}$ stands for the total time derivative along the unperturbed trajectories of the particles.

In typical fusion plasmas, the Larmor radius $\lambda_L$ is small compared with the characteristic length $a$ of equilibrium. When studying microinstabilities, Eq.(1) can then be transformed approximately using an expansion with respect to $\epsilon = \lambda_L/a \ll 1$ to the

linearized GKE [15]:

$$\left.\frac{D}{Dt}\right|_{u.t.G.C.} \tilde{g}= \left(\frac{\partial}{\partial t}+ \vec{v}_g \cdot\frac{\partial}{\partial \vec{R}}\right) \tilde{g}= -i\frac{q}{T}F_M(\omega-\omega^\star) < \phi >, \qquad (2)$$

where $\tilde{g}=\tilde{f} +\frac{q}{T}\phi F_M$ is the non adiabatic part of $\tilde{f}$, $< \phi >$ the gyro-averaged potential, $\omega^\star$ the diamagnetic drift frequency, and $\omega$ the frequency of perturbation. Eq.(2) is written in gyrokinetic variables $(\vec{R}, E, \mu, \alpha, \mathrm{sign}(v_\parallel))$, with $\vec{R}=\vec{r} +\frac{\vec{v}\times\vec{e}_\parallel}{\Omega}$ the guiding center (GC), $E=\frac{1}{2}v^2$ the kinetic energy, $\mu=\frac{1}{2}\frac{v_\perp^2}{B}$ the magnetic moment, and $\alpha$ the gyroangle. Although one solves for the particle distribution function, the GKE has taken full advantage of guiding center theory as $\left.\frac{D}{Dt}\right|_{u.t.G.C.}$ stands for the total time derivative along the unperturbed trajectories of the guiding centers. The effects of density and temperature gradients appear through the diamagnetic drift frequencies $\omega_n$ and $\omega_T$ respectively:

$$\omega^\star \sim \omega_n + \omega_T.$$

To be able to perform explicitly the gyro-averaging of the unknown potential $\phi$, one uses the Fourier transformation:

$$\phi(\vec{r}) = \int d\vec{k}\; e^{i\vec{k}\cdot\vec{r}}\; \hat{\phi}\,(\vec{k}),$$

so that

$$< \phi >= \int d\vec{k}\; e^{i\vec{k}\cdot\vec{R}}\; \hat{\phi}\,(\vec{k})\frac{1}{2\pi}\int_0^{2\pi} d\alpha\; e^{-i\vec{k}\cdot\frac{\vec{v}\times\vec{e}_\parallel}{\Omega}} = \int d\vec{k}\; J_0\left(\frac{k_\perp v_\perp}{\Omega}\right) e^{i\vec{k}\cdot\vec{R}}\; \hat{\phi}\,(\vec{k}), \qquad (3)$$

where the Bessel function $J_0(k_\perp\lambda_L)$ contains the full FLR effects. For this reason, Fourier representation is intrinsic to gyrokinetic theory.

Eq.(2) is solved by integrating along the unperturbed trajectories of the GC:

$$\tilde{g}\,(\vec{R}, E, \mu, \sigma; \omega) = \frac{q}{T}\int d\vec{k}\; J_0(k_\perp v_\perp/\Omega) e^{i\vec{k}\cdot\vec{R}}\; \hat{\phi}\,(\vec{k})(\omega^\star-\omega)F_M\, i\,\mathcal{P}(\vec{R}, \vec{k}, E, \mu, \sigma; \omega),$$

$$\begin{cases} \frac{d}{d\tau}\vec{R}'=\vec{v}_g\,(\vec{R}'; E, \mu, \sigma) = v_\parallel\,\vec{e}_\parallel + \vec{v}_d= v_\parallel\,\vec{e}_\parallel +\frac{1}{\Omega}\left(\frac{v_\perp^2}{2}+v_\parallel^2\right)(\nabla\times\vec{e}_\parallel)_\perp, \\ \vec{R}'\,(\tau=0) =\vec{R}\,. \end{cases}$$

For a given system, solving the GKE thus consists essentially in calculating the propagator

$$\mathcal{P} = \int_{-\infty}^{0} d\tau e^{i\left[\vec{k}\cdot(\vec{R}'-\vec{R})-\omega\tau\right]}, \qquad (4)$$

which in particular contains all resonances.

## 2.2 The Eigenvalue Equation

For low frequency ES microinstabilities, the system is closed invoking quasineutrality:

$$\sum_{\text{species}} \tilde{\rho}_q\,(\vec{r},\omega) = 0. \qquad (5)$$

The charge density $\tilde{\rho}_q$ is evaluated from $\tilde{g}$ after transforming back to particle variables and integrating over velocity space:

$$\tilde{\rho}_q(\vec{r},\omega) = \frac{q^2}{T}\left[-N\phi(\vec{r}) + \int d\vec{k}\; e^{i\vec{k}\cdot\vec{r}}\;\hat{\phi}(\vec{k})(\omega^\star-\omega)\int d\vec{v}\; J_0^2(k_\perp v_\perp/\Omega)F_M\, i\mathcal{P}(\omega)\right], \tag{6}$$

where the gyroangle integration has already been performed, producing a second Bessel function $J_0$, so that $d\vec{v}= 2\pi v_\perp dv_\perp dv_{||}$.

Eq.(5) defines an eigenvalue problem for the ES potential: One must find the frequencies in the complex $\omega$-plane for which there exists a non trivial solution $\phi$.

Note that in (6) $\phi$ appears in configuration space as well as in Fourier representation. By transforming back to space the eigenvalue problem reads:

$$\int d\vec{r'}\,\mathcal{K}(\vec{r},\vec{r'};\omega)\phi(\vec{r'}) = 0, \tag{7}$$

which is of integral type and therefore contains boundary and regularity conditions. It can be shown that the kernel $\mathcal{K}$ has an integrable singularity at $\vec{r}=\vec{r'}$ that must be handled carefully. Eq.(7) was solved for a cylindrical system using finite elements. After appropriate transformations [16], the singularity is integrated analytically. This method however cannot be extended to toroidal systems.

This problem was avoided by writing the quasineutrality equation in Fourier representation:

$$\sum_{\vec{k'}} \hat{\mathcal{K}}(\vec{k},\vec{k'},\omega)\,\hat{\phi}(\vec{k'}) = 0.$$

As the system is finite, notice that Fourier series instead of a Fourier transform was employed so that $(\vec{k},\vec{k'})$ naturally take discrete values. The main advantage of this representation is that there is no singularity at $\vec{k}=\vec{k'}$.

Formally the spectral problem can always be written in vectorial form:

$$\overleftrightarrow{\mathcal{K}}(\omega)\,\vec{\phi} = 0.$$

To find the spectrum of the system, one must solve the characteristic equation

$$\det \overleftrightarrow{\mathcal{K}}(\omega) = 0.$$

This is not a standard eigenvalue problem as the frequency dependence of $\overleftrightarrow{\mathcal{K}}$ is not simply linear. In practice, first estimates were obtained by either performing a scan of $\det\overleftrightarrow{\mathcal{K}}$ over the complex $\omega$-plane or eigenvalues were localized within a closed curve invoking Niquist theorem, i.e. taking advantage of the analyticity of $\det\overleftrightarrow{\mathcal{K}}$. These results were then refined using a Newton algorithm.

## 2.3 Toroidal Model for ITG Instabilities

A large aspect ratio, circular cross-section torus with major radius $R$ and minor radius $a$ is considered. The magnetic field of equilibrium can then be written

$$\vec{B}= B_0\frac{R}{r}\left(\vec{e_\varphi} - \frac{\rho}{Rq_s}\vec{e_\theta}\right),$$

$(\rho,\theta,\varphi)$ being the toroidal variables, $(r,\varphi,z)$ the cylindrical variables, and $q_s(\rho)$ the safety factor. In cylindrical variables the potential can be Fourier decomposed as follows:

$$\phi(\rho,\theta,\varphi;t) = e^{i(n\varphi-\omega t)}\sum_{(k,m)}\hat{\phi}_{(k,m)}\, e^{i(\kappa\rho+m\theta)},$$

where $n$ is the fixed toroidal wave number, $(k,m)$ the radial and poloidal wave numbers respectively. A local wave vector is then given by

$$\vec{k}= \kappa\,\vec{e_\rho} + \frac{m}{\rho}\,\vec{e_\theta} + \frac{n}{R}\,\vec{e_\varphi}, \qquad \kappa = k\frac{2\pi}{\Delta\rho},$$

with $\Delta\rho$ being the radial width of the annulus over which the eigenmodes are solved for in the poloidal plane.

As ITG instabilities are essentially driven by passing particles, for simplicity, only circulating particles are considered and furthermore are approximated as highly passing, i.e. the modulation of parallel velocity along the trajectories due to the variation of the magnitude of $\vec{B}$ is neglected. This was validated by PIC results when trapped particle effects could be neglected i.e. for large aspect ratio systems or for frequencies above the average bounce frequency. Under these assumptions the derivation of the propagator (Eq.(4)) leads to

$$\mathcal{P} = \sum_{p,p'=-\infty}^{+\infty} e^{i(p-p')(\theta+\theta_{\vec{k}})}\frac{J_p(k_\perp v_{dz}/\omega_t)J_{p'}(k_\perp v_{dz}/\omega_t)}{i(k_\parallel v_\parallel - p\omega_t - \omega)},$$

where $v_{dz} = \frac{1}{\Omega}\left(\frac{v_\perp^2}{2}+v_\parallel^2\right)\frac{1}{R}$ are the vertical toroidal drifts and $\theta_{\vec{k}} = \arg(k_\theta - i\kappa)$. Note the possible resonances with respect to the harmonics of the transit frequency $\omega_t = \frac{v_\parallel}{Rq_s}$.

Assuming adiabatic electrons and only one species of singly charged ions, the two-dimensional eigenvalue problem in Fourier space becomes:

$$\sum_{(k',m')}\hat{\mathcal{K}}_{(k,m);(k',m')}(\omega)\,\hat{\phi}_{(k',m')} = 0,$$

$$\begin{aligned}\hat{\mathcal{K}}_{(k,m);(k',m')}(\omega) &= \frac{1}{\Delta\rho}\int_{\rho_l}^{\rho_u} d\rho e^{-i(k-k')\frac{2\pi}{\Delta\rho}\rho}\left[\alpha_c(1+\frac{T_e}{T_i})\delta_m^{m'} + \right.\\ &\left.\frac{T_e}{T_i}(\omega-\omega^\star)e^{i(m-m')\theta_{\vec{k}}}\frac{1}{\sqrt{2\pi}}\int_{-\infty}^{+\infty}dv_\parallel e^{-\frac{1}{2}v_\parallel^2}\sum_p\frac{I(\rho,k_\perp,v_\parallel,p,p'=p-m+m')}{k_\parallel v_{th}v_\parallel - p\omega_t - \omega}\right],\end{aligned}$$

$$I(\rho,k_\perp,v_\parallel,p,p') = \int_0^{v_{\perp c}(\rho,v_\parallel)} v_\perp dv_\perp e^{-\frac{1}{2}v_\perp^2}J_0^2(\xi_L)J_p(\xi_b)J_{p'}(\xi_b),$$

with $\alpha_c$ the fraction of circulating particles. For each frequency the matrix must be recomputed, which implies for each matrix element $\hat{\mathcal{K}}_{(k,m);(k',m')}$ a radial Fourier transform, a parallel velocity integral, and a sum over harmonics of the transit frequency. The perpendicular velocity integrals $I$ can be precalculated and contain all FLR effects through $\xi_L = k_\perp \lambda_L$, and finite banana width effects through $\xi_b = k_\perp \lambda_b = k_\perp \lambda_L q_s \left(\frac{v_\perp^2}{2} + v_\parallel^2\right) \frac{1}{v_\parallel}$.

The code is run on a Silicon Graphics Indigo2. Average input parameters are approximately 80 radial mode numbers, 10 poloidal mode numbers, 10 harmonics of transit frequency, 60 integration points in each velocity direction. A frequency scan of the order of 1000 values of $\omega$ presently takes $\sim$ 15 hours.

# 3 Time Evolution Approach

## 3.1 Initial System of Equations

To avoid the numerically noisy time derivative in the right hand side of Eq.(2), the equation taken here for the particle dynamics is slightly different, following a derivation by Hahm [17]. In this case one solves for the distribution function of the GC $\tilde{f}_g\,(\vec{R}, v_\parallel, v_\perp; t)$:

$$\left.\frac{D}{Dt}\right|_{u.t.G.C.} \tilde{f}_g = \left[\frac{\partial}{\partial t} + \vec{v}_g \cdot \frac{\partial}{\partial \vec{R}} + \frac{dv_\parallel}{dt}\frac{\partial}{\partial v_\parallel} + \frac{dv_\perp}{dt}\frac{\partial}{\partial v_\perp}\right] \tilde{f}_g = T_{RHS}, \tag{8}$$

with

$$\begin{cases} \frac{d}{dt}\vec{R} &= \vec{v}_g \\ \frac{d}{dt}v_\parallel &= \frac{1}{2}v_\perp^2 \nabla\cdot \vec{e}_\parallel \\ \frac{d}{dt}v_\perp &= -\frac{1}{2}v_\perp v_\parallel \nabla\cdot \vec{e}_\parallel, \end{cases}$$

and

$$T_{RHS} = \left\{ \frac{<\vec{E}> \times \vec{B}}{B^2} \cdot \frac{\partial}{\partial \vec{R}} + \frac{e}{m} < E_\parallel > \frac{\partial}{\partial v_\parallel} + < \vec{E} > \cdot \frac{\vec{B} \times \nabla \ln B}{B^2} \left[\frac{v_\perp}{2}\frac{\partial}{\partial v_\perp} + v_\parallel \frac{\partial}{\partial v_\parallel}\right] \right\} F_M.$$

Velocity variables $(v_\parallel, v_\perp)$ are adopted to avoid singularities in the Jacobian when performing integrals over velocity space using $(\epsilon, \mu)$. The system is again closed invoking quasineutrality:

$$\frac{eN}{T_e}\phi(\vec{r},t) = \int d\vec{v}\; d\vec{R}\, \tilde{f}_g\,(\vec{R}, v_\parallel, v_\perp; t)\delta(\vec{R} + \vec{\lambda_L} - \vec{r}) - \nabla_\perp \frac{eN}{m\Omega^2}\nabla_\perp \phi(\vec{r},t), \tag{9}$$

where the left hand side is the density of the adiabatic electrons and the right hand side the ion density. Note that the RHS contains a correction term valid to second order in FLR so as to correctly obtain the particle density from $\tilde{f}_g$. Let us point out that the system of equations (8)-(9) is equivalent to this order to the starting equations (2) -(5) of the spectral approach.

## 3.2 Solving using PIC Algorithm and FEM

Phase space $(\vec{R}, v_{\|}, v_{\perp})$ is discretized into $N_p$ cells of volume $\xi_\nu$ (incompressible under phase space flow) centered at $(\vec{R}_\nu, v_{\|\nu}, v_{\perp\nu})$. If the centers of these cells are pushed in time along the GC trajectories, the discretized distribution function can be approximated by

$$\tilde{f}_g\left(\vec{R}, v_\perp, v_{\|}; t\right) = \sum_\nu \frac{f_\nu(t)}{2\pi v_\perp} \delta\left(\vec{R} - \vec{R}_\nu\left(t\right)\right) \delta\left(v_{\|} - v_{\|\nu}(t)\right) \delta\left(v_\perp - v_{\perp\nu}(t)\right),$$

with the weights $f_\nu$ being evolved as

$$\frac{d}{dt} f_\nu = T_{RHS}|_{(\vec{R}_\nu, v_{\|\nu}, v_{\perp\nu}; t)} \xi_\nu.$$

No approximations were made when integrating the GC trajectories, so that both trapped and circulating particles are fully taken into account.

The quasineutrality equation is solved for $\phi$ at each time step. This second order differential equation is inverted using a finite element method (FEM) so that charge assignment is defined naturally. The finite elements (quadratic splines) are built on a realistic magnetic coordinate mesh provided by the MHD equilibrium code CHEASE [18]. Had one kept full FLR effects, the equation for $\phi$ would have been a numerically time consuming integral equation.

The code is run on a massively parallel CRAY-T3D (32-64 processors). Typical runs take $10^6$ particles and approximately 1 hour computing time.

# 4 Results of Comparisons

## 4.1 Benchmarking

To allow for exact benchmarking, one defines a case that is well within the common approximation limits of both approaches. A large aspect ratio torus must be considered to avoid trapped particle effects which are neglected by the spectral code. Furthermore, the device must be large and the fixed toroidal wave number low so that the second order expansion in $k_\perp \lambda_L$ of the PIC method is valid. The first results presented here are for a system with major radius $R = 30.\text{m}$, minor radius $a = 2.\text{m}$, average ion Larmor radius $\lambda_L = 3.2\text{mm}$, parabolic safety factor profile so that $q_s = 3.25$ on axis and $q_s = 6.25$ on edge, flat density profiles, and temperature profiles having steepest gradients at $s = 0.5$ where $\frac{L_T}{R} = 0.05$. Here $s = \rho/a$ stands for the normalized radial variable and $L_T$ for the characteristic length of equilibrium.

Fig.1 shows the most unstable part of the spectrum as well as the first evaluation of frequency and growth rate of the PIC run. The average position taken by this last point with respect to the first most unstable eigenvalues led to a spectral time analysis of the PIC evolution for each magnetic surface (Fig.2a), which shows that the signal contains

more than one frequency, i.e. is still the superposition of many eigenmodes. Naturally, by pursuing the run even further in time, the highest growing mode would be isolated. Note however that the dominant component in Fig.2a agrees very well with the frequency, radial average position and width of the highest growing eigenmode (Fig.2b). Extracting this frequency from the PIC signal gives the field structure in Fig.3a, very similar to the eigenmode structure in Fig.3b. The next highest growing eigenmodes explain the residual components in Fig.2a.

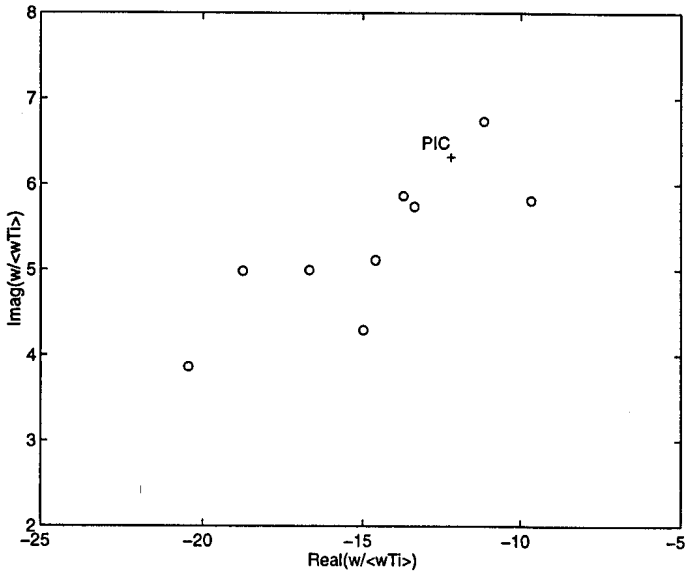


**Fig.1.** Spectrum of highest growing modes; $< \omega_{Ti} >= 250 s^{-1}$.

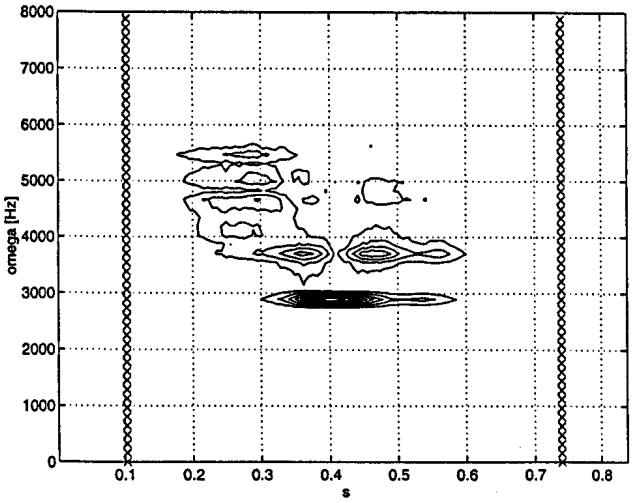


**Fig.2a.** Spectral time analysis of PIC signal as a function of magnetic surface.

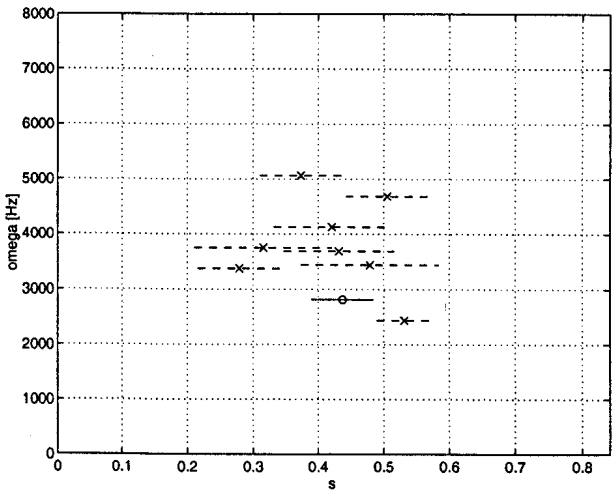


**Fig.2b.** Frequency, position and width of most unstable modes given by spectral results: '—o—':highest, '- -x- -':next.

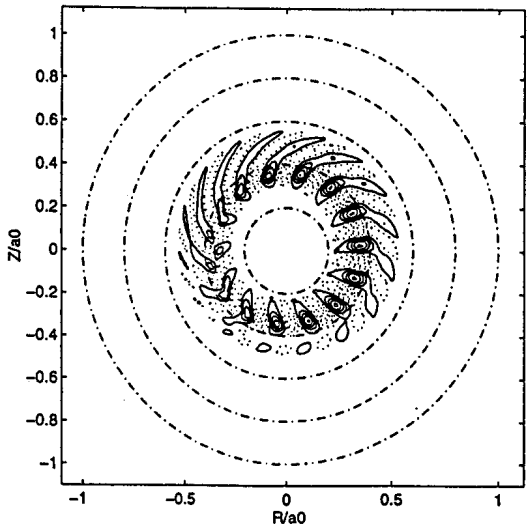


**Fig.3a.** Poloidal field structure of time filtered PIC signal.

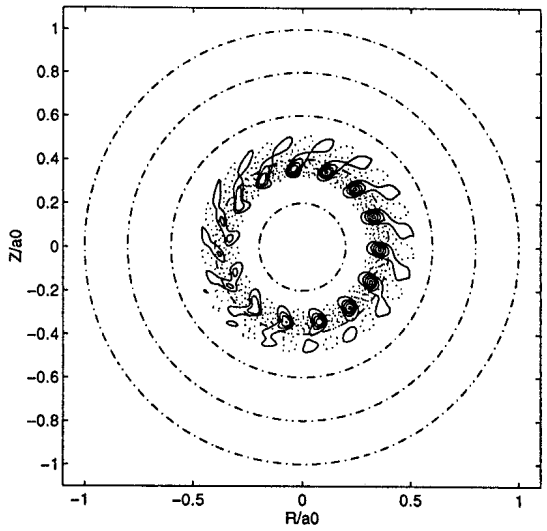


**Fig.3b.** Poloidal mode structure of highest growing mode of spectrum.

## 4.2 Aspect Ratio Scan

The goal here is to study how the eigenmodes transform when going from cylinder to torus. In cylinder magnetic drifts are negligible and temperature gradients eventually give rise to the so-called slab-ITG instability driven by the particle dynamics parallel to the magnetic field line. With increasing toroidicity these modes progressively adopt the full character of the more unstable toroidal-ITG. This second type of instability is flute-like as $k_{\|} \simeq 0$ and therefore is driven by the perpendicular dynamics, i.e. by the magnetic drifts of the particles. These drifts are stabilizing where opposed to the diamagnetic drifts (called favorable curvature regions, usually limited to the inner side of the torus) and destabilizing where going in the same direction (unfavorable curvature regions, usually the outer side of torus). At even higher toroidicity, the driving mechanism is less efficient and the growth rate decreases [11]. The basic understanding of the slab- and toroidal-ITG mode is given by a local fluid dispersion relation [5]-[6], showing that these two modes are different limits of the same branch. In this sense it is strictly wrong to state that toroidicity induces a new mode.

Our reference case is a plasma with major radius $R = 1.2$m, minor radius $a = 0.2$m, average ion Larmor radius $\lambda_L = 3.2$mm, safety factor going from $q_s(s = 0) = 1.25$ to $q_s(s = 1) = 4.25$, flat density, steepest temperature gradients at $s = 0.5$ where $\frac{L_T}{R} = 0.13$, and perturbations with toroidal wave number $n = 4$. This configuration, which we will call full torus, is then unbent into a cylinder keeping $Rq_s$, $nq_s$ and $a$ constant as well as all the equilibrium profiles. In particular, two intermediate states are labeled half and quarter torus, having respectively half and quarter inverse aspect ratio of full torus.

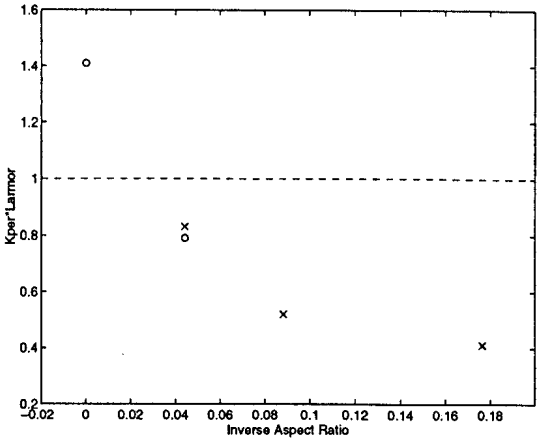


**Fig.5a.** Average value of $k_\perp \lambda_L$ going from cylinder to torus. 'o': eigenmode # 1, 'x': eigenmode # 2.

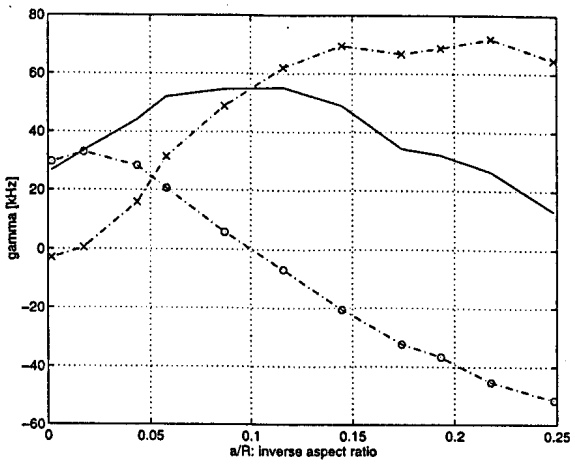


**Fig.5b.** Power transfer from parallel ('o'), and perpendicular ('x') dynamics. The sum is proportional to the growth rate ('-').

## 4.3 Toroidal Wave Number Scan

A toroidal wave number scan was performed for the full torus equilibrium defined in the previous section. PIC and spectral results for frequency and growth rate are shown in Fig.6a and b respectively. There is good agreement near $n = 7$ where the growth rate saturates due to FLR effects.

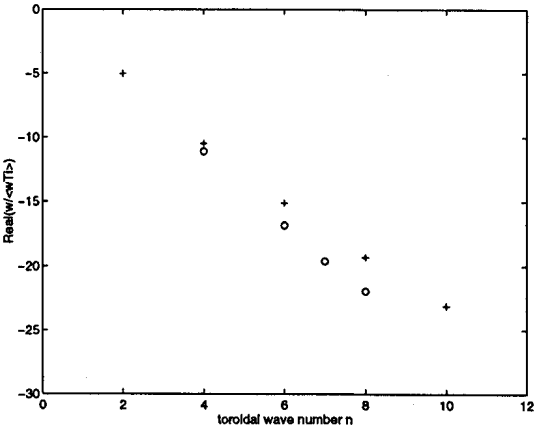


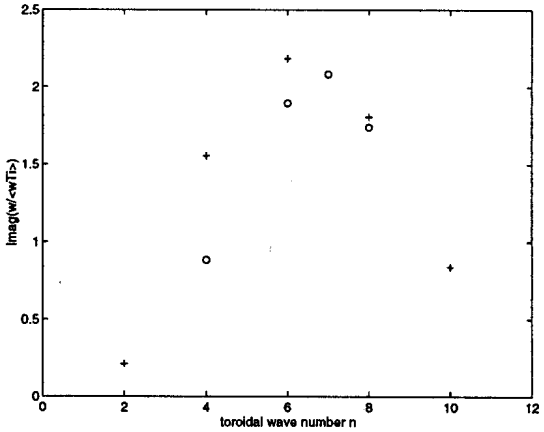


**Fig.6a, b.** Real frequency and growth rate of highest growing eigenmode for varying toroidal wave number. '+': PIC results, 'o': Spectral.

Frequency and growth rate of the highest growing eigenmode are plotted in Fig.4a and b respectively. In cylinder this eigenmode (# 1) turns out to have poloidal mode number $m = 7$. Near quarter torus, a second eigenmode (# 2) takes over. PIC results in cylinder as well as in quarter, half and full torus are also indicated. The two methods agree perfectly on the real part of the frequency. For the growth rate they show the same qualitative behavior for varying aspect ratio but quantitative differences up to 20%.

In Fig.5a the average value of $k_\perp \lambda_L$ evaluated from the spectral results is plotted as a function of the inverse aspect ratio. In cylinder where $k_\perp \lambda_L \simeq 1.4$ one is beyond the limits of the second order FLR expansion performed by the PIC method. In full torus where $k_\perp \lambda_L \simeq 0.4$ one is well within. Therefore, differences between PIC and spectral results at lower aspect ratios are probably explained by trapped particle effects.

A diagnostic on the PIC signal evaluating the power transfer related to parallel and perpendicular dynamics is presented in Fig.5b. Note how the driving mechanism progressively turns from parallel to perpendicular dynamics when going from cylinder to torus, this being the signature of a slab- to toroidal-ITG transition. In full torus parallel dynamics are actually stabilizing and lead to the saturation and decrease of the growth rate.

Plots on the left of Fig.7 give the radial dependence of the poloidal Fourier components with increasing toroidicity, plots on the right-hand side the corresponding structures in configuration space. In cylinder the field is very localized near the rational surface corresponding to the fixed poloidal mode number. In full torus, the ballooning and the appearance of large , slightly twisted coherent structures called 'fingers' follow from the constraints on the mode to be simultaneously localized in the unfavorable curvature region and locally have $k_{||} \simeq 0$.

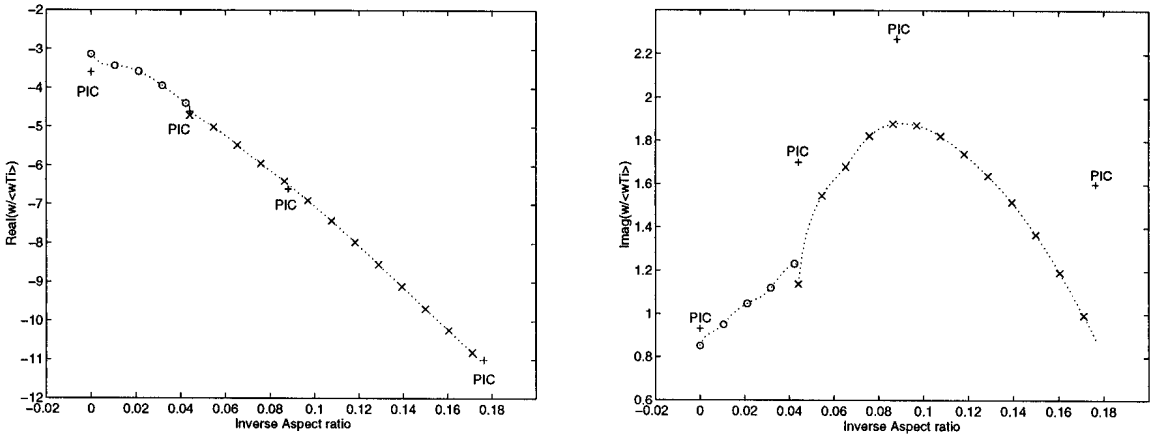


**Fig.4a, b.** Real frequency and growth rate of highest growing eigenmode going from cylinder to torus. 'o': eigenmode # 1, 'x': eigenmode # 2, '+': PIC results; $< \omega_{Ti} >= 22.310^3 s^{-1}$.

**Cylinder.** The highest growing mode has poloidal wave number $m = 7$ and is centered on the corresponding rational surface.

**Quarter Torus.** The poloidal Fourier componants couple by pairs between the corresponding rational surfaces. In configuration space, this leads to a broader but structured radial dependance of the eigenmode.

**Half Torus.** Higher order coupling between the poloidal Fourier components, leads to more coherent structures of the eigenmode called 'fingers'. The mode balloons in the unfavorable curvature region. These are the signatures of a toroidal-ITG mode.

**Full torus.** The toroidal-ITG characters are confirmed.

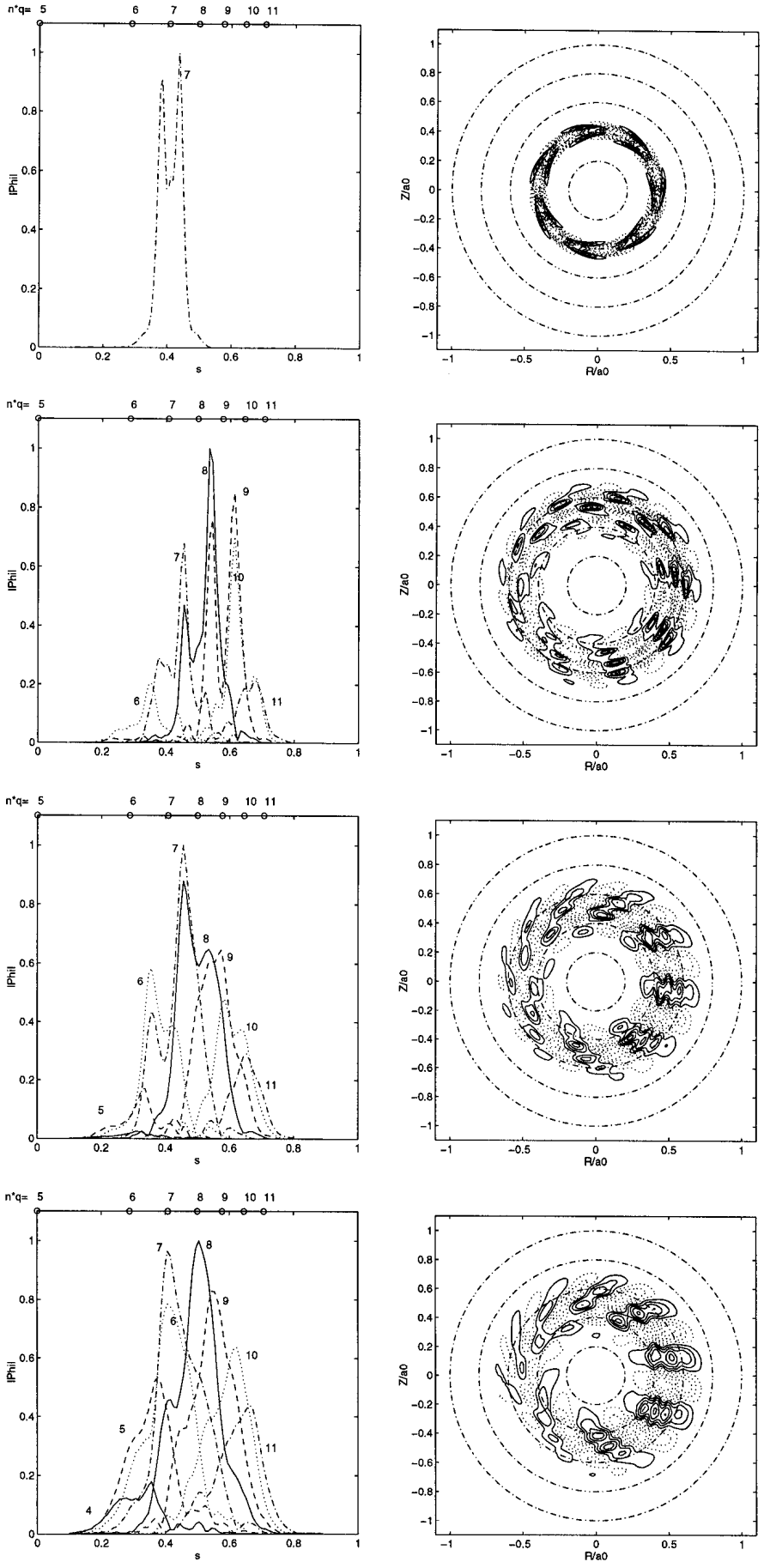


**Fig.7.**

# 5 Conclusions

A time evolution PIC as well as a spectral code for solving global toroidal microinstabilities are being developed. The complementarity of the two approaches has been very useful for benchmarking the codes and in particular for validating and defining the limits of the different approximations made. For cases where trapped particle effects are not significant and for low values of $k_\perp \lambda_L$ comparisons have shown very good quantitative agreement. For other cases where these effects are present but not dominant, at least good qualitative agreement was obtained. Differences show the way for future improvement.

Running these codes in parallel allows to scan efficiently a wide parameter space and give more information on a same problem. The PIC approach considers realistic equilibria, and the effects of shaping (elongation, Shafranov shift, etc) can be studied. Having sampled out the fast poloidal dependence, perturbations with large toroidal mode numbers $n$ ($\sim 100$) can be handled [14]. The eigenvalue approach contains FLR effects to all orders and allows to follow continuously the full unstable spectrum from cylinder to torus.

**Acknowledgment:** This work was supported in part by the Swiss National Science Foundation.

# References

[1] L.I.Rudakov, R.Z.Sagdeev, Nuclear Fusion Suppl.1962 **2**, 481, (1962)

[2] P.Terry, W.Anderson, W.Horton, Nuclear Fusion **22** (4), 487, (1982)

[3] W.Horton, Duk-In Choi, W.M.Tang, Phys.FLuids **24** (6), 1077, (1981)

[4] E.A.Frieman, G.Rewoldt, W.M.Tang, A.H.Glasser, Phys.Fluids **23** (9), 1750, (1980)

[5] F.Romanelli, Phys.Fluids B **1** (5), 1018, (1989)

[6] X.Garbet, L.Laurent, F.Mourgues, J.P.Roubin, A.Samain, X.L.Zou, J.Chinardet, Phys.Fluids B **4** (1), 136, (1992)

[7] J.Q.Dong, W.Horton, J.Y.Kim, Phys.Fluids B **4** (7), 1867, (1992)

[8] G.W.Hamett, M.A.Beer, J.C.Cummings, W.Dorland, W.W.Lee, H.E.Mynick, S.E.Parker, R.A.Santoro, M.Artun, H.P.Furth, T.S.Hahm, G.Rewoldt, W.M.Tang, R.E.Waltz, G.D.Kerbel, J.L.Milovich, 1994 IAEA Proceedings, Vol.3, 463, (1995)

[9] R.D.Sydora, Physica Scripta.52, 474, (1995)

[10] S.E.PArker, W.W.Lee, R.A.Santo, Phys.Rev.Letters 71, 2042, (1993)

[11] M.A.Beer, Princeton Univ. Phd Thesis, (1995)

[12] R.Marchand, W.M.Tang, G.Rewoldt, Phys.Fluids **23** (6), 1164, (1980)

[13] W.M.Tang, G.Rewoldt, Phys.Fluids B **5** (7), 2451, (1993)

[14] M.Fivaz, T.M.Tran, L.Villard, K.Appert, S.Brunner, S.E.Parker, J.Vaclavik, in these proceedings, (1996)

[15] P.J.Catto, Plasma Physics **20**, 719, (1978)

[16] O.Sauter, J.Vaclavik, F.Skiff, Phys.Fluids B **2** (3), 475, (1990)

[17] T.S.Hahm, Phys.Fluids **31** (9), 2670, (1988)

[18] H.Lütjens, A.Bondeson, A.Roy, Comput.Phys.Commun. **69**, 287, (1992)

# Linear gyrokinetic particle-in-cell simulations for small to large toroidal wavenumbers

M. Fivaz, T.M. Tran, L. Villard, K. Appert, S. Brunner, S.E. Parker[1] and J. Vaclavik

Centre de Recherches en Physique des Plasmas, Association Euratom - Confédération Suisse, EPFL, PPB, CH-1015 Lausanne, Switzerland

[1]Department of Physics, University of Colorado, Boulder, CO 80309, USA

## Introduction

We study here low frequency electrostatic microinstabilities driven by ion temperature gradients (ITG instabilities) relevant to anomalous ion heat transport in tokamaks. The plasma is modelled with gyrokinetic ions [1] and adiabatic electrons. An axisymmetric equilibrium magnetic structure is provided by the MHD equilibrium code CHEASE [2]. The full plasma cross-section is considered in the simulations. We follow the time-evolution of electrostatic, quasineutral perturbations of a local Maxwellian equilibrium distribution function, using two different particle-in-cell (PIC) codes running on a massively parallel CRAY-T3D.

## The gyrokinetic model

In the following, $\vec{x}$, $v_{||}$, $v_\perp$ and $\alpha$ denote particle positions, velocity components and gyroangles, $\vec{R}$ and $\vec{\rho}$ guiding center positions and the vectors pointing from them to the particles (Larmor radius), $\vec{B}$ and $\vec{h}$ the magnetic field and its direction, $T_e$ and $n_0$ the electron temperature and density, and $\Omega$ the ion cyclotron frequency, respectively.

In this notation, the trajectories of the guiding center motion in phase space and the evolution of the perturbed guiding center distribution function, $f(\vec{R}, v_{||}, v_\perp, t)$, are given by

$$\frac{d}{dt}\left(\vec{R}, v_{||}, v_\perp\right) = \left(v_{||}\vec{h} + \frac{v_{||}^2 + v_\perp^2/2}{\Omega}\vec{h}\times\frac{\nabla B}{B}\ ,\ \frac{1}{2}v_\perp^2\nabla\cdot\vec{h}\ ,\ -\frac{1}{2}v_\perp v_{||}\nabla\cdot\vec{h}\right) \qquad (1)$$

and

$$\left.\frac{df}{dt}\right|_{guiding\ center\ trajectory} = T_{RHS} \qquad (2)$$

where

$$T_{RHS} = -\frac{\langle\vec{E}\rangle\times\vec{B}}{B^2}\frac{\partial f_0}{\partial\vec{R}} - \frac{\Omega}{B}\langle E_{||}\rangle\frac{\partial f_0}{\partial v_{||}} - \left(v_{||}\frac{\partial f_0}{\partial v_{||}} + \frac{1}{2}v_\perp\frac{\partial f_0}{\partial v_\perp}\right)\langle\vec{E}\rangle\cdot\vec{h}\times\frac{\nabla B}{B^2} \qquad (3)$$

The electric potential, $\phi(\vec{x},t)$, and the gyro-averaged electric field, $\langle\vec{E}\rangle$, are given by

$$\frac{n_0 e}{k_b T_e}\phi(\vec{x},t) - \nabla_\perp\cdot\frac{n_0}{B\Omega}\nabla_\perp\phi(\vec{x},t) = \int f(\vec{R},v_{||},v_\perp,t)\delta(\vec{R}-\vec{x}+\vec{\rho})d\vec{R}d\vec{v} \qquad (4)$$

and

$$\langle\vec{E}\rangle(\vec{R},v_\perp,t) = -\int \nabla\phi(\vec{x},t)\delta(\vec{x}-\vec{R}+\vec{\rho})d\vec{x}d\alpha. \qquad (5)$$

Since the equilibrium is axisymmetric, one can Fourier-expand the perturbed quantities $\phi$ and $f$ in the toroidal angle $\varphi$, and keep one toroidal harmonic $n$ only. This reduces the problem to two spatial dimensions. The resulting equations are solved with a finite element particle-in-cell method.

## Poloidal structure of ITG modes

ITG modes can be unstable only when the parallel wavenumber $k_{||}$ is small. Setting $\vec{B}\cdot\nabla\phi(s,\chi,\varphi) = 0$, we can therefore get a good estimate of the poloidal mode structure:

$$\phi(s,\chi,\varphi) = \phi(s)\exp[-i(n\varphi + nq(s)\chi)], \qquad (6)$$

$$\chi(s,\theta) = \int_0^\theta \frac{B_{tor}}{Rq(s)\vec{B}_{pol}\cdot\nabla\theta}d\theta. \qquad (7)$$

Here, $\theta$, $\chi$, $s$ and $q$ are the poloidal angle, the "straight-field-line" angle, the square root of the normalized poloidal magnetic flux function and the safety factor, respectively. In Figure 1, we show, on an example, how well the structure given by Eq. (6) can mimic that of a "real" unstable mode obtained from a PIC simulation. For this, $\phi(s)$ has been chosen to be a Gaussian centered at $s_0$, the position of the largest temperature gradient in the simulation, and with a width given by that of the real mode. As high-$n$ modes have a fine poloidal structure, their numerical treatment demands a large number of poloidal grid points and, as a consequence, small timesteps $\Delta t$ as well. Indeed, integration accuracy and stability require $\Delta t$ to be smaller than the time it takes a particle to cross one poloidal wavelength. This translates into a maximum timestep which is inversely proportional to $n$ and makes the simulation of high-$n$ modes very difficult.

Eigenmode from simulation  Structure given by Eq. (6)

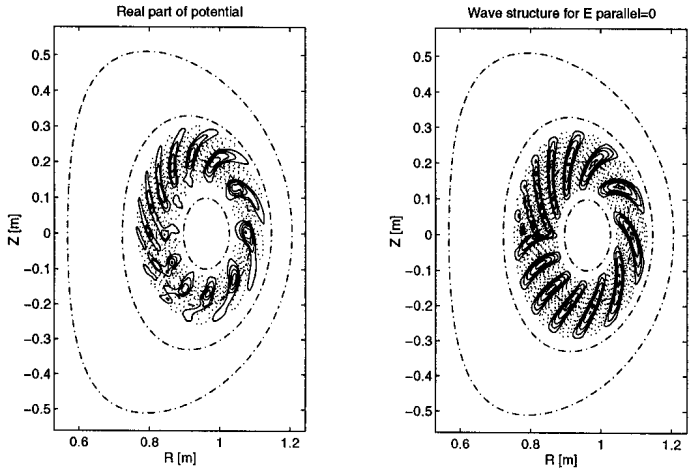


Figure 1

**Extraction of fast $k_{||} = 0$ poloidal variation**

The mentioned difficulty can be overcome by taking advantage of the approximate knowledge given by Eq. (6). In fact, the fast poloidal variation corresponding to $k_{||} = 0$ can be extracted from the gyrokinetic equations. Let us define transformed quantities, $\tilde{f}$ and $\tilde{\phi}$, by writing

$$\phi(s,\theta) = \tilde{\phi}(s,\theta)\, e^{iS(s,\theta)} \tag{8}$$

and

$$f(s,\theta) = \tilde{f}(s,\theta) e^{iS(s,\theta)} \tag{9}$$

where

$$S(s,\theta) = inq(s)\chi(s,\theta). \tag{10}$$

The non-periodicity in $\theta$ of $\tilde{\phi}$ and $\tilde{f}$ leads to technically cumbersome jump conditions. To avoid them, we consider a simpler choice for $S$,

$$S(\theta) = im_0\chi(s_0,\theta) \tag{11}$$

where $m_0$ is an integer close to $nq(s_0)$ and $s_0$, again, the position of maximal temperature gradient.

The transformed quantities, $\tilde{f}$ and $\tilde{\phi}$, vary slowly in the poloidal direction, even for high toroidal mode numbers. The equations for the transformed quantities can be derived without approximation. Defining $\vec{K} = \nabla S$ and noting that $\frac{dS}{dt} = \vec{K}\cdot\frac{d\vec{R}}{dt}$, the Eqs. (2, 4 and 5) become

$$\frac{d\tilde{f}}{dt} + i\frac{dS}{dt}\tilde{f} = \tilde{T}_{RHS}, \tag{12}$$

$$\frac{n_0 e}{k_b T_e}\tilde{\phi}(\vec{x},t) - \left(i\vec{K}_\perp + \nabla_\perp\right)\cdot\frac{n_0}{B\Omega}\left(i\vec{K}_\perp + \nabla_\perp\right)\tilde{\phi}(\vec{x},t) = \tag{13}$$

$$= \int \tilde{f}(\vec{R}, v_{||}, v_\perp, t)\delta(\vec{R} - \vec{x} + \vec{\rho}) e^{iS(\vec{R}) - iS(\vec{x})} d\vec{R} d\vec{v}$$

and

$$\langle\vec{\tilde{E}}\rangle(\vec{R}, v_\perp, t) = -\int \left(i\vec{K} + \nabla\right)\tilde{\phi}(\vec{x},t)\delta(\vec{x} - \vec{R} + \vec{\rho}) e^{iS(\vec{x}) - iS(\vec{R})} d\vec{x} d\alpha. \tag{14}$$

The time integration of the fast phase variation in equation (12) needs special care if large timesteps are to be taken. A good integration scheme for arbitrary values of $\frac{dS}{dt}\Delta t$ is obtained by splitting the timestep and integrating the fast variation analytically:

**(a)** $\tilde{f}_* = \tilde{f}^t + \tilde{T}_{RHS}\frac{\Delta t}{2}$,

**(b)** $\tilde{f}_{**} = \tilde{f}_*\, e^{i\frac{dS}{dt}\Delta t}$,

**(c)** $\tilde{f}^{t+\Delta t} = \tilde{f}_{**} + \tilde{T}_{RHS}\frac{\Delta t}{2}$.

The described extraction method has been implemented in our linear gyrokinetic PIC code and works as expected, Figure 2. The number of poloidal grid points needed is reduced, which in turn reduces the numerical noise and the number of particles required. The simulation timestep can be greatly increased because the poloidal wavelength of the transformed quantities is large (Figure 2b) and independent of $n$. As a consequence, the extraction decreases the cost of large $n$ simulations by two orders of magnitude without diminishing the precision of the results.

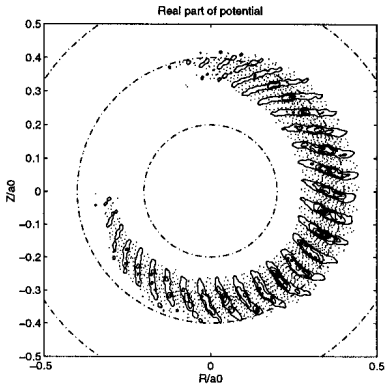


Fig 2a. Potential $\phi$ in simulation without extraction. $\omega$=627 kHz, $\gamma$=233 kHz, 128 poloidal grid points.

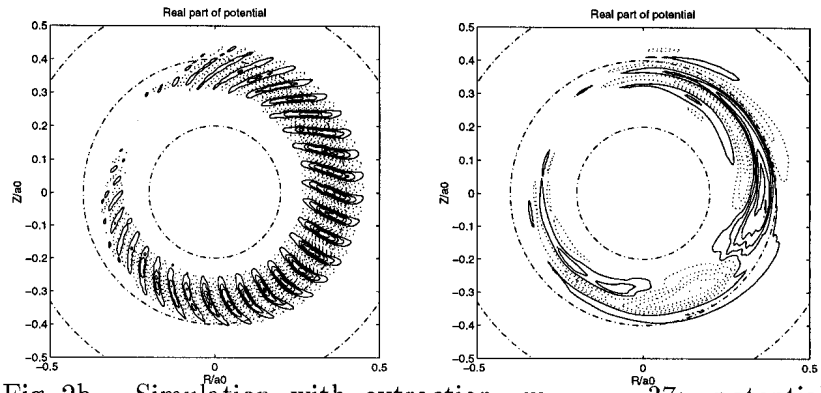


Fig 2b. Simulation with extraction, $m_0 = -37$: potential $\phi = \tilde{\phi}e^{iS}$ (left) and transformed potential $\tilde{\phi}$ (right). $\omega$=634 kHz, $\gamma$=243 kHz, 32 poloidal grid points. The timestep is 24 times larger and both, the noise and the number of poloidal grid points, are reduced.

**Results for $n$-scan in a TFTR-like equilibrium**

The transition from low to high toroidal mode numbers was studied in a TFTR-like circular equilibrium with the global parameters $R = 2.58m$, $a = .92m$, $R/a = 2.8$, $a/\rho_i = 660$, $B = 3.8T$ and $T_i = T_e = 1.3keV$. Locally, at $r/a = 1/3$, we have $L_n/R = .28$, $q = 1.4$, shear $\hat{s} = .53$ and $\eta_i = 4$, where the undefined symbols have the usual meaning.

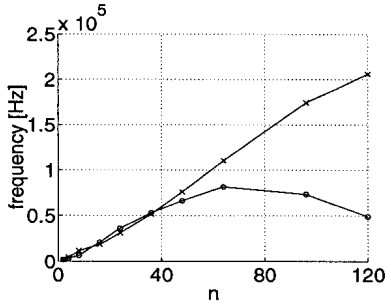


Fig 3a: frequency (x) and growth rate (o)

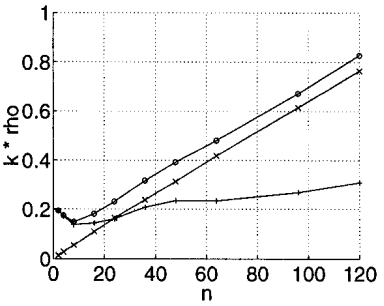


Fig 3b: perp. (o), poloidal (x) and radial (+) wavenumbers

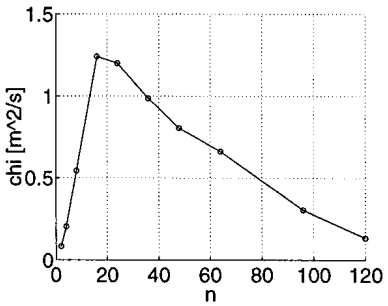


Fig 3c: mixing-length estimate of ion heat transport

Figure 3 shows the frequency $\omega$ and growth rate $\gamma$, the perpendicular wavenumbers and the mixing length estimate of the ion heat diffusion coefficient as functions of $n$. Figure 4 shows a few eigenmodes.

The typical bounce frequency is $\omega_b$=40 kHz. At low $n$, $\omega < \omega_b$ and the modes have a strong trapped-ion character: the trapped-ion precession is strongly destabilizing. At

very low $n$ ($n = 4$), the mode covers one rational surface only, and the perpendicular wavenumber $k_\perp$ is given by its radial componant $k_r$.

At very high $n$, the mode covers many rational surfaces and the usual ballooning structure is recovered. Here, $\omega > \omega_b$ and the trapped-ion precession has no effect; the mode can be classified as "toroidal ITG". The perpendicular wavenumber is given by its poloidal componant $k_\theta$.

Both, the radial extension of the modes (not shown) and the mixing length estimate of the ion heat transport (Fig. 3c), peak around $n = 16$. It could therefore be that these intermediate values of $n$ would produce the largest transport. Modes in this range have a mixed toroidal-ITG and trapped-ion mode character.

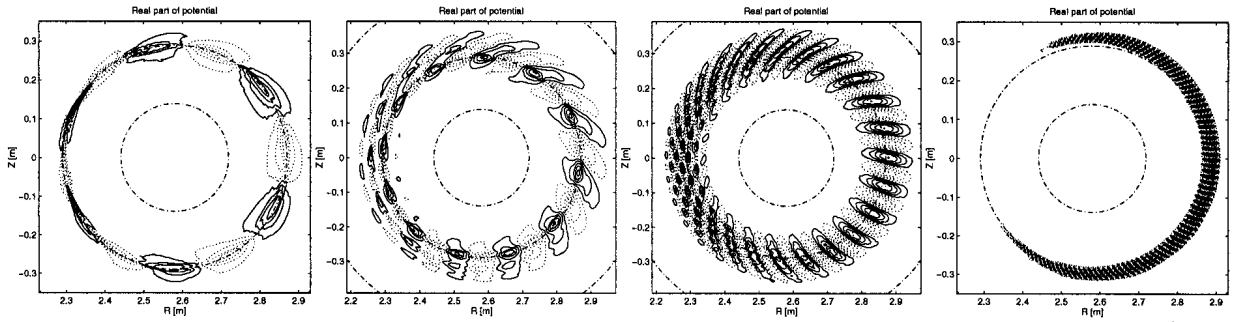


Fig 4: $n$=4 $n$=8 $n$=16 $n$=96

## The effect of a magnetic well

A variety of JET-shaped MHD equilibria were produced using the equilibrium code CHEASE[2], keeping the shape of the boundary and the safety factor at $s_0 = 0.5$ fixed. Their stability was studied using our PIC code [3], as well as a version of ORB [4], modified to take the magnetic structure of the MHD equilibrium into account. Both codes give essentially the same results. The main parameters are: $R = .96$ m, $a = .35m$, $R/a = 2.8$, elongation=1.6, triangularity=.3, $a/\rho_i = 76$, $B = 1T$, $T_i = T_e = 1.keV$. At $s = s_0 = 0.5$: $L_T/R = .125, q = 2, \eta_i = \infty$.

In the fluid limit, the drift frequency is defined by $\omega_d = nq\vec{v}_d \cdot \nabla\chi$, where the magnetic drift velocity, $\vec{v}_d = \frac{v_{Thi}^2}{\Omega B^2}\vec{B}\times\nabla B$. The local dispersion relation for ITG modes predicts (local) stability for $\omega_d < 0$ (good curvature) and instability for $\omega_d > 0$ (bad curvature) [5] [6]. Figure 5 shows the contours of $\omega_d$ (a) in the standard case of a configuration without a magnetic well, and (b) in a configuration with a strong magnetic well. In the latter, the drift velocity is reversed over a substantial region on the low field side of the torus; this has been predicted to stabilize microinstabilities [7].

The equilibrium shown in Fig. 5a is unstable for several toroidal mode numbers; the corresponding growth rates are shown on Fig. 6. On the other hand, the equilibrium shown in Fig 5b was indeed found to be fully stable to ITG modes, i.e., stable for all values of n. This is because the region of bad curvature is too small that a mode could simultaneously satisfy $k_{||} \approx 0$ and gather an overall positive contribution from

$\omega_d$, despite the infinite value of $\eta_i$ and the value of $L_T/R = .125$ which usually lead to high growth rates [8].

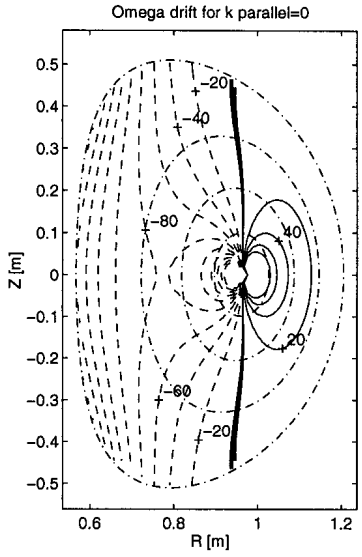


Fig 5a: $\omega_d$ for $k_{||} = 0$

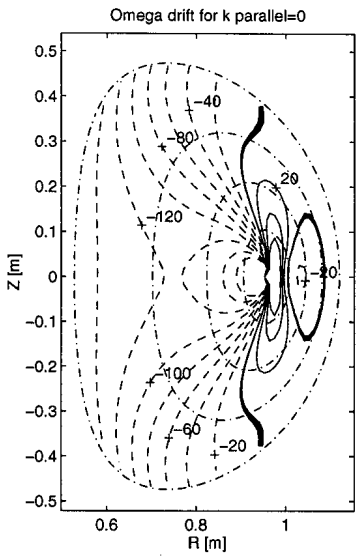


Fig 5b: $\omega_d$ for $k_{||} = 0$

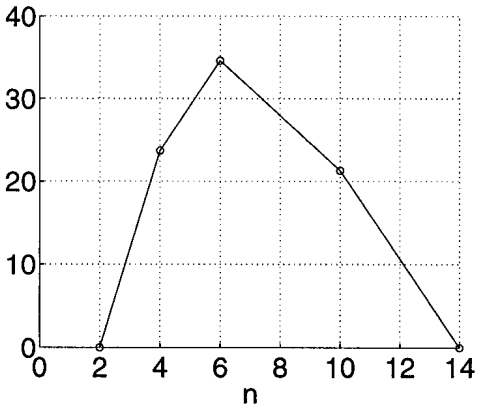

Fig 6: Growth rate vs $n$

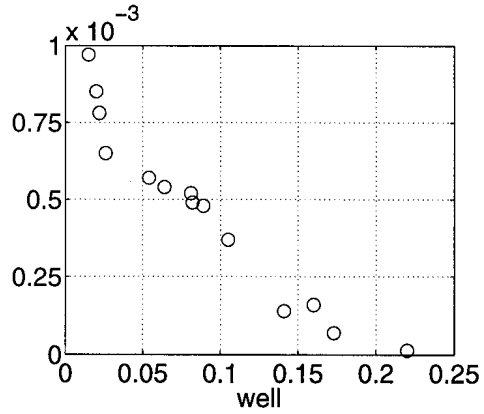


Fig 7: Growth rate vs $W$

The magnetic well $W$ [9] is a global (on a magnetic surface) measure of the inhomogeneity of the magnetic field. The growth rate as function of $W(s = s_0 = 0.5)$ is shown in Fig.7 for all the configurations studied. It appears that the depth of the magnetic well is a good predictor of ITG stability as claimed by Rosenbluth and Sloan [7] for many microinstabilities.

## Conclusions

The fast poloidal phase variation corresponding to $k_{||} = 0$ has been extracted, without approximation, from the distribution function and the potential. This procedure has sped up the linear PIC code by two orders of magnitude when high-$n$ modes are simulated because larger timesteps, lower poloidal resolution and fewer particles can be used.

The transition from low to high toroidal mode numbers has been studied in a TFTR-like equilibrium. At low $n$, the mode has a trapped-ion character and is localized around one rational surface. At high $n$, it has a toroidal ITG character and extends over many rational surfaces. At intermediate values of $n$ where it produces the largest mixing-length estimate of transport, it covers a few rational surfaces only and is of mixed character.

By studying a variety of magnetic structures at fixed boundary shape and a fixed value of the safety factor at half radius, we found that the MHD equilibrium structure affects the stability of ITG modes primarily through the magnetic well. A strong magnetic well, by reducing or even reversing the magnetic drifts, can fully stabilize the ITG modes. Other parameters such as the local shear, the Shafranov shift or the plasma $\beta$ were found to have less or no correlation with the growth rate.

The presence of a substantial magnetic well is only possible in high $\beta_p$ discharges. Recently, high $\beta_p$ experiments have been reported from several tokamaks which showed very good transport properties. In the view of our results, it is tempting to explain these properties by the presence, in these discharges, of diamagnetic wells sufficiently deep to stabilize the ITG modes and hence improve confinement.

**Acknowledgments**

We are grateful to A. Cooper, O. Sauter, D. Ward and S. Wüthrich for useful discussions.

This research was supported in part by both the Cray/EPFL Parallel Application Technology Program and the Swiss National Science Foundation.

# References

[1] T. S. Hahm, Phys. Fluids **31**, 2670 (1988).

[2] H. Luetjens, A. Bondeson, and O. Sauter, Comput. Phys. Commun. **97**, 219 (1996).

[3] S. Brunner *et al.*, *in these Proceedings.*

[4] S. Parker, W. Lee, and R. Santoro, Phys. Rev. Letters **71**, 2042 (1993).

[5] X. Garbet *et al.*, Phys. Fluids **4**, 136 (1992).

[6] F. Romanelli, Phys. Fluids B **1**, 1018 (1989).

[7] M. Rosenbluth and M. L. Sloan, Phys. Fluids **14**, 1725 (1971).

[8] J. Dong, W. Horton, and J. Kim, Phys. Fluids B **4**, 1867 (1992).

[9] J. P. Freidberg, in *Ideal Magnetohydrodynamics* (Plenum, 233 Spring St., New York, NY 10013, 1987), Chap. 6, p. 107.

# Global stability of plasmas with helical boundary deformation and net toroidal current against $n = 1, 2$ external modes

**A. Ardelea** and W. A. Cooper
CRPP/EPFL, Association Euratom/Confederation Suisse,
Lausanne, Switzerland

## 1 Introduction

In this paper we resume a numerical study of the global stability of plasmas with helical boundary deformation and non null net toroidal current. The aim was to see whether external modes with $n = 1, 2$ ($n$ toroidal mode number) can be stabilized at values of $\beta$ inaccessible to the tokamak. L=2,3 configurations with several aspect ratios and different numbers of equilibrium field periods are considered. A large variety of toroidal current densities and different pressure profiles are taken into account. Mercier stability is also investigated.

## 2 Equilibrium and stability codes

The 3D equilibria with nested magnetic surfaces and single magnetic axis are generated with the VMEC code [1] [2]. Input parameters are : $N_{per}$ the number of equilibrium field periods, $\epsilon$ the inverse aspect ratio, $J'(s)$ the toroidal current density profile, $p(s)$ the pressure profile and $\Phi(s)$ the toroidal flux function. Here $s$ represents the radial coordinate which is chosen proportional to $\Phi$, i.e. $d\Phi/ds = cst$. The plasma boundary is kept fixed and its shape is specified by choosing the Fourier amplitudes $R_{m_b n_b}$ and $Z_{m_b n_b}$

$$R(s=1,u,v) = \sum_{m_b,n_b} R_{m_b n_b}(s) cos(m_b u - n_b N_{per} v)$$

$$Z(s=1,u,v) = \sum_{m_b,n_b} Z_{m_b n_b}(s) sin(m_b u - n_b N_{per} v)$$

where the subscript $_b$ stands for boundary and $u$ and $v$ are the poloidal and toroidal coordinates. The Fourier amplitudes of the inverse coordinates R (the distance from major axis) and Z (the distance from midplane) obtained from VMEC together with $\Phi'(s)$ and $\Psi'(s)$, which are the radial derivatives of the toroidal and poloidal magnetic flux functions, form the input to the stability code TERPSICHORE [4]. The variational formulation of the linear MHD stability of 3D plasmas on which TERPSICHORE is based is described in detail in [3]. The variational equation is written as:

$$\delta W_p + \delta W_v - \omega^2 \delta W_k = 0$$

with

$$\delta W_p = \frac{1}{2}\int\int\int d^3x \left\{Q^2 + \Gamma p(\vec{\nabla}\cdot\vec{\xi})^2 + \vec{j}\wedge\vec{\xi}\cdot\vec{Q} + (\vec{\xi}\cdot\vec{\nabla}p)(\vec{\nabla}\cdot\vec{\xi})\right\}$$

$$\delta W_v = \frac{1}{2}\int\int\int d^3x \left|\vec{\nabla}\wedge\vec{A}\right|^2 \qquad \delta W_k = \frac{1}{2}\int\int\int d^3x \vec{\xi}\cdot\rho_M\cdot\vec{\xi}$$

where $\delta W_p$, $\delta W_v$, $\delta W_k$ and $\omega^2$ represent the potential energy in the plasma, the magnetic energy in the vacuum region, the kinetic energy and the eigenvalue of the system. The perturbations have been assumed to evolve as $exp(i\omega t)$ and the system is unstable to MHD modes when $\omega^2 < 0$. $\vec{\xi}$ is the displacement vector, $\vec{Q}$ stands for the perturbed magnetic field and $\vec{A}$ represents the perturbed vector potential. TERPSICHORE reconstructs the MHD equilibrium and maps it to the Boozer coordinate system $(s,\theta,\phi)$. The displacement vector expressed as [3]:

$$\vec{\xi} = \sqrt{g}\xi^s\vec{\nabla}\theta\wedge\vec{\nabla}\phi + \eta\frac{\vec{B}\wedge\vec{\nabla}S}{B^2} + \left[\frac{J(s)}{\Phi'(s)B^2}\eta - \mu\right]\vec{B}$$

with $(\xi^s,\eta,\mu)$ the (radial,binormal,parallel) components. By imposing the incompressibility constraint $\vec{\nabla}\cdot\vec{\xi} = 0$ to get rid of the positive definite term $\Gamma p(\vec{\nabla}\cdot\vec{\xi})^2$ from $\delta W_p$, the parallel component $\mu$ is eliminated as a variable from the problem and the two remaining components of the perturbation are expanded in truncated Fourier series,

$$\xi^s(s,\theta,\phi) = \sum_l \xi_l(s)sin(m_l\theta - n_l\phi) \qquad \eta(s,\theta,\phi) = \sum_l \eta_l(s)cos(m_l\theta - n_l\phi)$$

where $m_l$ and $n_l$ are the poloidal and toroidal mode numbers, $l$ being the index of an $(m,n)$ pair.

# 3 Studied configurations

Configurations of the type $L = 2$ and 3 have been studied i.e. the plasma boundary has been prescribed according to the following equations

$$L=2 \quad \begin{cases} R(s=1,u,v) &= R_0 + cosu + \delta\left(cos(u) + cos(u - 2N_{per}v)\right) \\ Z(s=1,u,v) &= sinu - \delta\left(sin(u) + sin(u - 2N_{per}v)\right) \end{cases}$$

$$L=3 \quad \begin{cases} R(s=1,u,v) &= R_0 + cosu + \delta\left(cos(2u - N_{per}v) + cos(2u - 3N_{per}v)\right) \\ Z(s=1,u,v) &= sinu - \delta\left(sin(2u - N_{per}v) + sin(2u - 3N_{per}v)\right) \end{cases}$$

$\delta$ being a measure of the boundary deformation.

In a geometry with $N_{per}$ field periods the configuration repeats itself $N_{per}$ times when going in the toroidal direction. It follows that modes with toroidal number $n$ are only coupled to modes with $n$, $n \pm N_{per}$, $n \pm 2N_{per}$, etc. There are a total of $N_{fam} = N_{per}/2$ families ( $N_{fam} = (N_{per} - 1)/2$ families) of modes for configurations with an even (odd)

number of field periods [5], [6]. If $k$ labels one of these families the modes belonging to it will have a toroidal mode number given by

$$n = n_i(k, N_{per}) = iN_{per} \pm k \quad i = .., -1, 0, 1, .. \quad k \in \{1, N_{fam}\}.$$

The following remarks can be made: 1) $N_{fam}$ increases with the number of field periods. If $N_{per} \leq 3$ there is a single family (with all $n$ 's), if $N_{per} = 4, 5$ there are two families and so on. 2) The coupling between modes with close values of $n$ is restricted to configurations with small $N_{per}$. 3) If $N_{per}$ is even the familiy $k = N_{fam} = N_{per}/2$ contains less modes than the other families. For practical reasons which result from the observations above, we have limited the computation to configurations with $N_{per} = 4, 5$ and 7 ($N_{per} = 2, 3, 6$ and greater values were left aside).
Several values have been taken for the aspect ratio $1/\epsilon = 5, 8, 10, 13, 17$. The toroidal current density was prescribed with

$$J'(s) = a_1 (1 - s^{a_2})^{a_3} + a_4 (1 - s^{a_5})^{a_6}$$

the six parameters $a_{1,..,6}$ offering a large choice of profiles; $a_4$, $a_5$ and $a_6$ were taken nonzero only for hollow $J'(s)$ profiles. All the computations were made with pressure profiles given by $p(s) = p_0[(1-s)^2 + (1-s^2)^2]$ (p#1) and $p(s) = p_0(1-s^2)$ (p#2) at $\beta = 0.3$, 1 and 2%

The following procedure was used ; for a given configuration with fixed $L, N_{per}, \epsilon$, a sequence of equilibra $\mathcal{E}_i$ ( $i = 0, 1, ..$ ) was generated so that :
- all $\mathcal{E}_i$ resulted from the same current density $J'(s)$ profile .
- each $\mathcal{E}_i$ was computed with an increasing boundary deformation parameter $\delta_i = \delta_{start} + i\,\Delta\delta$. In general $\delta_{start} = 0$ such that $\mathcal{E}_0$ corresponds to the circular tokamak equilibrium.
- the shape of the pressure profile was the same (p#1 or p#2 ) but $p_0$ was adjusted to keep $\beta$ constant.
This basic procedure was repeated for other $J'(s)$ and $p(s)$ profiles and all studied combinations of $L$, $N_{per}$, $\epsilon$. For each equilibrium thus obtained TERPSICHORE was called to calculate the global stability and the Mercier criterion.

# 4 Results

As mentioned above that we tried to start sequences of equilibria with the circular tokamak. The reason was that we wanted to see the effect of a helical boundary deformation on the $n = 1, 2$ modes, in the cases in which these modes are unstable in the circular tokamak. However, combinations of input parameters were considered (in general low, peaked currents, high $1/\epsilon$), for which the circular equilibrium did not exist (VMEC did not converge, Shafranov shift inacceptably large at $\delta = 0$,..). In those cases the sequence was started with a $\delta_{start} \neq 0$ which ensured a proper equilibrium.

The numerical study has shown that it is possible to stabilize the $n = 1, 2$ global modes. In fact we are meaning the $(m, n) = (2, 1)$ and $(3, 2)$ modes but the $(3, 1)$, $(4, 1)$ ,$(4, 2)$, etc were also included in the calculations. The results can be summarized as follows (the given numerical values are related to the $(2, 1)$ mode) :

- when $\delta$ is increased $q$ is lowered; $q_{edge}$ is lowered much more rapidly than $q_{axis}$ (for $L = 3$ $q_{axis}$ is barely changed). Increasing $\delta$ causes $\omega^2$ to rise and plasma becomes less unstable. If $q_{edge} \leq q_{res} = m/n$ the mode $(m, n)$ is strongly destabilized. As $\delta$ is further increased $\omega^2$ attains a minimum after which it starts increasing again. A stability window $[\delta_{min}, \delta_{max}]$ may then appear (see *Fig.1,2*). Stabilization is lost when the minimum of the security factor $q_{min}$ is less than one somewhere in the plasma. This happens at $\delta \simeq \delta_{max}$.
- if the equilibrium is such that $q_{min}$ is already low at $\delta = 0$ then increasing $\delta$ may not stabilize the plasma.
- increasing/decreasing $J'(s)$ but keeping it's profile the same ( by changing only $a_1$), new stability windows are obtained. The representation of these stability windows in a $(q_{axis}, q_{edge})$ plane gives a stability area (see *Fig.3,4*). It's left (small $q_{axis}$) and lower (small $q_{edge}$) margins are limited by the condition $q_{min} > 1.0$, and the upper margin corresponds to $\delta \simeq \delta_{min}$. The right limit (large $q_{axis}$) is not well defined; this topic will be discussed below.
- in general the stability area is situated under the diagonal $q_{edge} = q_{axis}$ and in the region limited by $q_{edge} \leq 1.5$ but for strong and peaked currents, stable plasmas are obtained with $q_{axis} < q_{edge}$. Small currents require more deformation for stabilization (bigger $\delta_{min}$) than large currents. Peaked current profiles ($a_2 < 1.5$) yield compact areas, situated mostly in the $1.0 < q_{axis} < 1.5$ region and broader currents ($a_2 > 5$) give areas elongated in the $q_{axis}$ direction. Hollow currents ($sign(a_1) \neq sign(a_4)$) produce stable areas shifted towards large $q_{axis}$.
- $N_{per} = 7$ produces the least extended stable zones. Although beeing different in details, $N_{per} = 4$ and $N_{per} = 5$ give comparable stability zones ($N_{per} = 4$ is slightly better).
- configurations with $L = 2$ give better results than those with $L = 3$ but require much larger values of the deformation parmeter: $\delta_{min}^{L=2} \geq 0.2$ compared with $\delta_{min}^{L=3} \simeq 0.1 - 0.15$.
- with respect to the aspect ratio, the best results were obtained for $1/\epsilon = 8$ and 10. The largest $1/\epsilon = 17$ and the smallest $1/\epsilon = 5$ gave reduced stability zones.
- a different pressure profile (p#2 instead of p#1) does not bring major changes to the size or position of the stability area. At $\beta = 1\%$ stable areas were obtained for a large variety of combinations of $L$, $N_{per}$, $\epsilon$ and current profiles. At $\beta = 2\%$ calculations were done only for $1/\epsilon = 10$ and we found that it is still possible to find stable areas but they are strongly diminished and exist only for a reduced set of combinations of equilibrium parameters.
- Mercier stability at $\delta = 0$ depends on the equilibrium parameters. Configurations have been found for which the Mercier criterion can be satisfied for $\delta$ between zero and a max-

imun value $\delta_M$. For $\delta > \delta_M$ more and more surfaces become Mercier unstable. The aim was to have $\delta_M > \delta_{min}$ which, in general, was not the case. The highest values for $\delta_M$ were obtained with low, peaked currents and p#1 profiles.
The Mercier criterion was satisfied only for configurations with $L = 3$, $N_{per} = 4, 5$ $1/\epsilon \geq 8$ and small currents. Unfortunately this corresponded to the points at the right limit of the stable zone in the $(q_{axis}, q_{edge})$ plane i.e. at large $\Delta_{sh}$ (more than 15%).

In the cases when stable areas are still open at their right side for values of $q_{axis} \geq 2$, the continuation of calculations for higher $q_{axis}$ (lower currents) may become difficult. The following remarks can be made with respect to this problem :
- the p#1 profile produces equilibria with large Shafranov shifts $\Delta_{sh} \simeq 10 - 18\%$ and for low, peaked currents at high apect ratio the circular tokamak equilibrium does not even exist. However, increasing the helical deformation diminishes the Shafranov shift; for $L = 2$ configurations $\Delta_{sh}$ is diminished by a factor of 2 and more when going from $\delta = 0$ to $\delta \geq \delta_{min}$.
- working with currents which are lower and lower causes VMEC to produce equilibria with inacceptable $\Delta_{sh}$ i.e. $\geq 15 - 20\%$. When these values are encountered stability investigation for smaller currents is stopped. For peaked currents at high $1/\epsilon$ such problems may appear for $q_{axis} \geq 1.6 - 1.8$, whereas for hollow currents it is possible to continue beyond $q_{axis} \geq 2.2 - 2.5$.
- the p#2 parabolic pressure profile was introduced with the aim of reducing the Shafranov shift. It effectively brought down these large $\Delta_{sh}$ to more acceptable values of $6 - 9\%$ and pushed the above mentioned limits of $q_{axis}$. However, we still could not continue with lower currents, because the null pressure gradient at the flux surfaces near the axis caused increasing problems in computing the equilibrium.
- convergence studies have shown that the points of the $(q_{axis}, q_{edge})$ plane which are situated in the stable area with $q_{axis} \geq 2$ tend to be marginaly stable, independently of the pressure or current profile.

Stable areas associated to the $(m, n) = (3, 2)$ mode suffer from an important reduction in size comming from the fact that this mode is destabilized for values of $q_{edge}$ around and inferior to 1.5. This shrinks the stable area under $q_{edge} \simeq 1.3$ and does not look promissing if we try to imagine what will be the stble area produced by modes with higher $n$'s ( $(4, 3)$ for example).

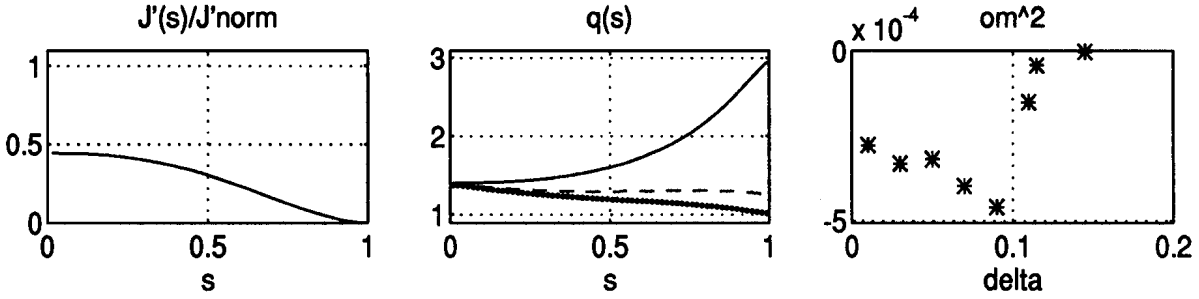


**Fig.1** Study of the (2,1) mode : $J'(s)$ profile, $q$ profile and the most unstable eigenvalue $\omega^2$ as a function of $\delta$ for a configuration characterized by $L = 3, N_{per} = 5, 1/\epsilon = 10$ at $\beta = 1\%$, pressure profile p#2 and toroidal current density given by $J'(s)/J'_{norm} = 0.440 * (1 - s^{2.5})^2$. $q$ decreases with $\delta$; the three curves in the middle plot represent $q$ at $\delta = 0.01$, $\delta = 0.115$ (last unstable $\omega^2$) and $\delta = 0.145$ (first unstable $\omega^2$ after the stability window). For this last value $q_{min} = q_{edge} < 1$. $q_{axis}$ barely changes with $\delta$.

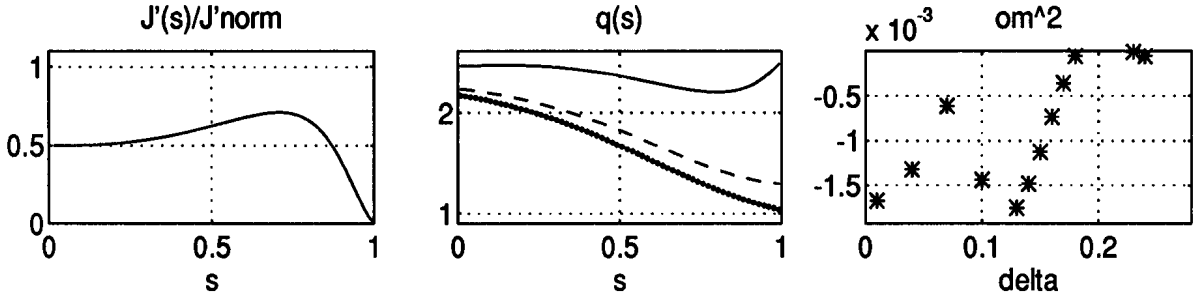


**Fig.2** The same as above for $L = 2, N_{per} = 5, 1/\epsilon = 5$, $\beta = 1\%$, pressure profile p#1 and toroidal current density given by $J'(s)/J'_{norm} = 0.9 * (1 - s^{10})^2 - 0.4 * (1 - s^{2.5})^2$. $q$ is represented for $\delta = 0.010$, $\delta = 0.180$ and $\delta = 0.230$; $q_{axis}$ decreasses with $\delta$. For $\delta$=0.010 and 0.040 the (3,1) mode dominates, at $\delta$=0.070 the (3,1) and (2,1) modes have comparable amplitudes, for $0.100 \leq \delta < 0.180$ the (2,1) mode dominates and finaly for $\delta \geq 0.230$ (last two points) the (1,1) mode sets off.

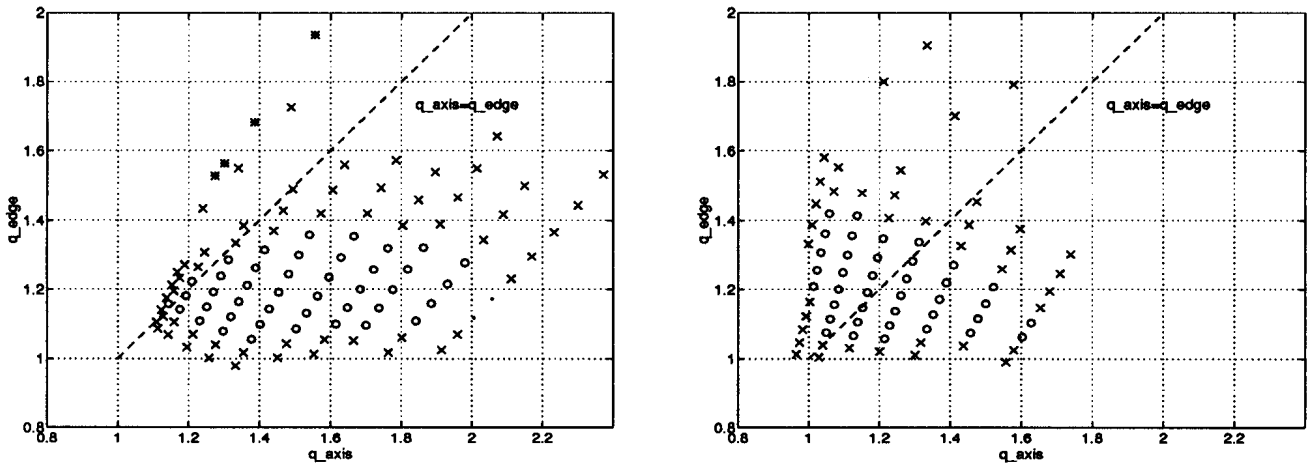


**Fig.3,4 Left plot:** stability area for the $(2,1)$ mode for equilibria with $L = 2, N_{per} = 5, 1/\epsilon = 10$, $\beta = 1\%$, pressure profile p#2 and toroidal current densities having the form $J'(s)/J'_{norm} = a_1 * (1 - s^{20})^8$. Each oblique line corresponds to a fixed $a_1$ value and represent $(q_{axis}, q_{edge})$ pairs at different $\delta$'s. Unstable points are represented with the labels $\times$, stable points byo and $*$ correspond to the circular tokamak $\delta = 0$. The stable zone gets narrower and probably will close for a smaller current. The "." marker represent a positive eigenvalue close to marginal stability. **Right plot:** all equilibrium parameters are the same with the exception of the toroidal current densities which have the form $J'(s)/J'_{norm} = a_1 * (1 - s^{1.2})^2$ .

# References

[1] S.P.Hirshman, U.Schwenn, J.Nührenberg - J. Comput. Phys. **87**, 396 (1990)

[2] S.P.Hirshman, O.Betancourt - J. Comput. Phys. **96**, 99 (1991)

[3] W.A.Cooper - "Variational formulation of the linear MHD stability of 3D Plasmas with noninteracting hot electrons" - Plasma Physics and Controlled Fusion, vol 34, No 6, pp.1011-1036, 1992

[4] D.V.Anderson, W.A.Cooper, R.Gruber, S.Merazzi, U.Schwenn - Terpsichore: a 3-dimensional ideal magnetohydrodynamic stability program - Scient. Comp. on Supercomputer II ,159 (1990)

[5] W.A.Cooper,G.Y.Fu and all - "Global external ideal MHD instabilities in 3D plasmas"- Proceedings of the joint Varenna-Lausanne international workshop, (1990) p.165

[6] C.Nuhrenberg - Physics of Plasmas **3** (1996) p 2401

# Stabilisation of ballooning modes in torsatrons with an externally applied toroidal current

W. A. Cooper

*CRPP/EPFL, Association Euratom-Confédération Suisse, Lausanne,Switzerland*

It has been found that ideal ballooning modes can impose very restrictive volume average $\beta$ limits in torsatrons[1–4] much below the typical values close to 5% that are required to be economically realisable as reactor systems and it has been shown that externally applied toroidal currents that are peaked can destabilise the Mercier criterion in this type of configuration.[5] We will show here that if the applied currents are hollow, they can stabilise the ballooning modes without triggering Mercier instabilities and as a result raise the limiting $\beta^*$ from 2% to 5%. We employ the fixed boundary version of the 3D VMEC equilibrium code[6] to generate 3D equilibria for a 10 field period torsatron configuration that has been previously examined with a large number of MHD stability codes.[7] We prescribe the pressure profile as $p(s) = p(0)(1-s)^2$, where $0 \leq s \leq 1$ represents the radial variable that labels the flux surfaces. The toroidal plasma current enclosed within each flux surface is prescribed as $2\pi J(s) = 2\pi J(1)(5s^4 - 4s^5)$ to obtain equilibria with peaked pressures and hollow toroidal currents. The $p(s)$ and the $2\pi J'(s)$ profiles are displayed in Fig. 1a. In VMEC, the toroidal flux function is $\Phi(s) = 0.5$. With this normalisation, we generate a hollow toroidal current sequence by choosing $2\pi J(1) = 0, -0.25, -0.5, -0.625$ and $-0.75$, and modify $p(0)$ to fix $\beta* = 5\%$. We use $\beta^* = 0.5(< p^2 > V)^{1/2} / < B^2 >$ as the figure of merit, where $< ... >$ represents a volume average and $V$ is the plasma volume. The rotational transform profiles for the sequence are shown in Fig. 1b.

We map the equilibria to Boozer magnetic coordinates[8,9] to carry out the 3D ballooning and Mercier stability investigations. The ideal ballooning eigenvalue profiles are shown in Fig. 2a. In the absence of toroidal currents, the ballooning modes are strongly unstable in the outer region of the plasma $0.5 < s < 0.85$. With finite hollow

plasma current, the instability region shrinks and marginal stability is obtained when $2\pi J(1) = -0.625$. The convergence of the ballooning eigenstructures tends to deteriorate for $s < 0.35$ and there are indications of destabilisation for $2\pi J(1) < -0.625$. The Mercier criterion profiles are displayed in Fig. 2b for $2\pi J(1) = 0$, $-0.625$ and $-0.75$. With zero current, the Mercier criterion is unstable near $s \simeq 0.6$. The toroidal plasma current stabilises these modes near this location, but destabilises them around $s < 0.3$ for $2\pi J(1) = -0.75$. The spiky nature of the Mercier criterion profiles results from the localized destabilization caused by the parallel current density singularities near mode rational surfaces.

We examine the normal curvature, the local magnetic shear and the parallel current density of the zero current configuration and the marginally stable configuration obtained with $2\pi J(1) = -0.625$. The 4 dominant Fourier components of the normal curvature show a similar structure for the two cases (Fig. 3a). The toroidal current, however, does cause the $(m = 3, n = 1)$ and $(m = 2, n = 1)$ components that destabilise the outer edge of the prolate up-down symmetric cross section within a period of the torsatron to increase (decrease) in magnitude in the outer(inner) radial part of the plasma. This effect should make outer region of the plasma more unstable which we observe <u>not</u> to be the case. The local magnetic shear amplitudes in Fig. 3b are also similar in character. The toroidal current appears to radially compress the structure reducing the shear in the edge region. This does not seem to have adverse consequences with respect to stability. The Fourier amplitudes of the parallel current density display the most consequent difference between the two cases. The $(m = 1, 2, 3; n = 0)$ components are similar except for a slight radial compression. However, the finite toroidal current constitutes a significant $(m = 0, n = 0)$ component in the outer part of the plasma. This term exercises a strong stabilising influence in the energy principle.[10]

In conclusion, we have demonstrated that a hollow toroidal plasma current that increses the edge rotational transform from 1.2 to 1.5 can strongly stabilise ballooning modes in a 10 period torsatron configuration. The limiting $\beta^* = 2\%$ for zero toroidal current can be increased to $\beta^* = 5\%$.

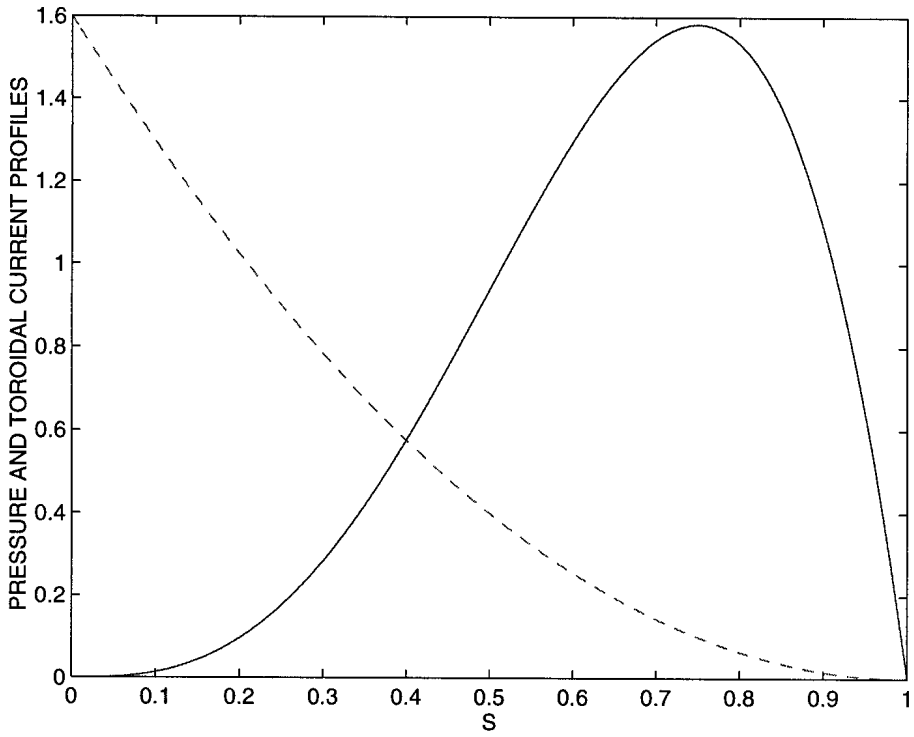


Fig. 1a. The pressure profile given by $p(s) = p(0)(1-s)^2$ and (dashed line) the toroidal plasma current profile $-2\pi J'(s)$ (solid line) that results from prescribing $2\pi J(s) = 2\pi J(1)(5s^4 - 4s^5)$. This case corresponds to $2\pi J(1) = -0.75$.

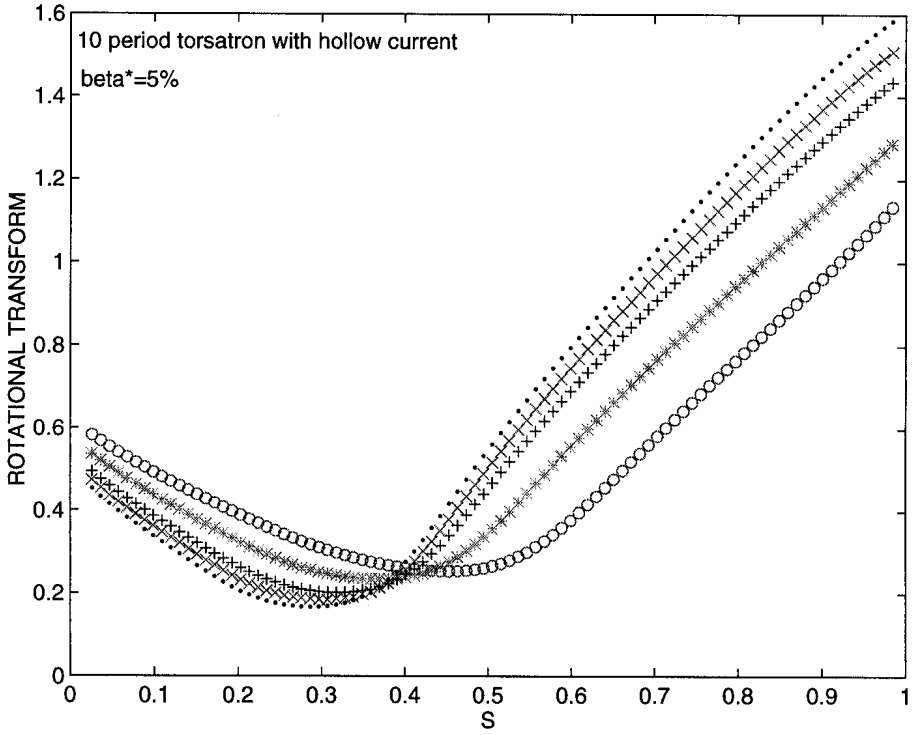


Fig. 1b. The rotational transform profiles in a 10 field period torsatron sequence with hollow toroidal plasma current profiles for $\beta^* = 5\%$. The cases examined have toroidal currents $2\pi J(1)$ of $0(o)$, $-0.25(*)$, $-0.5(+)$, $-0.625(x)$ and $-0.75(.)$.

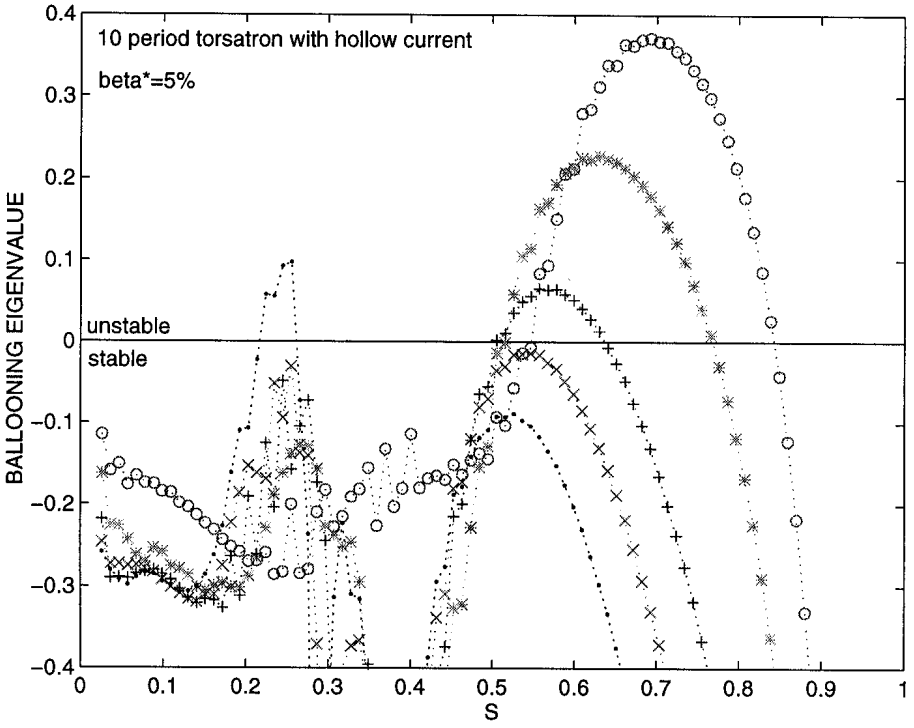


Fig. 2a. The ballooning eigenvalues as a function of the radial variable $s$ on a field line that crosses the outer edge of the prolate up-down symmetric cross section in a 10 field period torsatron sequence with hollow toroidal plasma current profiles. The cases examined have toroidal currents $2\pi J(1)$ of $0(o)$, $-0.25(*)$, $-0.5(+)$, $-0.625(x)$ and $-0.75(.)$.

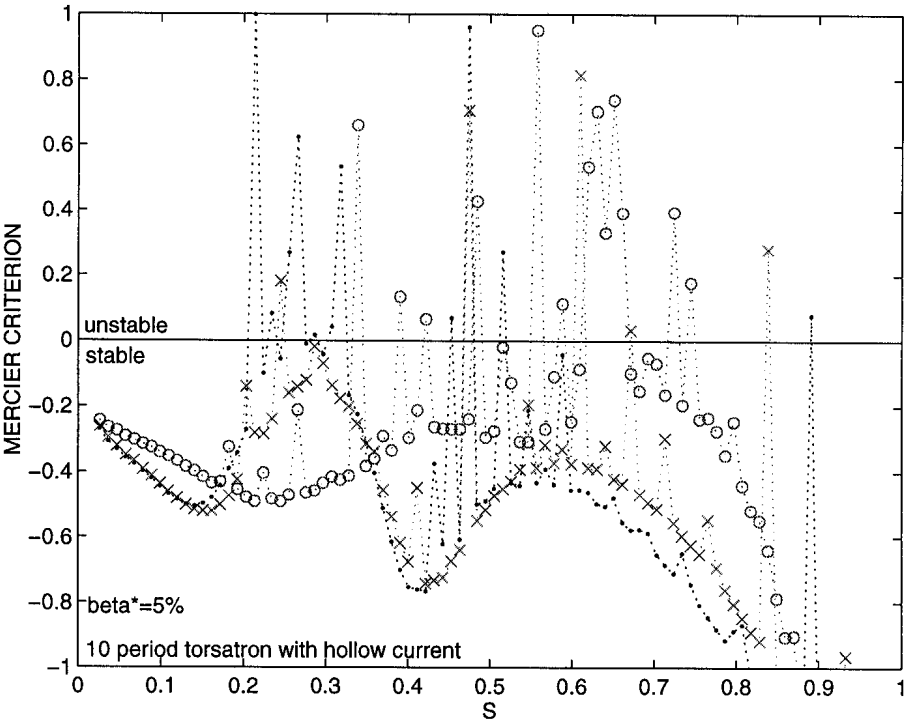


Fig. 2b. The Mercier criterion as a function of the radial variable $s$ in a 10 field period torsatron sequence with hollow toroidal plasma current profiles. The cases examined have toroidal currents $2\pi J(1)$ of $0(o)$, $-0.625(x)$ and $-0.75(.)$.

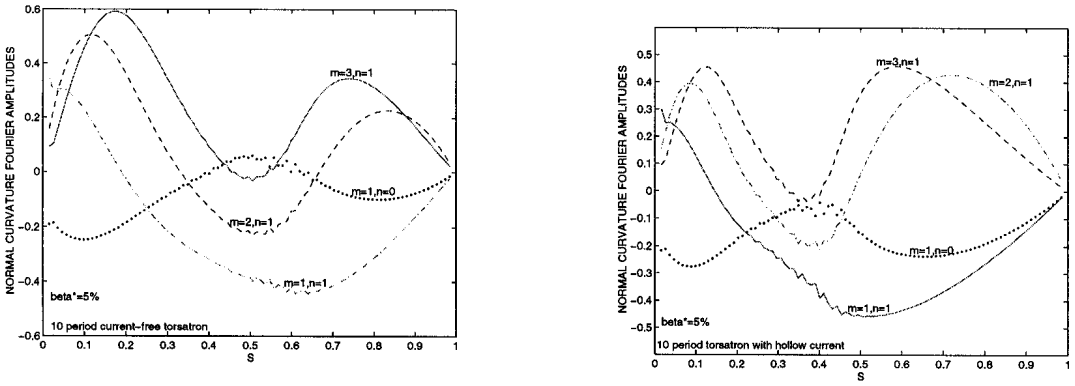


Fig. 3a. The profiles of the 4 dominant Fourier amplitudes of the normal magnetic field line curvature in a 10 field period torsatron with zero net toroidal current (left) and with a hollow toroidal current profile with $2\pi J(1) = -0.625$ (right).

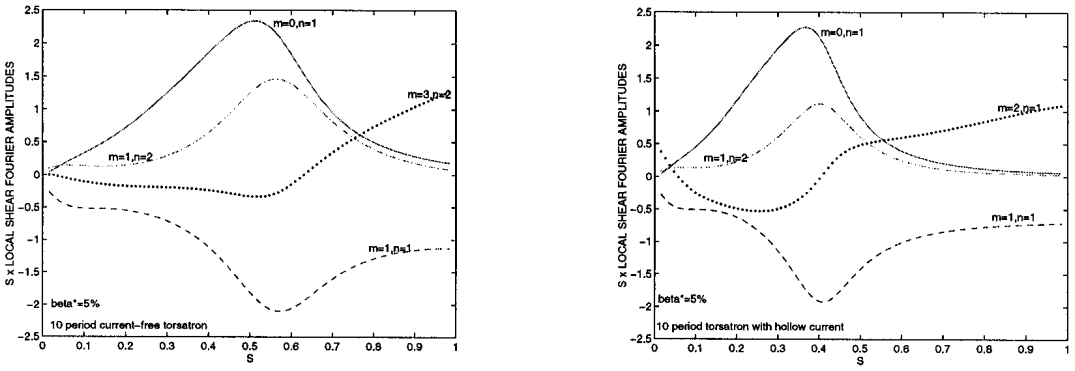


Fig. 3b. The profiles of the 4 dominant Fourier amplitudes of $s\times$ the local magnetic shear in a 10 field period torsatron with zero net toroidal current (left) and with a hollow toroidal current profile with $2\pi J(1) = -0.625$ (right).

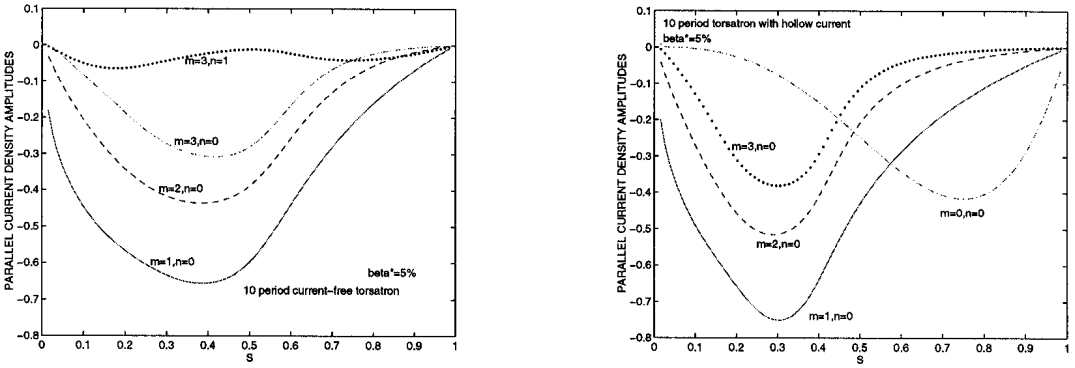


Fig. 3c. The profiles of the 4 dominant Fourier amplitudes of the parallel current density in a 10 field period torsatron with zero net toroidal current (left) and with a hollow toroidal current profile with $2\pi J(1) = -0.625$ (right).

# REFERENCES

[1] W.A. Cooper, Y. Nakamura, M. Wakatani, R. Gruber, S. Merazzi, D.V. Anderson, and U. Schwenn, in "Proc. 19th EPS Conf. on Controlled Fusion and Plasma Physics, Innsbruck 1992", Europhysics Conference Abstracts, Vol. 16C, p.557, European Physical Society (1992).

[2] R. Moeckli and W.A. Cooper, Nucl. Fusion **33**, 1899 (1993).

[3] N. Dominguez and V.E. Lynch, *Absence of Second Stability in ATF*, Oak Ridge National Laboratory Report ORNL/TM-13040 (1995).

[4] N. Nakajima, *High-mode-number ballooning modes in a heliotron/torsatron system: II. Stability*, Institute of Fusion Studies Report IFSR No.750 (1996).

[5] K. Ichiguchi, N. Nakajima, M. Okamoto, Y. Nakamura, and M. Wakatani, Nucl. Fusion **33**, 481 (1993).

[6] S.P. Hirshman and O. Betancourt, J. Comput. Phys. **96**, 99 (1991).

[7] Y. Nakamura, T. Matsumoto, M. Wakatani, S.A. Galkin. V.V. Drozdov, A.A. Martynov, Yu.Yu. Poshekhnonov, K. Ichiguchi, L. García, B.A. Carreras, C. Nührenberg (née Schwab), W.A. Cooper, and J.L. Johnson, *Comparison of the calculations of the stability properties of a specific stellarator equilibrium with different MHD stability codes*, accepted for publication in J. Comput. Phys.; Princeton Plasma Physics Laboratory Report PPPL-3092 (1995).

[8] A.H. Boozer, Phys. Fluids **23**,904 (1980).

[9] J. Nührenberg and R. Zille, *Equilibrium and stability of low-shear stellarators* in "Theory of Fusion Plasmas," A. Bondeson, E. Sindoni, and F. Troyon eds. (Soc. Ital. Fisica – Editrice Compositori, Bologna, 1988) pp. 3–23.

[10] W.A. Cooper, *Normal curvature, local magnetic shear and parallel current density in tokamaks and torsatrons*, submitted to Phys. Plasmas.; LRP report 549/96 (1996).

# Numerical $\Delta'$ studies of the nonlinear finite-$\beta$ tearing mode

A. Pletzer

*Centre de Recherches en Physique des Plasmas, Association Euratom - Confédération Suisse*

*PPB - Ecublens, CH-1015 Lausanne, Switzerland (pletzer@crpp.epfl.ch)*

## I. INTRODUCTION

Tearing modes have recently attracted attention following theoretical successes in predicting the presence of magnetic islands [1] with moderate poloidal $m = 3, 4$ and toroidal $n = 2, 3$ mode numbers during TFTR (Tokamak Fusion Test Reactor) supershots.

Classical linear resistive mode theory [2] predicts instability when the asymptotic matching index $\Delta'$ defined as the jump of logarithmic derivative of the radial magnetic perturbation across the rational surface is positive. Recently, it was suggested [3,4] that tearing modes could also persist when $\Delta' < 0$ provided bootstrap current effects are taken into account. In all the above theories, the crucial parameter which determines the stability from both the geometry and equilibrium profiles is $\Delta'$. It is shown in the present study that the $\Delta'$ of the $(m = 2, n = 1)$ mode computed with the PEST-3 code [5,6] is virtually always positive. Saturation can nevertheless be achieved provided the symmetry breaking term of a current gradient is included in the resistive layer.

## II. $\Delta'$ IN THE REDUCED MHD LIMIT

The outer, ideal region, radial magnetic field perturbations $\Psi$ are governed in the large aspect, low $\beta$ and circular cross-section limit by the equation

$$\frac{1}{r}\frac{d}{dr}r\frac{d\Psi}{dr} - \frac{\lambda(r)}{r(r-r_s)}\Psi - \frac{m^2}{r^2}\Psi = 0 \qquad (1)$$

where $\lambda(x) \equiv Rq_s j'(x)(x-1)/(B_z[q_s/q(x)-1])$ is proportional to the current gradient $j'(r)$, $x \equiv r/r_s$ is the radial coordinate normalized to the rational surface position $r_s$, $B_z$ is the constant equilibrium magnetic field, $R$ is the major radius and $q(r)$ the safety factor profile. Exact solutions of (1) exist for $\lambda = \text{const}$,

$$\Psi_< = x^m F(a_-, a_+, 1+2m|x) \qquad (x<1)$$
$$\Psi_{>\pm} = x^{\pm m} F(a_\mp, -a_\pm, 1\mp 2m\nu|1/x) \qquad (x>1)$$

in terms of hypergeometric functions $F(a,b,c|x)$, where $a_\pm = m(1\pm\nu)$ and $\nu \equiv \sqrt{1+\lambda/m^2}$. The two solutions $\Psi_{>\pm}$ are combined to give $\Psi = 0$ at the conducting wall position $x = a/r_s$. In the vicinity of $x=1$, the solution expansion

$$\Psi = 1 + \lambda(x-1)\log|x-1| + O(x-1) + O((x-1)^2\log|x-1|). \tag{2}$$

involves logarithmic terms in addition to a power series. The matching data on either side of $x=1$ are

$$r_s\Delta_\pm \equiv \lim_{x\to 1\pm} \frac{d\Psi/dx}{\Psi} \qquad \text{with} \qquad \Delta' \equiv \Delta_+ - \Delta_-. \tag{3}$$

Note that $\Delta_\pm \to \pm\infty$ but the difference $\Delta'$ is well defined. For a conducting wall at infinity,

$$\begin{aligned} r_s\Delta_- &= m - \frac{\lambda}{1+2m}\frac{F(1+a_-, 1+a_+, 2+2m|1-)}{F(a_-, a_+, 1+2m|1)} \\ r_s\Delta_+ &= -m\nu - \frac{\lambda}{1+2\nu}\frac{F(1+a_+, 1-a_-, 2+2m\nu|1-)}{F(a_+, -a_-, 1+2m\nu|1)} \end{aligned} \tag{4}$$

from which it is readily seen that $r_s\Delta' \to -2m$ as $\lambda/m \to 0$. Expressions (4) agree with the zero-$\beta$ analytic formula $r_s\Delta' = -\pi\lambda \mathrm{ctg}(\pi\lambda/2m)$ of Ref.7 as $\lambda/m \to 0$ but give a larger threshold than $2m$ for ideal instability: $\Delta' \to \infty$ as $\lambda \to 2m+1$.

For the sake of comparing (4) with the toroidal PEST-3 results, we also solve numerically (1) after prescribing the $q = q_0(1+\alpha x^{2p})^{1/p}$ profile by adjusting the three parameters $q_0$, $q_a$ and $p$, $\alpha \equiv (q_a/q_0 - 1)^p - 1$, which determine $j'(x) = -2\alpha B_z x^{2p-1}(2p+1-\alpha x^{2p})/[Rq_0(1+\alpha x^{2p})^{2+1/p}]$ and therefore $\lambda(x)$. The value $p=5$ was found to give a flat $q$ profile from the axis to $r/a \approx 0.7$ and then monotonically increasing. This profile reproduces the PEST-3 profile obtained from a zeros-$\beta$ numerical equilibrium with inverse aspect ratio $\epsilon = 0.01$ to within $\pm 1\%$. The following five cases are considered with $q_s = 2$:

| case | $q_0$ | $q_a$ | $r_s/a$ | $\lambda_s$ |
|---|---|---|---|---|
| I | 1.24 | 2.20 | 0.953 | 0.0994 |
| II | 1.35 | 2.40 | 0.909 | 0.707 |
| III | 1.47 | 2.60 | 0.867 | 1.55 |
| IV | 1.64 | 2.90 | 0.802 | 3.39 |
| V | 1.92 | 3.40 | 0.651 | 8.73 |

(5)

The $\lambda$ profile is bell-shaped with its maximum value, at $r/a \approx 0.7$, increasing from 5 to 9 for cases I to V, respectively. The large increase in $\lambda_s \equiv \lambda(r_s)$ noticeable from case I to V is thus mainly due to the rational surface moving inwards.

Figure 1 shows the comparison between analytic (a) and numerical (b-c) calculations of $r_s\Delta'$ for the poloidal modes $m$ = 2, 4, 6 , 8, 10, 14 and 20. The destabilizing effect of increasing $\lambda$ can be observed, as well as $r_s\Delta'$ tending asymptotically to $-2m$ when $m \to \infty$ except for case (b,I) which suffers from numerical inaccuracies due to the proximity of the wall from $r_s$ (PEST-3 is less sensitive in that respect because it uses the flux coordinate as independent variable). The differences between cases (b) and (c) are otherwise due to small differences in the equilibrium profiles, which tend to be more pronounced when looking at the current profile. The stabilizing effect of the wall is apparent for profile I: $r_s\Delta'$ is negative and lies well below the $-2m$ asymptote even for $m \sim 20$.

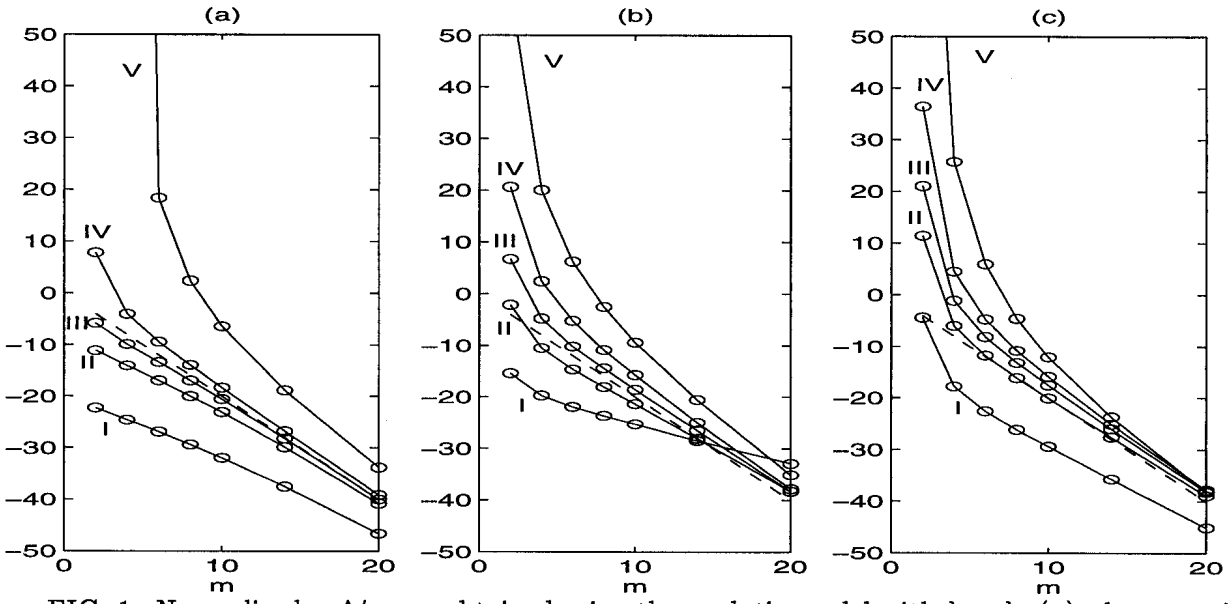


FIG. 1. Normalized $r_s\Delta'$ vs $m$ obtained using the analytic model with $\lambda = \lambda_s$ (a), the numerical model with the prescribed $q$ profile (b) and PEST-3 (c) for the five cases I-V. The asymptote $-2m$ is shown in dashed line.

## III. FINITE ASPECT RATIO AND SHAPING

The effect of varying the inverse aspect ratio $\epsilon$ on $\Delta'$ for the ($m$ = 2,$n$ = 1) mode in a plasma of elongation $E$ = 1.7 and triangularity $T$ = 0.3, is studied while imposing the

safety factor $q = 1.05$ constant on axis. The current profile is flat from the axis to the 30% flux surface, and then decreases monotonically to zero. A triangular pressure profile (in poloidal flux coordinate) is adopted with volume averaged $\beta = 3.5\%$ at $\epsilon = 0.3$ (Troyon factor $g = 2.6$).

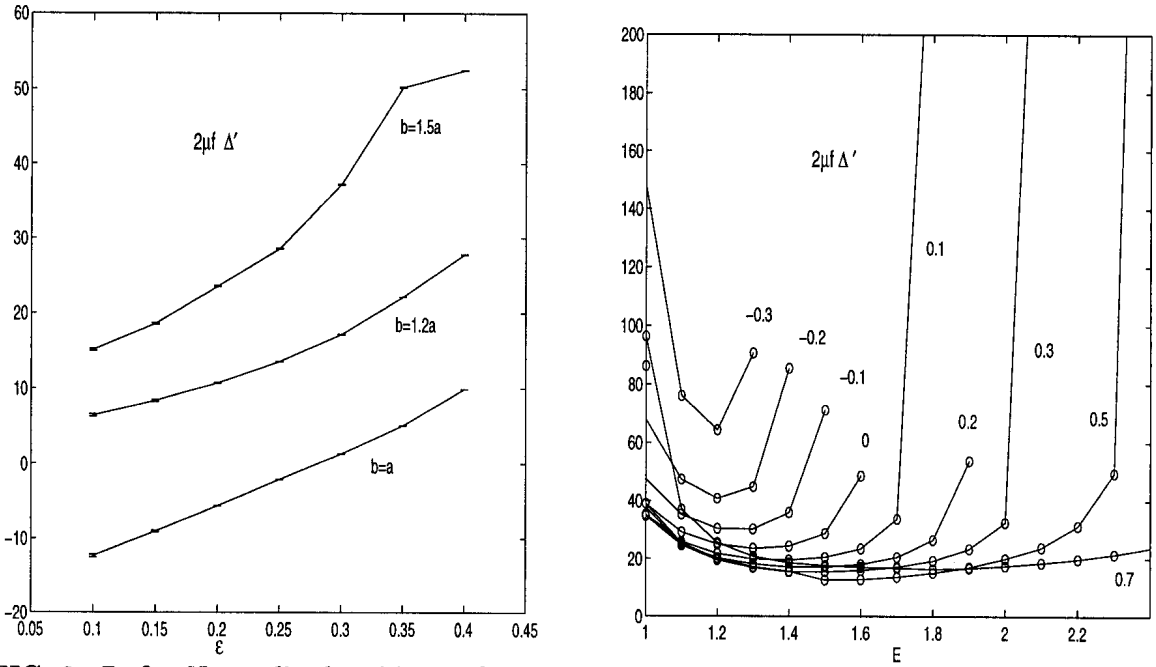


FIG. 2. **Left:** Normalized $r_s\Delta'$ vs $\epsilon$ for the $E = 1.7$ and $T = 0.3$ equilibrium. A conducting wall is applied at distance $b = a$, $b = 1.2a$ and $b = 1.5a$. **Right:** The PEST-3 matching data $2\mu f\Delta'$ (see appendix) vs triangularity $T$ and elongation $E$.

It is seen in Fig. 2 (left) that a compact torus is more $\Delta'$ unstable (i.e. more positive $\Delta'$) than a large aspect ratio tokamak when allowing $\beta \propto \epsilon^2$ ($g \sim \epsilon$). Due to its exterior location, the $(2,1)$ mode is sensitive to the wall position $b$. In Fig. 2 (right), elongation $E$ and triangularity $T$ are varied at fixed $\epsilon = 0.3$ and $b = 1.2a$. Here we have $\beta$ approximately $\propto E$ ($g \sim$ constant) and $\Delta' \to \infty$ when the ideal stability limit is reached.

## IV. NONLINEAR SATURATION MODEL

The stability of small resonant perturbations $\Psi(X,t)\cos m\hat{\theta}$ of the helical flux $\psi_h \equiv \frac{1}{(2\pi)^2}\int d\tau \boldsymbol{B}\cdot\boldsymbol{\nabla}\hat{\theta}$ ($\hat{\theta}$ is the helical angle $\theta - m\zeta/n$ whereas $\theta$ and $\zeta$ are respectively the poloidal and toroidal angles) is governed in toroidal geometry by the Kotschenreuther *et al.* (KHM)

equation [8]

$$\frac{\partial^2}{\partial X^2}\Psi\cos m\hat{\theta} = \frac{\overline{|\nabla\chi|_i^{-2}}}{\eta}\frac{\partial}{\partial t}\Psi\left\langle\cos m\hat{\theta}\right\rangle + G_1 p'(\psi_h)(X - < X >)$$
$$-G_2\mathcal{L}p'(\psi_h)\frac{\partial\Psi}{\partial X}\left\langle\cos m\hat{\theta}\right\rangle + G_2\left(Xp'(\psi_h) + \mathcal{L}p_i'\right) + \frac{\kappa}{\mathcal{L}}(X - < X >) \qquad (6)$$

to which a current gradient term $\kappa(X - < X >)/\mathcal{L}$ has been added. Here, $X \equiv \chi - \chi_i$ is the distance from the rational surface in poloidal flux coordinate, $\mathcal{L} \equiv q_i/q_i'$, $\eta$ is the resistivity, $p(\psi_h)$ is the total of equilibrium and perturbed pressure, $\langle\cdot\rangle \equiv \oint_{\psi_h} d\hat{\theta}\,(\partial_X\psi_h)^{-1}\cdot\Big/\oint_{\psi_h} d\hat{\theta}\,(\partial_X\psi_h)^{-1}$ is the weighted average along iso-$\psi_h$ lines, $p_i'\mathcal{L}^2G_1 \approx E + F$ and $p_i'\mathcal{L}^2G_2 \approx H$ are related to the Glasser *et al.* [9] coefficients of the inner layer. Primes denote derivation with respect to $\chi$ and subscripts $i$ indicate evaluation at the rational surface $\chi_i$. Equation (6) incorporates the minimal number of ingredients to get a singular equation

$$\frac{\partial^2}{\partial X^2}\Psi + \left(D_I + \frac{1}{4}\right)\frac{\Psi}{X^2} - \kappa\frac{\Psi}{X} = 0 \qquad (7)$$

in the large $X$ limit, with $D_I \equiv E + F + H - \frac{1}{4}$ the ideal Mercier index. Solutions of (7) $\sim X^{\frac{1}{2}\pm\mu}$ can be matched to those computed by PEST-3 ($\mu \equiv \sqrt{-D_I}$). [Compare (7) to (1) in the vicinity of $r = r_s$ after taking $D_I = -\frac{1}{4}$ and substituting $\kappa$ by $\lambda\partial r/\partial\chi$].

Allowing for symmetry breaking perturbations, we write [10]

$$\Psi \equiv \Psi_0 + \Psi_\pm' X \qquad (\Psi' = \Psi_+' \text{ for } X > 0, \text{ resp. } \Psi' = \Psi_-' \text{ for } X < 0) \qquad (8)$$

and take $(1/\Psi_0\pi)\int_{-\infty}^{\infty} dX \int_{-\pi}^{\pi} d\hat{\theta}\cos m\hat{\theta}$ of (6) to obtain (after some manipulations) an evolution equation for the island width $W \equiv 4|\mathcal{L}\Psi_0|^{\frac{1}{2}}$ in terms of the matching data $(\Psi_+' \pm \Psi_-')/\Psi_0$. The critical step is to recognize that the exponent $\frac{3}{2}-\mu$ of the first order term in the Frobenius expansion of the large solution $\frac{|X|^{1/2-\mu}}{2\mu f}\left(1 - \frac{\kappa X}{1-2\mu} + \cdots\right)$ has almost the same power as the zeroth order of the small solution $\frac{\Delta'}{2}|X|^{1/2+\mu} + \frac{\Gamma'}{2}|X|^{1/2+\mu}\mathrm{sgn}(X)$ when $\mu$ approaches $\frac{1}{2}$ (see appendix for the definition of the normalization $2\mu f$ in PEST-3). These two terms produce the familiar logarithmic terms of (2) in the zero-$\beta$ limit, $|X|^{1/2-\mu} \approx |X|^{-1/2+\mu} + (1-2\mu)\ln|X|$. Matching to nonlinear solutions at $X = \pm W/2$ then gives

$$\frac{\Psi_+' - \Psi_-'}{\Psi_0} \to \Delta' + \mathrm{O}(1-2\mu) \quad \text{and} \quad \frac{\Psi_+' + \Psi_-'}{\Psi_0} \to \tilde{\Gamma}' + \frac{\kappa}{\mu f}\ln\left|\frac{W}{2\chi_a}\right| + \mathrm{O}(1-2\mu) \qquad (9)$$

where $\tilde{\Gamma}' \equiv \Gamma' - \kappa/[2\mu f(\mu - \frac{1}{2})] \sim O(1)$ is the renormalized matching index of ballooning parity that is well behaved as $\beta \to 0$. The logarithmic term in (9) has previously been obtained [11] in the large aspect ratio, $\beta \to 0$ limit. An equation determining the equilibrium island width from the "dispersion relation"

$$\Delta' = -\frac{1}{2\mu f}\left(k_2 \frac{D}{W} + k_1 \kappa^2 W \ln\left|\frac{W}{2\chi_a}\right|\right) - k_1 \kappa W \frac{\tilde{\Gamma}'}{2} \tag{10}$$

can then be derived, with $k_1 \approx 0.82$, $k_2 \approx 6$ and $\chi_a$ the flux coordinate at the edge.

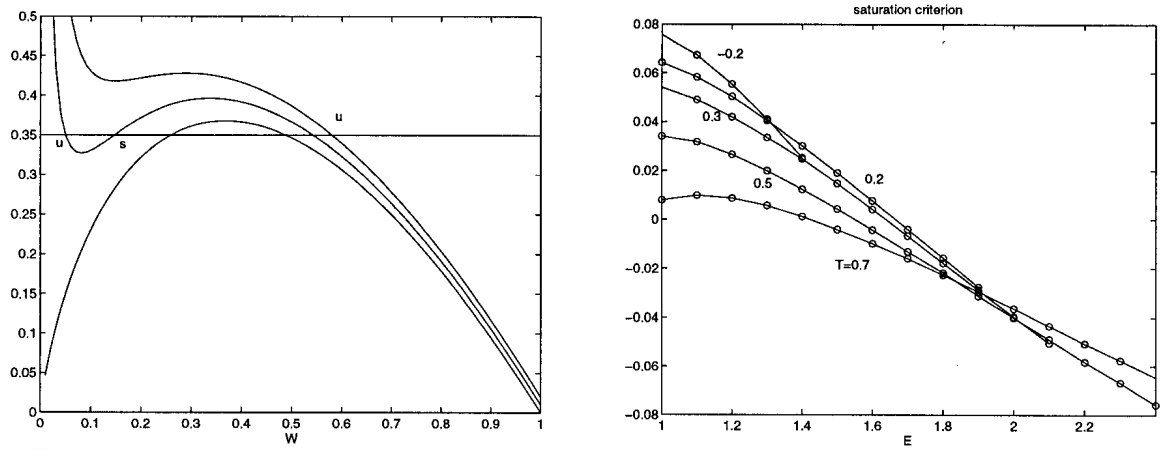


FIG. 3. **Left:** Schematic representation of $\Delta' = \Delta(W)$ for given $\Delta'$ (horizontal line). The lower curve corresponds to $\beta = 0$. The upper curves represent the effect of an increasingly negative resistive Mercier function. Stable and unstable fixed points are labelled by "s", respectively "u". **Right:** The saturation criterion expressing the non-monotonicity of $\Delta(W)$ vs $E$ and $T$ for $\epsilon = 0.3$ is violated in the positive domain ($\tilde{\Gamma}'$ was assumed to be negligible).

Figure 3 (left) shows a succession of fixed points for the $\beta = 0$ case: stable at $W_1 > 0$ and unstable at $W_2 > W_1$ (stability corresponds to $d\Delta/dW > 0$). A stable fixed point arises at $W = 0$ and an unstable one $0 < W < W_1$ for $D < 0$. For $D$ and $\tilde{\Gamma}$ small,

$$-D \lesssim \frac{k_1}{k_2}\left(\frac{\kappa\chi_a}{\exp(1+\mu f\tilde{\Gamma}'/\kappa)}\right)^2 \tag{11}$$

$\Delta(W)$ is a decreasing function of $W$ with a local minimum $\check{\Delta}$ and maximum $\hat{\Delta}$ [neglecting $O(D^2)$ terms]. The widths for which $\Delta(W)$ has a local minimum $\Delta(\check{W}) \equiv \check{\Delta}$, respectively a maximum $\Delta(\hat{W}) \equiv \hat{\Delta}$, can be estimated to be

$$\hat{W} \approx \frac{\chi_a}{\exp(1+\mu f\tilde{\Gamma}'/\kappa)}\left[1 + \sqrt{1 + \frac{k_2 D}{k_1}\left(\frac{\exp(1+\mu f\tilde{\Gamma}'/\kappa)}{\kappa\chi_a}\right)^2}\right]$$

$$\check{W} \approx -\frac{1}{2}\frac{k_2 D}{k_1}\left(\frac{\exp(1+\mu f\tilde{\Gamma}'/\kappa)}{\kappa\chi_a}\right)^2$$

so that the condition for a stable saturated island simply reads $\check{\Delta}\tilde{<}\Delta'\tilde{<}\hat{\Delta}$. This window is however generally quite small unless $\tilde{\Gamma}'$ is negative. At present, PEST-3 does not provide an accurate estimate of $\tilde{\Gamma}'$ so that (11) could only be determined assuming this term to be recessive in (10). Figure 3 (right) shows that (11) is satisfied for elongations larger than 1.6 regardless of the triangularity.

## V. DISCUSSION

The matching index at $q = 2$ computed by PEST-3 has been compared with an analytic model in the reduced MHD limit. The $\Delta'$ obtained with PEST-3 were found to be more unstable (positive) than their analytical counterparts, except for one case with large current gradient. Positive $\Delta'$ values have been found up to $(m = 6, n = 3)$.

The finite $\beta$ $\Delta'$ is destabilized by increasing the inverse aspect ratio while keeping $q$ on axis constant. Triangularity is always stabilizing. Small elongations of $1 - 1.2$ are stabilizing but larger values tend to be destabilizing. A positive, minimum value of $\Delta'$ has been located at elongation 1.6 and triangularity 0.3.

The Kotschenreuther *et al.* (KHM) nonlinear tearing mode model has been extended to include current gradient effects. These are important because the matching to outer region solutions would otherwise be incorrect (no singularity). It also changes the bifurcation picture: the island width of the unstable KHM equilibrium is reduced and new (stable and unstable) fixed points appear provided (11) is satisfied and $\Delta' > 0$.

The code PEST-3 has been extensively used in order to identify regimes in the current, pressure, elongation and triangulation parameter space, where saturation is achievable. The work by Carrera *et al.* [3] suggests that the bootstrap current effect competes with the Glasser stabilization, thereby facilitating the achievement for saturation. This effect has not been taken into account in this work.

This work was partly supported by the Swiss National Science Foundation.

## APPENDIX: NORMALIZATION OF $\Delta'$ IN PEST-3

The matching data are computed in PEST-3 from the expression

$$\frac{1}{2}\Delta' = W(\check{\xi},\check{\xi}) + \frac{1}{2}(\hat{\xi}, L\hat{\xi}) \tag{A1}$$

where $W(\xi,\xi)$ is the symmetric ideal energy functional, ( , ) denotes integration over the plasma volume and $L\xi \equiv \mathcal{J}\nabla\chi\cdot(\mathbf{F}\cdot\boldsymbol{\xi})|/\nabla\chi|^2$ is the MHD force operator applying on the normal displacement field $\xi \equiv \boldsymbol{\xi}\cdot\nabla\chi$. The functions $\hat{\xi}$ and $\check{\xi}$ approximately capture

$$\hat{\xi} \sim \frac{|x|^{-\frac{1}{2}-\mu}\mathrm{sgn}(x)}{2\mu f} \qquad \check{\xi} \sim \frac{1}{2}\Delta'|x|^{-\frac{1}{2}+\mu}\mathrm{sgn}(x) + \frac{1}{2}\Gamma'|x|^{-\frac{1}{2}+\mu} \tag{A2}$$

the large and small solutions behaviour about the rational surface $\chi_i$, $x \equiv \chi - \chi_i$, with $L(\hat{\xi}+\check{\xi}) = 0$. The coefficient $f = \frac{4\pi^2 n^2 q'^2}{<m|-\mathcal{J}\nabla\cdot\nabla_s|m>}$, where $\nabla_s$ is the surface gradient lying on a magnetic surface, is a convenient normalization factor used in PEST-3 to ensure that the $\Delta'$ form a Hermitian matrix in the multi-rational surface case.

Considering transformation on the dependent variable $\partial_\chi \rightarrow \chi_\rho^{-1}\partial_\rho$, we observe that since $f \sim \mathcal{J}^{-1}$ is inversely proportional to the Jacobian, $f \rightarrow \chi_\rho^{-1} f$, $\hat{\xi} \rightarrow \chi_\rho\hat{\xi}$, $\check{\xi} \rightarrow \chi_\rho\check{\xi}$ and $\Delta' \rightarrow \chi_\rho^2\Delta'$. The normalized $\Delta'$ representing the ratio of small to large solution being $\chi_i^{2\mu f}(2\mu f)\Delta'$, we then find the normalized $\Delta'$ expressed in radial coordinate to be

$$r_s(2\mu f)\frac{d\chi}{dr}\Delta' = \frac{(2\mu f)^2}{4\pi^2}R\frac{{q_i}^2}{{q_i'}^2}\Delta' \tag{A3}$$

in the large aspect ratio, zero $\beta$ and circular cross-section limit.


1. Z. Chang, Phys. Rev. Lett. **74**, 4663 (1995).
2. H. P. Furth, J. Killeen, and M. N. Rosenbluth, Phys. Fluids **6**, 459 (1963).
3. R. Carrera, R. D. Hazeltine, and M. Kotschenreuther, Phys. Fluids **29**, 899 (1986).
4. C. C. Hegna and J. D. Callen, Phys. Plasmas **1**, 3135 (1994).
5. A. Pletzer and R. L. Dewar, J. Plasma Phys. **45**, 427 (1991).
6. A. Pletzer, A. Bondeson, and R. L. Dewar, J. Comput. Phys. **115**, 530 (1994).
7. C. C. Hegna and J. D. Callen, Phys. Plasmas **1**, 2308 (1994).
8. M. Kotschenreuther, R. D. Hazeltine, and P. J. Morrison, Phys. Fluids **28**, 294 (1985).
9. A. H. Glasser, J. M. Greene, and J. L. Johnson, Phys. Fluids **18**, 875 (1975).
10. L. E. Zakharov *et al.*, Sov. J. Plasma Phys. **16**, 451 (1991).
11. A. Thyagaraja, Phys. Fluids **24**, 1716 (1981).

# Resistive Wall Stabilization by Toroidal Rotation: Effects of Partial Wall Configurations and Aspect Ratio

D. J. Ward

Centre de Recherches en Physique des Plasmas, Association Euratom - Confédération Suisse,
Ecole Polytechnique Fédérale de Lausanne, CH-1015 Lausanne, Switzerland

## I. Introduction

Numerical calculations [1,2] have shown that it is possible to stabilize pressure-driven kink modes, where the value for $\beta$ (the ratio of the plasma particle pressure to the magnetic field pressure) is above the Troyon limit, in a tokamak plasma surrounded by a resistive wall given sufficient toroidal rotation. Experimental results [3,4] have confirmed this stabilizing effect.

There are, in fact, two modes which must be stabilized simultaneously [1,2]: (1) the ideal "plasma mode", and (2) the "resistive wall mode". The plasma mode is stable when the wall separation is less than the marginal position for stability with an ideally conducting wall. The resistive wall mode is stable for a given (sufficient) rotation when the wall separation is larger than some marginal value. This results in a region of stability, in terms of wall position, for a given rotation speed. Increasing the rotation speed moves the marginal position for stability to the resistive wall mode closer to the plasma, thus widening the stability region. Conversely, by moving the resistive wall farther from the plasma (but remaining always within the marginal ideal wall threshold), the resistive wall mode can be stabilized at a lower rotation speed.

Introducing gaps in the wall has much the same effect as moving the wall farther away, in that it is easier to stabilize the resistive wall mode (i.e., the resistive wall mode can be stabilized at a lower rotation speed). For pressure-driven external kink modes, the instability couples most strongly to the wall at the outboard midplane. Therefore, toroidally continuous gaps near the outboard midplane can have a very strong effect. This effect moves the region of stability, in terms of wall position, closer to the plasma and reduces it in extent, but allows stabilization to be reached at a lower rotation speed. This effectively makes wall stabilization more accessible.

Toroidal coupling between different poloidal harmonics and between the Alfvén and sound waves complicates the effect of rotation on pressure-driven modes. Rotation modifies the eigenfunction at resonances near the rational surfaces, and calculations indicate [2,4] that additional rational surfaces, particularly those in regions of relatively high pressure, make the stabilization more effective. The effect of lower aspect ratio, which increases toroidal coupling and the number of rational surfaces residing in the plasma, on resistive wall stabilization will be examined in Section III.

## II. Partial Wall Configurations

Because of the importance of wall stabilization for advanced tokamak equilibria [5] (that is, equilibria with reverse-shear, high-$\beta$, high bootstrap fraction) we will focus on such equilibria in this section. The equilibrium considered here is a reverse-shear equilibrium used in calculations presented in Ref. [2]. This particular equilibrium is identical to that in Fig. 9 of Ref. [2] at $\beta^* = 5.2\%$ ($\beta^*$ is the rms value of $\beta$, i.e., $\beta^* \equiv 2\mu_0\langle p^2\rangle^{1/2}/\langle B^2\rangle$). This equilibrium is very similar to the equilibria described in Ref. [5]. It has $q_0 = 2.5$, $q_{min} \approx 2.2$, $q_S = 4.1$, high $\beta^*$, and a bootstrap fraction of nearly unity with the bootstrap current well aligned with the total plasma current. It is stable everywhere to ballooning modes and has good stability properties with respect to various microinstabilities [5], but is unstable to the low-$n$ pressure driven, external kink. In the absence of a conducting wall, the limit in $\beta^*$ is 2.49%.

**Figure 1**

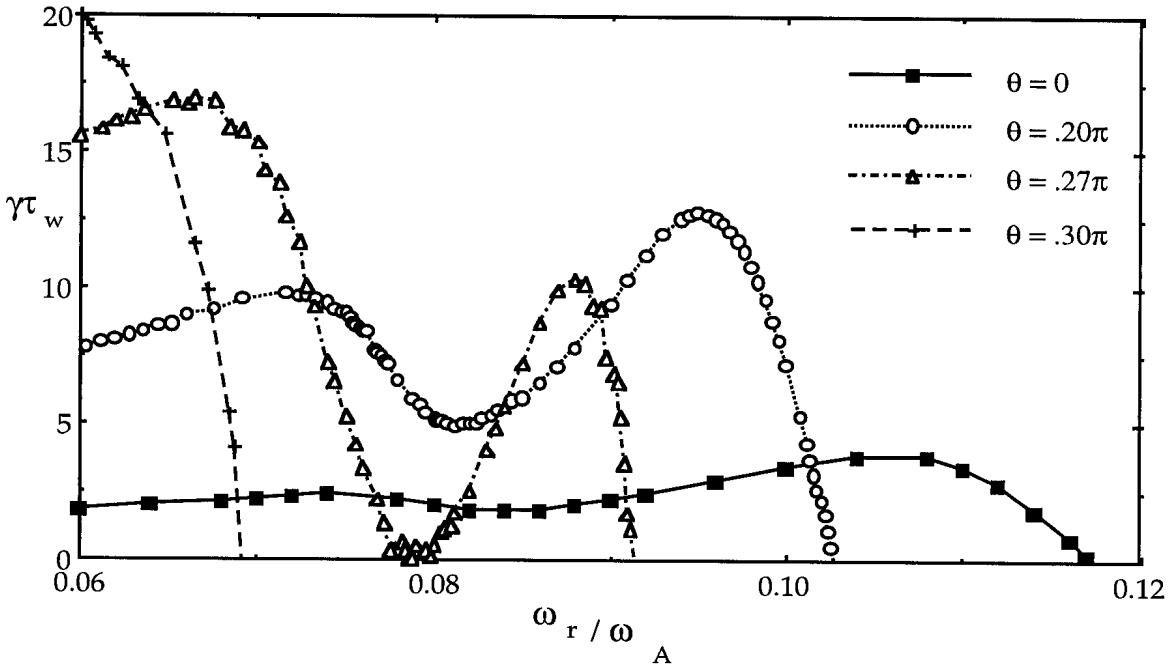


Figure 1 shows the results with a wall separation of $d/a = 1.04$ and with gaps in the wall centered at the *outboard* midplane with half-widths of $\theta_g = 0.2\pi$, $\theta_g = 0.27\pi$, and a slightly larger gap of $\theta_g = 0.3\pi$, as well as for $\theta_g = 0$ (full wall). For $\theta_g = 0.2\pi$, the threshold rotation frequency above which the resistive wall mode is stabilized is $\omega_r/\omega_A \approx 0.103$ — a reduction of 13% from the case with a full wall. For a somewhat larger outboard gap of half-

width $\theta_g = 0.27\pi$, the threshold rotation frequency is $\omega_r/\omega_A \approx 0.092$ — a 22% reduction from the case with a full wall.

Figure 1 shows that the threshold value of stability of $\omega_r$ for the case with an outboard gap of $\theta_g = 0.3\pi$ is $\omega_r/\omega_A \approx 0.069$. This is a reduction of 41% of the necessary rotation frequency to stabilize compared to the case with a full wall. The necessary wall separation needed to stabilize the ideal plasma mode is $d/a = 1.06$ for the case with an outboard gap of $\theta_g = 0.3\pi$, compared to $d/a = 1.36$ for the full wall. This results in the need to have the wall somewhat closer in order to stabilize the ideal plasma mode when there is such a gap, but there is a significant reduction in the necessary rotation to stabilize the resistive wall mode.

## II.A. Wall Stabilization with Discrete Conducting Plates

In the Tokamak Physics Experiment (TPX) design [6] passive stabilization against the axisymmetric, vertical instability and against the ideal external kink is provided by conducting plates on the inboard and outboard sides. In fact, the passive structure is not quite axisymmetric and actually takes the form of a three-dimensional "cage". But it can be approximated as two pairs of axisymmetric plates. A resistive wall on the inboard side has very little effect on the pressure-driven kink mode in high-$\beta$ equilibria, therefore the inboard plates will be ignored in the following calculations. The calculations use a pair of conformal wall sections on the outboard side with the same poloidal angular extent as the outboard TPX plates (from $|\theta| = 0.18\pi$ to $|\theta| = 0.48\pi$).

The results are shown in Fig. 2. The growth rates are normalized to the same wall time (calculated for a complete resistive wall) as in Fig. 1. There we see that the growth rates are considerably higher than for the cases in Fig. 1, particularly in the peak just short of the critical rotation frequency for stabilization. But we see that stabilization occurs at a much lower rotation frequency. In fact, the necessary critical frequency for stabilization is reduced by a factor of aprroximately 3.6 compared to the case with a complete wall with the same plasma-wall separation (with a full wall at $d/a = 1.04$ there is stabilization at $\omega_r/\omega_A \approx 0.12$).

Therefore we see that a large outboard gap, or even limiting the nearby conducting structure to a pair of discrete plates, can have a beneficial effect on the stabilization of the resistive wall mode by lowering the necessary rotation speed by a significant factor. There is, of course, a trade-off in that in order to also stabilize the ideal plasma mode (and both modes must be stabilized at the same time), the maximum plasma wall separation is reduced. However, this it is well understood that any configuration must be stable with an *ideal* wall. These results show that for a configuration with close fitting plates, or a wall with a large

outboard gap, the necessary rotation speed for stabilization of the resistive wall mode is greatly reduced compared to that which would be necessary with a continuous, completely surrounding resistive wall.

**Figure 2**

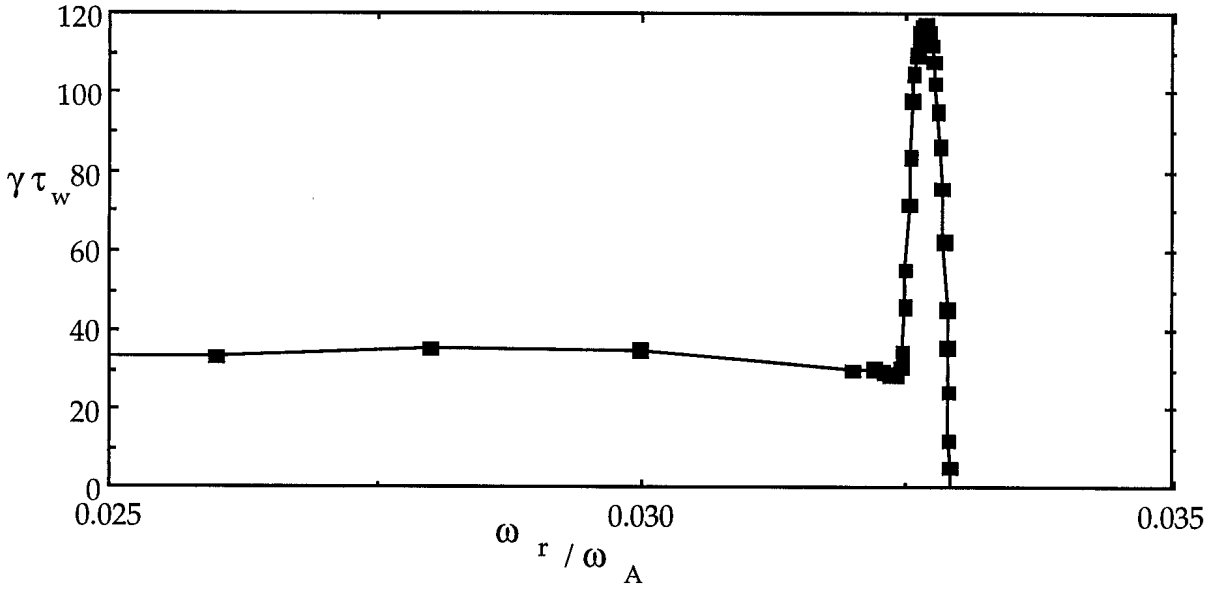


## III. Resistive Wall Stabilization of Low-Aspect-Ratio Tokamaks

The stabilization of resistive wall modes by toroidal rotation requires resonant surfaces inside the plasma [1,2], and toroidicity plays an important role in this stabilizing effect. Previous results [2] have shown that a larger number of rational surfaces in the plasma ehances this stabilizing effect. It seems likely, therefore, that resistive wall stabilization may be more effective for low aspect ratio, in which toroidal effects are enhanced, and in which a large number of rational surfaces naturally reside in the plasma.

Table 1 shows the results of resistive wall calculations at various aspect ratios. The table lists characteristics of the equilibria such as inverse aspect ratio $\varepsilon$, values of $\beta$ and $\beta^*$, the normalized values of beta ($g$ and $g^*$), the ratio of the normalized beta for the equilibrium to that for the equilibrium which is marginally stable to the free-boundary kink mode ($g/g_{lim}$), $q$ at the surface, the growth rate (without rotation) normalized to the wall time (for a wall at $d/a$ = 1.05), the ideal wall position for marginal stability, and finally the value of rotation that stabilizes the resistive wall mode (for a wall at $d/a$ = 1.05). A scan was made of the aspect ratios $\varepsilon$ = 0.3, 0.6, and 0.7, the definition for the profiles was kept the same, and the magnitude of the pressure varied to make equilibria that are unstable to the pressure-driven kink. The values for the marginally stable ($g/g_{lim}$ = 1.00) equilibria are also shown for those three aspect ratios.

We see that the magnitude of $\gamma\tau_w$ (without rotation) and the value of $d/a(ideal)$ are both good measures of the strength the instability, and are inversely correlated. As the instability becomes stronger (higher growth rate) it takes a larger rotation speed to stabilize it. Therefore it is quite striking that at the higher values of ε (0.6 and 0.7) the equilibria listed here are very unstable (by a factor of over thirty, in one case, over the ε = 0.3 unstable equilibrium), and yet the necessary rotation speed is quite comparable to that required to stabilize the ε = 0.3 case. Note that the equilibria in the aspect-ratio scan are not optimized, and thus the equilbria at low aspect ratio are considerably more unstable than for the higher aspect ratio cases.

Table 1: Aspect-ratio scan

| ε=1/A | $\beta$ | $\beta^*$ | $g$ | $g^*$ | $g/g_{lim}$ | $q_s$ | $\gamma\tau_w$ | $d/a(ideal)$ | $\omega_s/\omega_A$ |
|---|---|---|---|---|---|---|---|---|---|
| 0.3 | 5.153 | 5.848 | 2.67 | 3.03 | 1.00 | 4.12 | 0.00 | $\infty$ | 0.00 |
| 0.3 | 6.026 | 6.841 | 3.165 | 3.593 | 1.185 | 4.279 | 1.33 | 1.44 | 0.0236 |
| 0.6 | 14.05 | 15.98 | 4.17 | 4.74 | 1.00 | 9.05 | 0.00 | $\infty$ | 0.00 |
| 0.6 | 15.28 | 17.35 | 4.638 | 5.267 | 1.112 | 9.493 | 2.78 | 1.275 | 0.0182 |
| 0.6 | 17.26 | 19.61 | 5.49 | 6.237 | 1.316 | 10.41 | 12.44 | 1.112 | 0.035 |
| 0.7 | 18.13 | 20.60 | 5.285 | 6.003 | 1.00 | 15.99 | 0.00 | $\infty$ | 0.00 |
| 0.7 | 18.72 | 21.27 | 5.557 | 6.314 | 1.052 | 16.67 | 42.75 | 1.07 | 0.0312 |
| 0.7 | 19.78 | 22.48 | 6.083 | 6.915 | 1.151 | 18.18 | 24.17 | 1.092 | 0.0144 |
| 0.714 | 40.59 | 43.59 | 6.313 | 6.780 | N/A | 14.83 | 2.735 | 1.26 | 0.0047 |

The final equilibrium listed in Table 1 (ε = 0.714) is a highly optimized (to give high beta and near unity bootstrap fraction) low-aspect-ratio equilibrium developed by R. L. Miller, et al. [7]. In this case very high values of beta are achieved ($\beta_X$ = 55%, where $\beta_X \equiv 2\mu_0\langle p\rangle/B_0^2$ — here, $B_0$ is the magnetic field at the axis, following the convention commonly used for defining beta at low aspect ratio), and yet the passive growth rate is only $\gamma\tau_w$ = 2.735, and the equilbrium is completely stabilized (with a wall separation of $d/a$ = 1.05) at a normalized rotation speed of less than 0.005. Figure 3 shows the normalized growth rate for this case with respect to normalized rotation speed. Therefore, we see that this highly optimized, high-$\beta$ equilibrium is stabilized at quite modest values of rotation speed.

Figure 3

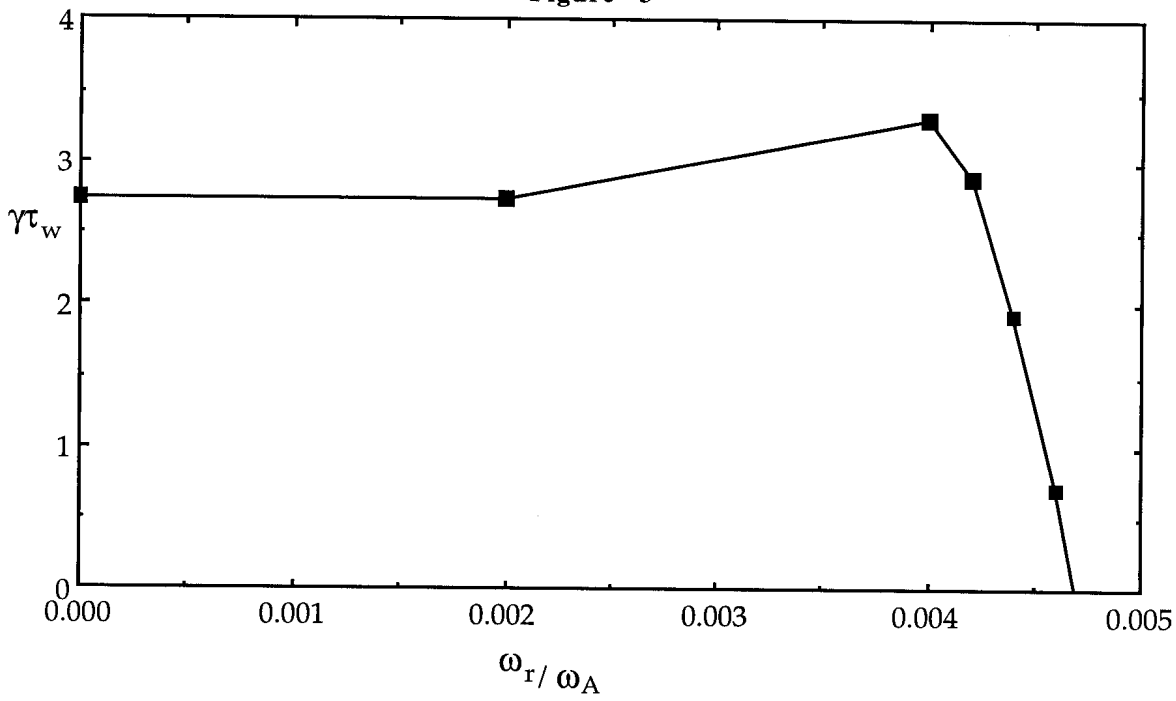


## Summary

Results have been presented which demonstrate that with a pair of close-fitting conducting plates, which leave a large gap at the outboard midplane, a high-$\beta$ equilibrium at conventional aspect ratio can be stabilized at a rotation speed reduced by a factor of over 3.5 compared to a fully surrounding, continuous and complete wall at the same separation. Results were also presented which show that low-aspect-ratio equilibria can be stabilized at significantly lower rotation speeds than at conventional aspect ratio. These two effects can perhaps be combined to enhance even further the effect of resistive wall stabilization at low aspect ratio.

## Acknowledgements

I would like to thank R. L. Miller and O. Sauter for useful discussions and for providing the optimized low-aspect-ratio equilibrium used in Section III. This work was supported by the Fonds National Suisse pour la Recherche Scientifique.

## References

[1] A. Bondeson and D. J. Ward, Phys. Rev. Lett. **72** (1994) 2709.
[2] D. J. Ward and A. Bondeson, Phys. Plasmas **2** (1995) 1570.
[3] E. J. Strait, et al., Phys. Rev. Lett. **74** (1995) 2483.
[4] M. Okabayashi, et al., to appear in Nucl. Fusion **36** (1996).
[5] C. Kessel, J. Manickam, G. Rewoldt, W. M. Tang, Phys. Rev. Lett. **72** (1994) 1212.
[6] R. Goldston, et al., Contr. Fusion and Plasma Phys., Proc. 20th European Conference, Lisboa, 1993 (Europ. Phys. Soc., Petit-Lancy, Switzerland, 1993) Vol. 17C, Pt. I, p. 319.
[7] R.L. Miller, these proceedings; and R. L. Miller, et al., G.A. Report, GA-A22321, July 1996; submitted to Phys. Plasmas.

# Free-boundary Ideal MHD Modes in W7-AS

PETER MERKEL, CAROLIN NÜHRENBERG

*Max-Planck-Institut für Plasmaphysik, Teilinstitut Greifswald*
*IPP-EURATOM Association, 17493 Greifswald, Germany*

and

W. A. COOPER

*Centre de Recherches en Physique des Plasmas, Association Euratom-Confédération Suisse*
*Ecole Polytechnique Fédérale de Lausanne, Lausanne, Switzerland*

## ABSTRACT

The CAS3D stability code may now be used to analyze the ideal magnetohydrodynamic energy principle for three-dimensional plasmas surrounded by a vacuum region, i.e. for perturbations which may deform the plasma-vacuum interface because of a non-vanishing normal component on this surface. A Green's function technique is used here to determine the vacuum energy contribution from a surface integral with the plasma-vacuum interface as domain of integration. Assets of this procedure are that it does not require to continue either the coordinate system nor the perturbation functions into the vacuum region. The application of the CAS3D free-boundary stability code to a set of finite-$\beta$ W7-AS plasma configurations, computationally generated from the W7-AS coil data, shows that unstable, radially extended free-boundary modes exist in equilibria of this set, for which the local Mercier stability criterion detects stability. This is in contrast to the behaviour of the fixed-boundary modes, for which the point of marginal stability approximately coincides with the one given by the local stability analysis. Corresponding results from the TERPSICHORE and CAS3D codes are in good agreement.

## I. INTRODUCTION

Since the CAS3D stability code [1] proved to be a valuable tool for the investigation of the ideal magnetohydrodynamic (MHD) stability properties of three-dimensional (3D) toroidal plasmas [2], it was desirable to remove its limitation to the fixed-boundary approach. The extension to the free-boundary stability problem, i.e. for perturbations which may deform the plasma-vaccum interface of a plasma surrounded by a vacuum region, should of course follow the guidelines which were adopted in the construction of the CAS3D code, which means that also the treatment of the vacuum part should take care of the truly 3D geometry of stellarator configurations. This may be accomplished with the help of a Green's function technique [3, 4], which has already proved useful in the computation of 3D free-boundary MHD equilibria with the NEMEC equilibrium code [5]. Figure 1 shows the boundary of a W7-AS [6] type plasma region demonstrating its 3D nature.

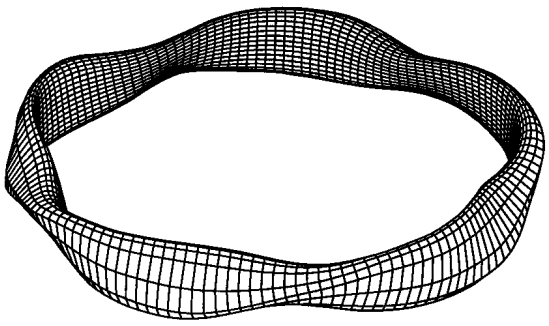

**Fig. 1.** *Plasma region for a truly 3D stability problem: Outer magnetic surface for a W7-AS equilibrium, as spanned by a field line with* $\iota = 8/23 \approx 1/3$. *For this case the ratio of the vertical magnetic field to the main field is* $\approx 0.015$

This paper is arranged as follows. Section II gives a brief review of the ideal MHD energy principle. Section III describes the treatment of the vacuum part with the Green's function technique. In Sec. IV applications to a set of equilibria, which were computed with the NEMEC code from the W7-AS modular coils, are discussed. Section V gives the conclusions.

## II. IDEAL MHD ENERGY PRINCIPLE

The task of the CAS3D stability code is to computationally solve the ideal MHD energy principle in its variational form [7, 8]

$$\lambda W_{\rm kin}(\boldsymbol{\xi}) - W_{\rm pot}(\boldsymbol{\xi}) \longrightarrow \text{minimum!} \tag{1}$$

for general 3D toroidal plasmas. The plasma region will be denoted by $P$, the surrounding, infinite vacuum region by $V$. The plasma boundary, identical with the plasma-vacuum interface, is $S$; the outer unit normal of a magnetic surface $s = \text{const}$ — on $S$ this is s=1 — is $\mathbf{n} = |\nabla s|^{-1}\nabla s$. In the following all the symbols have their usual meaning, compare Ref. 1. If necessary, plasma quantities are given the subscript P, and vacuum quantities are denoted by V. In the linearized stability theory, which is employed here, a subscript 1 indicates a first order perturbed quantity.

In Eq. (1) $W_{\rm kin}$ is the kinetic energy and $W_{\rm pot}$ the potential energy connected to the displacement vector $\boldsymbol{\xi}$, and $\lambda$ is the corresponding eigenvalue. A negative $\lambda_{\rm min}$, in its magnitude depending on the normalization given by $W_{\rm kin}$, indicates an MHD unstable equilibrium.

Following Ref. 7, the potential energy is the sum of three terms, $W_{\rm pot}= W_{\rm P}+W_{\rm V}+W_{\rm S}$. The contribution of the plasma region is $W_{\rm P}$,

$$W_{\rm P} = \frac{1}{2}\iiint_{\rm P} {\rm d}^3r\left[{\rm C}^2 + \gamma p\,(\nabla\cdot\boldsymbol{\xi})^2 - \mathcal{A}(\boldsymbol{\xi}\cdot\nabla s)^2\right] \quad . \tag{2}$$

The task of the fixed-boundary CAS3D code [1] is the numerical minimization of $W_{\rm P}$ formulated in magnetic coordinates $(s,\theta,\phi)$ [9, 10, 11] within a set of suitably normalized displacements, which have a vanishing normal component on the plasma boundary, $\boldsymbol{\xi}\cdot\nabla s = 0$. For the free-boundary version this boundary condition is not present; therefore the vacuum energy and the plasma-vacuum interface energy terms, $W_{\rm V}$ and $W_{\rm S}$, which vanish for fixed-boundary modes, may give non-zero contributions. The vacuum energy term is

$$W_{\rm V} = \frac{1}{2}\iiint_{\rm V} {\rm d}^3r|\mathbf{B}_{\rm V1}|^2 \tag{3}$$

with $\mathbf{B}_{\rm V1}$ the first order perturbed magnetic field in the vacuum region. In the so-called pseudo-plasma-vacuum technique [12,13] $W_{\rm V}$ is used as given by Eq. (3), the vacuum is treated as a shear- and pressureless pseudo-plasma, and the perturbation functions and the coordinate system are continued to the vacuum region. As a consequence the algebraic eigenvalue, which results from Eq. (1), increases in size, which is already $\mathcal{O}(10^4)$ for a medium-sized problem in the fixed-boundary case.

With the Green's function technique (see Sec. III) this is avoided, the computation area of the stability investigation is limited to the plasma region and its boundary. The contribution of the plasma-vacuum interface is $W_S$,

$$W_S = \frac{1}{2}\iint_S \mathrm{d}\mathbf{f} \cdot \boldsymbol{\nabla}\left[p + \frac{1}{2}B_P^2 - \frac{1}{2}B_V^2\right]|\nabla s|^{-2}(\boldsymbol{\xi}\cdot\boldsymbol{\nabla}s)^2 \quad . \tag{4}$$

For equilibria, which have been computed with the 3D MHD equilibrium code NEMEC [5], $W_S$ of Eq. (4) vanishes, since this code determines free-boundary equilibria with a continuous total pressure on the plasma-vacuum interface. Furthermore, also otherwise $W_S$ may be omitted from the stability investigation, since any equilibrium magnetic field can be analytically continued into the vacuum region, so that the condition

$$p + \frac{1}{2}B_P^2 - \frac{1}{2}B_V^2 = 0 \quad \text{on} \quad S \tag{5}$$

is fulfilled. Because of Eq. (3) the equilibrium vacuum magnetic field, $\mathbf{B}_V$, does not contribute to the vacuum energy.

## III. VACUUM ENERGY CONTRIBUTION

A Green's function technique is used here to determine the energy contribution of Eq. (3) for an infinite vacuum region surrounding the toroidal plasma. The first order perturbed vacuum magnetic field $\mathbf{B}_{V1}$, which enters the vacuum energy in Eq. (3), satisfies

$$\boldsymbol{\nabla}\cdot\mathbf{B}_{V1} = 0 \qquad \text{and} \qquad \boldsymbol{\nabla}\times\mathbf{B}_{V1} = 0 \quad . \tag{6}$$

With the outer unit normal being $\mathbf{n}$, the boundary condition on the plasma-vacuum interface is

$$\mathbf{n}\cdot\mathbf{B}_{V1} = \mathbf{n}\cdot\mathbf{B}_{P1} = \mathbf{n}\cdot\boldsymbol{\nabla}\times(\boldsymbol{\xi}\times\mathbf{B}_P) = |\boldsymbol{\nabla}s|^{-1}\mathbf{B}_P\cdot\boldsymbol{\nabla}(\boldsymbol{\xi}\cdot\boldsymbol{\nabla}s) \quad , \tag{7}$$

which may be obtained by utilizing the representation of the equilibrium magnetic field in magnetic coordinates with $\mathbf{B}_P\cdot\boldsymbol{\nabla}s = 0$ and $\sqrt{g}\mathbf{B}_P\cdot\boldsymbol{\nabla}\theta$ and $\sqrt{g}\mathbf{B}_P\cdot\boldsymbol{\nabla}\theta$ depending only on the flux label $s$. Because of Eq. (6) a scalar potential $\Phi$ exists for $\mathbf{B}_{V1}$ with

$$\mathbf{B}_{V1} = \boldsymbol{\nabla}\Phi \quad , \qquad \Delta\Phi = 0 \qquad \text{and} \qquad \boldsymbol{\nabla}\times\boldsymbol{\nabla}\Phi = 0 \quad . \tag{8}$$

On the plasma-vacuum interface the boundary condition for $\Phi$ is

$$\mathbf{n}\cdot\boldsymbol{\nabla}\Phi = \partial_n\Phi = |\boldsymbol{\nabla}s|^{-1}\mathbf{B}_P\cdot\boldsymbol{\nabla}(\boldsymbol{\xi}\cdot\boldsymbol{\nabla}s) \quad , \tag{9}$$

according to Eq. (7). With the help of Green's theorem the vacuum energy contribution of Eq. (3) can be converted to a surface integral with the plasma-vacuum interface as domain of integration and $\partial_n\Phi$ as given by Eq. (9),

$$W_V = \frac{1}{2}\iint_S \mathrm{d}\mathbf{f}\cdot(\Phi\boldsymbol{\nabla}\Phi) \quad . \tag{10}$$

On the plasma-vacuum interface the values of the harmonic function $\Phi$ are given by the integral equation

$$2\pi\Phi(\mathbf{r}) + \iint\limits_S \mathrm{d}\mathbf{f}' \cdot \left(\Phi(\mathbf{r}')\boldsymbol{\nabla}' G(\mathbf{r},\mathbf{r}')\right) = \iint\limits_S \mathrm{d}\mathbf{f}' \cdot \left(G(\mathbf{r},\mathbf{r}')\boldsymbol{\nabla}'\Phi(\mathbf{r}')\right) \quad , \tag{11}$$

which is obtained by transcribing $\boldsymbol{\Delta}\,\Phi = 0$ with the help of Green's theorem. Here, $G(\mathbf{r},\mathbf{r}') = |\mathbf{r}-\mathbf{r}'|^{-1}$ is the Green's function of Laplace's equation and $\mathbf{r}$ and $\mathbf{r}'$ denote position vectors for points on the plasma-vacuum interface $S$. Primed operations act on primed quantities. The right-hand-side of Eq. (11) may be considered as a source term, since it depends on the perturbation $\boldsymbol{\xi}$ by virtue of Eq. (9).

For a numerical treatment of the vacuum energy contribution the potential $\Phi$ — which is an even function, $\Phi(\theta,\phi) = \Phi(-\theta,-\phi)$, for even parity perturbations because of Eq. (9) — is approximated by a truncated double Fourier series,

$$\Phi(\theta,\phi) = \sum_{m=0}^{m_0} \sum_{n=-n_0}^{n_0} \widehat{\Phi}_{mn} \cos 2\pi(m\theta + n\overline{\phi}) \tag{12}$$

with $m_0$ and $n_0$ being the finite Fourier expansion parameters and $\overline{\phi}$ increasing by unity in one toroidal transit of the plasma region. This is equivalent to the ansatz used for the scalar components of the perturbation vector $\boldsymbol{\xi}$. Insertion of this approximation into Eq. (11) and Fourier transformation with respect to the magnetic coordinates $\theta$ and $\phi$ lead to a set of linear equations for the Fourier coefficients of the potential, $\widehat{\Phi}_{mn}$. When solving these equations, care must be taken of the singularities of the Green's function and its normal derivative. The regularization procedure [3, 4], which is applied here, follows Refs. 3 and 4 and has already succesfully been used in the computation of 3D free-boundary equilibria [5]: Subtraction of analytical functions with the same singular behaviour, but analytically calculable Fourier transforms with respect to $\theta$ and $\phi$, yields terms, which may be Fourier analyzed by standard numerical methods. The analytically obtained Fourier transforms of the regularization functions are added again in order to retain the original equations.

From Eqs. (7) and (9) it follows that the vacuum energy of Eq. (10) may be given in terms of $\boldsymbol{\xi} \cdot \boldsymbol{\nabla} s$ on the plasma-vacuum interface $S$, i.e.

$$W_{\mathrm{V}} = c_{\mathrm{S}}^t \; M_{\mathrm{V}} \; c_{\mathrm{S}} \quad , \tag{13}$$

where the real coefficient vector $c_{\mathrm{S}}$ comprises the values of the $\boldsymbol{\xi} \cdot \boldsymbol{\nabla} s$ Fourier harmonics on $S$. $M_{\mathrm{V}}$, the matrix for the vacuum energy, is real, symmetric, and non-negative. The extended algebraic eigenvalue problem

$$M_{\mathrm{pot}}\; c = \lambda M_{\mathrm{kin}}\; c \qquad \text{with} \qquad M_{\mathrm{pot}} = M_{\mathrm{P}} + \begin{pmatrix} 0 & 0 \\ 0 & M_{\mathrm{V}} \end{pmatrix} \tag{14}$$

thus includes the vacuum energy contribution; it is analyzed in the free-boundary CAS3D stability code. In Eq. (14) the '0' entries denote matrix sub-blocks with vanishing elements in a suitable block-partitioning. $M_{\mathrm{pot}}$, $M_{\mathrm{kin}}$, and $M_{\mathrm{P}}$ are the matrix equivalents of the potential, kinetic and plasma energies connected to the perturbation $\boldsymbol{\xi}$. The real coefficient vector $c$ consists of the the values of the Fourier

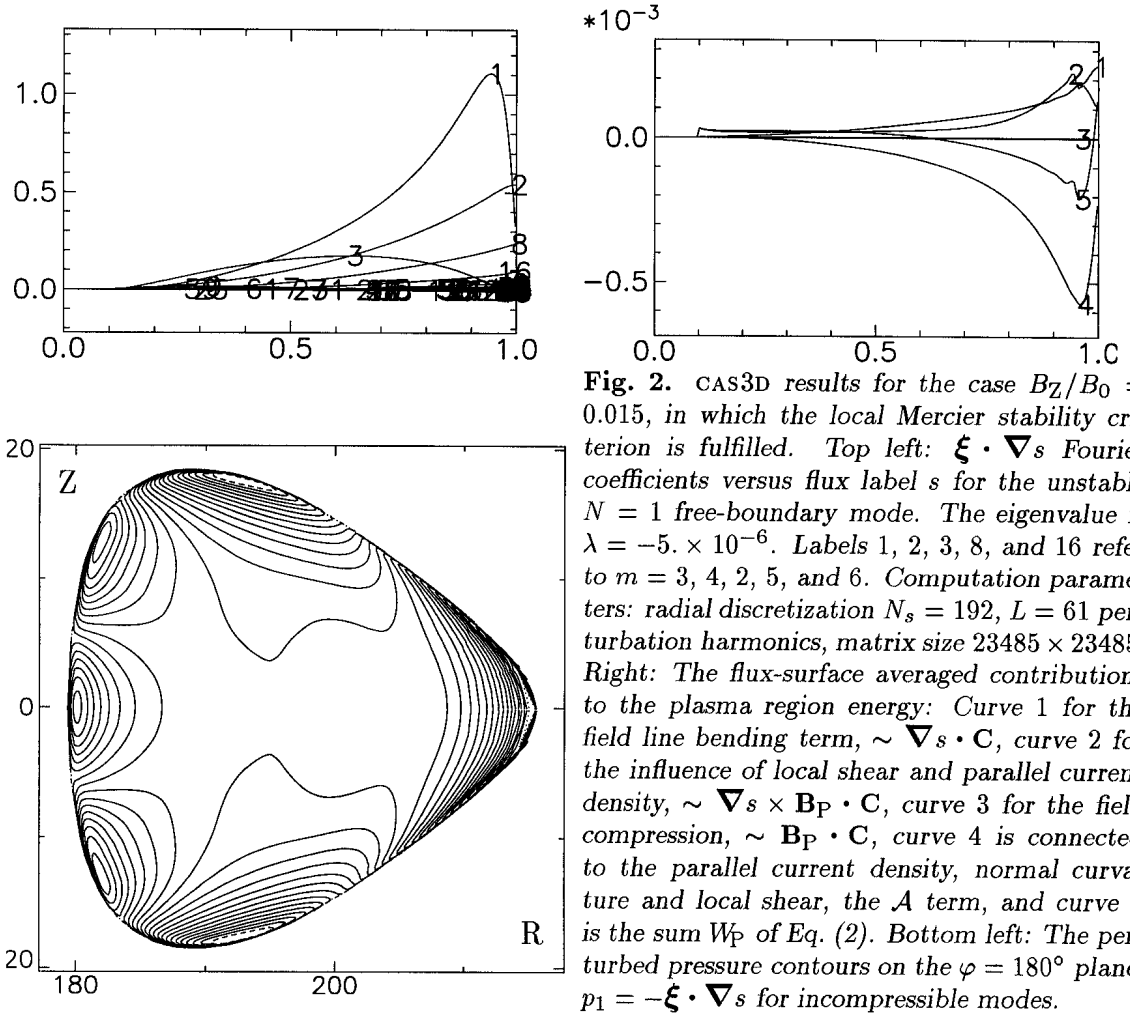


**Fig. 2.** CAS3D *results for the case* $B_Z/B_0 = 0.015$, *in which the local Mercier stability criterion is fulfilled. Top left:* $\boldsymbol{\xi} \cdot \nabla s$ *Fourier coefficients versus flux label* $s$ *for the unstable* $N = 1$ *free-boundary mode. The eigenvalue is* $\lambda = -5. \times 10^{-6}$. *Labels* 1, 2, 3, 8, *and* 16 *refer to* $m = 3$, 4, 2, 5, *and* 6. *Computation parameters: radial discretization* $N_s = 192$, $L = 61$ *perturbation harmonics, matrix size* $23485 \times 23485$. *Right: The flux-surface averaged contributions to the plasma region energy: Curve* 1 *for the field line bending term,* $\sim \nabla s \cdot \mathbf{C}$, *curve* 2 *for the influence of local shear and parallel current density,* $\sim \nabla s \times \mathbf{B}_P \cdot \mathbf{C}$, *curve* 3 *for the field compression,* $\sim \mathbf{B}_P \cdot \mathbf{C}$, *curve* 4 *is connected to the parallel current density, normal curvature and local shear, the* $\mathcal{A}$ *term, and curve* 5 *is the sum* $W_P$ *of Eq. (2). Bottom left: The perturbed pressure contours on the* $\varphi = 180°$ *plane;* $p_1 = -\boldsymbol{\xi} \cdot \nabla s$ *for incompressible modes.*

coefficients of $\boldsymbol{\xi} \cdot \nabla s$ and $\boldsymbol{\xi} \cdot \nabla s \times \mathbf{B}_P$ inside the plasma and, for $\boldsymbol{\xi} \cdot \nabla s$ only, on its boundary. From Eq. (14) it is clear that the sizes of the algebraic eigenvalue problems are identical in both the free- and fixed-boundary cases and that, since $M_V$ is symmetric, the nature of the eigenvalue problem in Eq. (14) remains unchanged.

## IV. APPLICATIONS

For a plasma configuration, which proves to be unstable against fixed-boundary global perturbations localized close to the plasma boundary, the free-boundary stability analysis is mandatory. In contrast to the purely internal global mode structure in configurations of a wider W7–X configurational neighbourhood [2, 12, 14, 15], perturbations in W7–AS type configurations tend to be boundary-localized [16]. Therefore, the stability properties of a set of W7–AS type equilibria will be discussed here. The NEMEC 3D MHD equilibrium code [5] — the VMEC equilibrium code in its free-boundary version — is used to create the input data for the stability calculation from the W7–AS coil data.

The relative magnitude of a vertical magnetic field, $B_Z$, which when superposed yields an *inward* shift of the plasma column, is used to construct a one-parametric series of equilibria. The sequence parameter $B_Z/B_0$ varies between 0.011 and 0.022. The value of the rotational transform on the plasma boundary is adjusted to $\iota_B =$

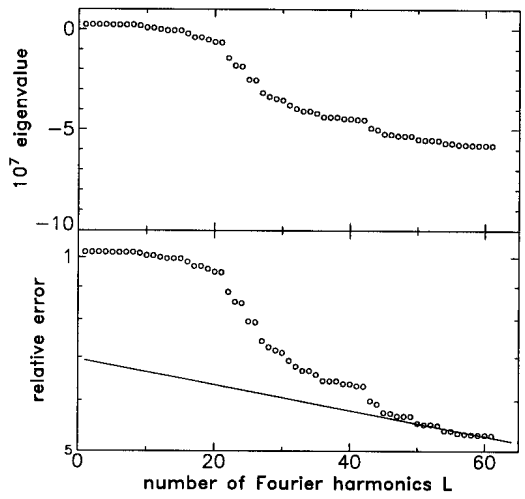


**Fig. 3.** *Eigenvalues (top frame) and relative error $[(\lambda_\infty - \lambda_{\min}(L))/\lambda_\infty$, bottom frame] versus the number of Fourier harmonics, $L$, for an $(M,N) = (3,-1)$ perturbation with a mixed type boundary condition in the case with $B_Z/B_0 = 0.02$. The number of perturbation Fourier harmonics is $2L+1$.*

| n \ m | 0 | 1 | 2 | 3 | 4 | 5 | 6 | 7 | 8 | 9 | 10 | 11 | 12 |
|---|---|---|---|---|---|---|---|---|---|---|---|---|---|
| −5 | | 57 | 61 | | | | | | | | | | |
| −4 | | 35 | 34 | | 45 | | 51 | | | | | | |
| −3 | 50 | 11 | 20 | 39 | 40 | | 37 | | 44 | | | | 43 |
| −2 | 16 | 6 | 13 | 14 | 33 | 17 | | | 27 | 32 | | | 25 |
| −1 | 8 | 3 | 31 | 23 | 22 | 7 | 19 | 28 | 55 | 21 | 24 | | 36 |
| 0 | 1 | 2 | 5 | 9 | 4 | 46 | 10 | 29 | 54 | | | | 15 |
| 1 | 18 | 30 | 12 | 58 | | | | | 56 | 59 | | | 26 |
| 2 | 52 | 48 | 38 | 41 | | 53 | | | | | | 60 | |
| 3 | | 47 | 42 | | | | | | | | | | |
| 4 | | 49 | | | | | | | | | | | |
| 5 | | | | | | | | | | | | | |

**Fig. 4.** *Set of $L = 60$ equilibrium Fourier index pairs $(m,n)$ belonging to the convergence study shown in Fig. 3. The $(m,n)$ cell numbering indicates the ordering which results from the iterative construction of this set; together with its $l-1$ preceding $(m,n)$ harmonics the component numbered $l$ contributes to the corresponding eigenvalue in the top left frame. Cells shaded in grey indicate the set of $L = 30$ Fourier indices, which, via coupling to $(3,-1)$, produce the 61 perturbation Fourier harmonics used for the computations shown in Fig. 2.*

1/3; within the sequence of equilibria this is achieved by superposition of an auxiliary toroidal magnetic field available in W7-AS.

The remaining equilibrium properties vary only slightly: On the magnetic axis the rotational transform is $\iota \approx 0.4$, i.e. the shear is small and negative. The average $\beta$ varies from $\langle\beta\rangle = 0.0148$ to 0.0112, The local Mercier stability criterion is violated in the cases with $B_Z/B_0 > 0.0165$, as seen with the JMC code [10].

Figure 2 shows CAS3D results of the stability investigation of this set of equilibria. The low-node-number free-boundary modes exhibit some important fixed-boundary-mode properties [1]: The structure of $W_P$ demands that the modes are resonant, so that because of $\iota \gtrsim 1/3$ the $m = 3$ harmonic and its poloidal side bands are dominant in the $N = 1$ perturbation, as may be seen in the top left frame of Fig. 2. The investigation of the various energy contributions to $W_{pot}$ shows, that also for the free-boundary modes the field compression term $B_P^{-2}\mathbf{B}_P \cdot \mathbf{C}$ [compare Eq. (2)] vanishes to a very good approximation (see curve 3 in the right frame of Fig. 2). In this case, as in all unstable cases of this series, the perturbation is radially extended with the maximum magnitudes near the plasma boundary. These properties are also visible in the perturbed pressure contours on meridional cuts, $p_1 = -\boldsymbol{\xi}\cdot\nabla s$ for incompressible modes; see Fig. 2 (bottom left frame) for the plot of the $\varphi = 180°$ plane for the $B_Z/B_0 = 0.015$ case. Since the shear is small, only few ($\sim 5$ out of a total of 61, compare Fig. 4) Fourier harmonics dominate the perturbation spectrum. However, a detailed convergence study on the eigenvalue behaviour under an increasing number of perturbation Fourier harmonics shows that, at least $\approx 25$ harmonics of $\boldsymbol{\xi}\cdot\nabla s$ must be used in order to obtain a negative eigenvalue. As may be seen in Fig. 3, approximately converged eigenvalues require $\gtrsim 60$ harmonics.

The calculation for the $B_Z/B_0 = 0.015$ case also shows that the specific free-boundary mode treated here is unstable, even though the local Mercier stability

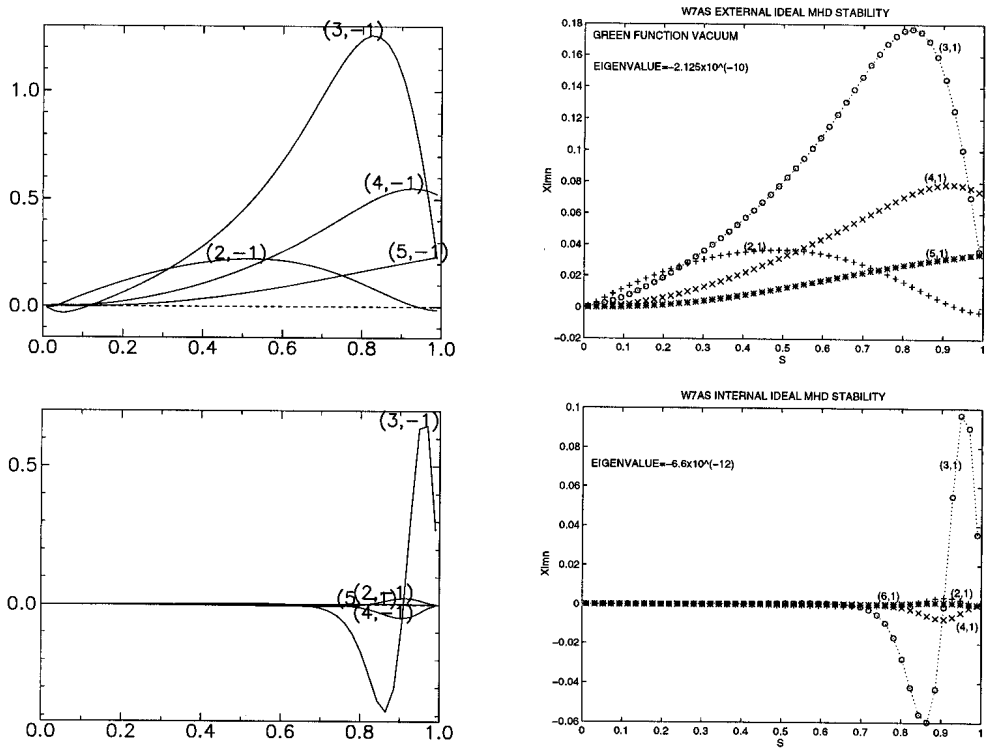


**Fig. 5.** *Comparison of perturbation structures obtained by the* TERPSICHORE *(right) and* CAS3D *(left) stability codes: For the most unstable case of the series ($B_Z/B_0 = 0.022$) the top frames show the Fourier coefficients of $\boldsymbol{\xi}\cdot\boldsymbol{\nabla}s$ versus the flux label $s$ resulting from the free-boundary calculation including the Green's function vacuum formulation; the bottom frames illustrate the corresponding fixed-boundary results, $\boldsymbol{\xi}\cdot\boldsymbol{\nabla}s = 0$ on the plasma boundary; here, the perturbation is clearly dominated by the $(3,-1)$ component. Only 4 out of 61 harmonics are shown.*

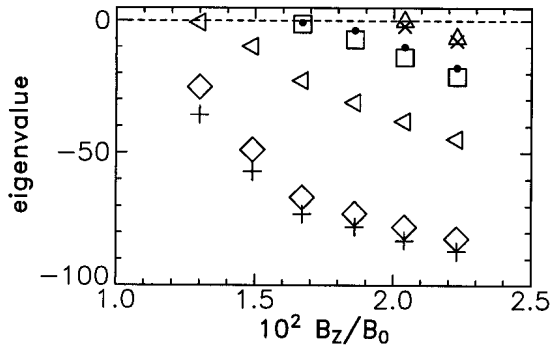


**Fig. 6.** *Eigenvalues (free-boundary: $10^{11}\lambda$, fixed-boundary: $10^{12}\lambda$) versus the ratio of vertical magnetic field to main field for the $(3,-1)$ perturbation in W7-AS equilibria.* TERPSICHORE *results: + for the free-boundary mode without vacuum energy, □ for the free-boundary mode with the Green's function vacuum energy ($N_s = 48$), △ for the fixed-boundary mode;* CAS3D *results: ◇ for the free-boundary mode without vacuum energy, • for the free-boundary mode with the Green's function vacuum energy ($N_s = 48$), ◁ as • but with $N_s = 192$, × for the fixed-boundary mode.*

criterion is satisfied. This behaviour is in contrast to the one found for the low-node-number fixed-boundary modes in low-shear stellarators [1], for which the Mercier stability limit sets the marginal point.

For the series investigated here the stability limit given by the $N = 1$ free-boundary modes is obtained for $B_Z/B_0 \approx 0.014$. Though the vacuum energy contribution itself is non-negative [compare Eq. (3)] and, therefore, stabilizing, the free-boundary modes may be more unstable in the same configuration, since there is no boundary condition on the plasma-vacuum interface. Here, the $N = 1$ free-boundary modes shift the fixed-boundary stability limit by $\approx -0.006$ in the ratio of vertical field to main field.

Figures 5 and 6 show the momentary status of the comparative calculations done with the TERPSICHORE and CAS3D codes. The eigenmode structures (see Fig. 5

for the $N = 1$ perturbation in the $B_Z/B_0 = 0.022$ case) and the corresponding eigenvalues (see Fig. 6) are in good agreement.

## V. CONCLUSIONS

The extension of the CAS3D stability code to the free-boundary stability problem was accomplished with the implementation of the Green's function approach for the vacuum energy. Advantages of the Green's function technique versus the pseudo-plasma vacuum treatment are, that there is no need to continue the coordinate system and the perturbation functions to the vacuum region. As a consequence the algebraic eigenvalue problem does not increase in size. Furthermore, an infinite vacuum region may be introduced, so that a 'wall' stabilization of the free-boundary modes can be avoided.

The application to a set of W7-AS configurations shows that, in contrast to the behaviour of the low-node-number fixed-boundary modes, free-boundary modes may be unstable in Mercier-stable configurations. Approximate vanishing of the field compression also applies to the free-boundary modes. The specific free-boundary modes treated here shift the fixed-boundary-mode stability limit by $\approx 0.006$ in the ratio of vertical field to main field

Corresponding results of the TERPSICHORE and CAS3D stability codes show good agreement for the perturbation structures and eigenvalues. The comparative work will be continued.

## ACKNOWLEDGMENTS

The authors appreciate continuous discussions with J. Nührenberg and would like to thank S. Gori for doing the equilibrium calculations.

[1] C. Schwab, Phys. Fluids B **5**, 3195 (1993).
[2] C. Nührenberg, Phys. Plasmas **3**, 2401 (1996).
[3] P. Merkel, J. Comput. Phys. **66**, 83 (1986).
[4] P. Merkel, Theory of Fusion Plasmas Varenna 1987, (SIF, Bologna), 25 (1988).
[5] S. P. Hirshman, W. I. van Rij, P. Merkel, Comput. Phys. Comm. **43**, 143 (1986).
[6] H. Renner *et al.*, *Plasma Physics and Controlled Nuclear Fusion Research 1990*, (IAEA, Vienna) **2**, 603 (1991).
[7] I. B. Bernstein, E. A. Frieman, M. D. Kruskal, and R. M. Kulsrud, Proc. Roy. Soc. Ser. A **244**, 17 (1958).
[8] K. Hain, R. Lüst, A. Schlüter, Z. Naturforsch. **12 a**, 833 (1957).
[9] A. H. Boozer, Phys. Fluids **25**, 520 (1982).
[10] J. Nührenberg, R. Zille, Theory of Fusion Plasmas Varenna 1987, (SIF, Bologna), 3 (1988).
[11] C. Schwab, Theory of Fusion Plasma Chèxbres 1988, (SIF, Bologna), 85 (1989).
[12] W. A. Cooper *et al.*, *Plasma Physics and Controlled Nuclear Fusion Research 1990*, (IAEA, Vienna) **2**, 793 (1991).
[13] R. Gruber *et al.*, Comput. Phys. Commun. **24**, 363 (1981).
[14] G. Y. Fu *et al.*, Phys. Fluids B **4**, 1401 (1992).
[15] J. Nührenberg *et al.*, in *Controlled Fusion and Plasma Physics 1993*, (IOP, Bristol), **35**, 115 (1993).
[16] A. Weller *et al.*, in *1992 Int. Conf. on Plasma Physics*, (Europhys. Conf. Abstracts, EPS), **1**, 549 (1992).

# Stable Bootstrap-Current Driven Equilibria for Low Aspect Ratio Tokamaks

R.L. Miller, Y.R. Lin-Liu, A.D. Turnbull, V.S. Chan,
*General Atomics, San Diego, California, U.S.A.*

L.D. Pearlstein
*Lawrence Livermore National Laboratory, Livermore, California, U.S.A*

O. Sauter, L. Villard
*CRPP/EPFL, Assoc. Euratom-Switzerland, Lausanne, Switzerland*

***Abstract***

Low aspect ratio tokamaks can potentially provide a high ratio of plasma pressure to magnetic pressure $\beta$ and high plasma current $I$ at a modest size, ultimately leading to a high power density compact fusion power plant. For the concept to be economically feasible, bootstrap current must be a major component of the plasma current. A high value of the Troyon factor $\beta_N$ and strong shaping are required to allow simultaneous operation at high $\beta$ and high bootstrap current fraction. Ideal magnetohydrodynamic stability of a range of equilibria at aspect ratio 1.4 is systematically explored by varying the pressure profile and shape. The pressure and current profiles are constrained in such a way as to assure complete bootstrap current alignment. Both $\beta_N$ and $\beta$ are defined in terms of the vacuum toroidal field. Equilibria with $\beta_N \geq 8$ and $\beta \sim 35\%$ to $55\%$ exist which are stable to $n = \infty$ ballooning modes, and stable to $n = 0,1,2,3$ kink modes with a conducting wall. The dependence of $\beta$ and $\beta_N$ with respect to aspect ratio is also considered.

Low Aspect Ratio Tokamaks (LATs) have received significant attention recently in part because of the experimental results from START[1] and the potential for tokamak operation at high plasma $\beta$, high plasma current, and modest size.[2] At low aspect ratio there is insufficient space on the inboard side of the tokamak for ohmic coils so non-inductive current drive will be required. Additionally, the large plasma currents characteristic of low aspect ratio will require prohibitive amounts of non-inductive current drive power unless a large fraction of the current can be maintained by the bootstrap current. Thus we are led to study the magnetohydrodynamic (MHD) stability of the high $\beta$, large bootstrap fraction regime.

The high bootstrap fraction, $f_{bs} = I_{bootstrap}/I_p$ requirement — the equilibria here have $f_{bs}$ in excess of 95% — constrains the current profile. Usually two independent plasma profiles determine an MHD equilibrium, *e.g.*, pressure and safety factor profiles. However, for high bootstrap fraction equilibria, the current profile is determined from the pressure profile alone; we use the collisionless model of Hirshman[3] to model the bootstrap current. A small amount of auxiliary current is required near the axis where the bootstrap current goes to zero.

Although ultra-low aspect ratios have been proposed,[2] Stambaugh *et al.*[4] show that given an assumed scaling of $\beta_N \propto 1/A$, the ratio of fusion power to Ohmic dissipation in the toroidal coil is maximized at $A = 1.4$. Although we present evidence that the scaling of $\beta_N$ with $A$ is weaker than $1/A$, suggesting larger optimal $A$ than 1.4 with respect to this criterion, we primarily focus on $A = 1.4$ in this paper.

Some appreciation of the parameters required to achieve simultaneous high $\beta$ and high bootstrap fraction can be seen from a simple relationship between $\beta$ and $\beta_p$. The Troyon scaling for MHD stable $\beta$ is given[5]

$$\beta = \frac{\beta_N}{100}\left(\frac{I}{aB}\right), \tag{1}$$

where $I$ is in megamps, $a$ is the minor radius in meters, $B$ is in tesla, and $\beta_N$ is in %-T-m/MA. At low $A$ it is particularly important to identify the $B$ used in this formula

and in the definition of $\beta$. We find that the above equation is best satisfied (*i.e.*, $\beta_N$ nearly a constant) using the vacuum $B$ field at the geometric axis of the outermost flux surface, $B_0$. The plasma $\beta$ is defined as the volume average of the pressure divided by the magnetic pressure due to this field

$$\beta = \frac{2\mu_0\langle p\rangle}{B_0^2} \ . \tag{2}$$

The poloidal $\beta$, $\beta_p$, is defined as the volume average of the pressure divided by the magnetic pressure due to an average poloidal field at the boundary

$$\beta_p = \frac{2\mu_0\langle p\rangle}{\overline{B}_p^2} = \frac{2\mu_0\langle p\rangle}{(\mu_0 I\, 10^6 / L_p)^2} \cong 25\left(\frac{1+\kappa^2}{2}\right)\frac{\beta_N}{100}\beta_N\left(\frac{aB_0}{I}\right) , \tag{3}$$

where we are still expressing $I$ in megamps and use the approximation

$$L_p = 2\pi\sqrt{\frac{1+\kappa^2}{2}}\, a \ , \tag{4}$$

for the poloidal circumference. Poloidal beta is a particularly important quantity in the present studies because the fraction of bootstrap current is proportional to $\beta_p$. Large $f_{bs}$ will require large $\beta_p$. Multiplying Eq. (1) by Eq. (3) we get the desired result

$$\beta\beta_p = 25\,\frac{1+\kappa^2}{2}(\beta_N/100)^2 \ , \tag{5}$$

where $\beta$ is now expressed as a number and not a percentage. This expression says that to achieve simultaneous high $\beta$ and high bootstrap fraction (high $\beta_p$) we need high $\beta_N$ and/ or high elongation.

The numerical study presented here assesses the MHD stability of high $\beta$, low $A$ equilibria for ideal infinite-$n$ ballooning modes and low $n$ kink modes. Additional details of some aspects may be found in Ref. 6. The low $n$ stability analysis has been done only for selected cases, including the highest $\beta$ cases. It appears, however, that for the beta range we study, the kink modes can be wall stabilized. Thus it is the ballooning mode which determines the $\beta$ limit, while kink stability is determining the required wall location. We scan over a range of elongations and triangularities and find an optimal triangularity of

about 0.4 while $\beta$ is still increasing with elongation up to the maximum $\kappa$ we studied of 3. The optimum triangularity can be understood from the constraint on full bootstrap alignment at the edge.

The equilibria for this study were generated using the flux-coordinate fixed boundary code TOQ.[7] This code can solve the Grad-Shafranov equation for a variety of different initial specifications. The code was recently modified and now uses a multigrid algorithm[8] to invert the elliptic operator. In this paper we specify pressure and the flux surface average of $\langle J \cdot B \rangle$ where $J$ is the plasma current and $B$ is the magnetic field. $\langle J \cdot B \rangle$ near the plasma axis is assumed to result from auxiliary current drive while $\langle J \cdot B \rangle$ away from the axis is prescribed as a constant and is entirely generated from bootstrap current as described below. The formula for the pressure gradient, $p' \equiv \partial p / \partial \psi$, is specified as a function of normalized poloidal flux $\tilde{\psi}$, where $\tilde{\psi}$ varies from 0 at the magnetic axis to 1 at the boundary. A polynomial form found to be near optimal in this study is given by

$$p' = C\left(0.025 + 0.975\ \tilde{\psi}^3 - \tilde{\psi}^4\right) , \tag{6}$$

where the constant $C$ is adjusted to give the desired $\beta$.

The primary contribution to $\langle J \cdot B \rangle$ is the bootstrap current. We use a simple model:

$$\langle J \cdot B \rangle_{\text{bootstrap}} = \mu_0 g(\tilde{\psi}) f p' \quad , \tag{7}$$

based on the collisionless theory of Hirshman[3] and described in more detail in Ref. 6. Here $f$ is the flux function given by the major radius $R$ times the toroidal field $B_T$, $f = RB_T$. We note in passing that the previously mentioned scaling $f_{bs} \propto \beta_p$ can be easily deduced from Eq. (7).

The infinite $n$ ballooning mode equation was solved using BALOO[7] and the low $n$ kink modes were analyzed using GATO.[9] The ballooning results were obtained by computing the marginal stable $\beta$ for equilibria with resolutions of $(N_\psi, N_\theta)$ = [(67,65), (131,129), (259,257)] and extrapolating the results to the marginally stable $\beta$ for infinite mesh size. Here $N_\psi$ and $N_\theta$ are the number of radial and angular mesh points, respectively. Some of the equilibrium and ballooning results were reproduced using the

Lawrence Livermore National Laboratory code TEQ, while some low $n$ kink results were confirmed using CHEASE[10] and ERATO.[11]

We first present equilibrium and stability results at $A = 1.4$ for a range of elongation, triangularity, temperature scale lengths, and $p'$ profiles. All of the equilibria are marginally stable to ballooning modes. Kink analysis has been done for only a few representative cases, including the highest $\beta$ cases. The case $\kappa = 3.0$, $\delta = 0.5$, and $p'$ given by Eq. (6) is shown in Fig. 1. The pressure profile across the midplane as a function of major radius is shown in Fig. 1(b). The $p'$ profile and $q$ profiles a function of $(\tilde{\psi})^{1/2}$ are shown in Fig. 1(c) and (d). The toroidal current density across the midplane as a function of major radius is shown in Fig. 2(a) and the peaking of the current density on the outboard midplane is quite striking. This is characteristic of LATs and is due to the strong variation of $B$ with $R$. Note also that the $q$ profile remains monotonic despite the off-axis peaking of the current density. The flux surface average $\langle JR_0 / R \rangle$ is shown in 2(b) to illustrate the total bootstrap alignment. The contributions to the "total bootstrap" current are shown individually as bootstrap, diamagnetic, and Pfirsch-Schluter contributions. The total bootstrap fraction for this equilibrium is 99% and the maximum stable $\beta_N$ is 8.28 The $\beta$ is 54% and $\beta_p$ is 1.63. A wall at 1.3 times the plasma radius is sufficient to stabilize these modes.

The variation of maximum stable $\beta_N$ and $\beta$ with respect to triangularity $\delta$ and elongation $\kappa$ are shown in Figs. 3 and 4. The Troyon factor $\beta_N$ is seen to increase with increasing elongation but the increase in $\beta$ is more dramatic because of the well-known increase in current $I$ with elongation. $\beta_p$ on the other hand is more nearly constant (Fig. 5) as a function of elongation and Eq. (5) shows in such a situation we expect $\beta$ to increase as $(1+\kappa^2)\beta_N^2$.

Somewhat surprisingly, Figs. 3 and 4 show a rather modest optimum triangularity. Ordinarily one would expect higher $\beta$ with increasing triangularity from stability arguments. However, increasing triangularity also reduces the trapped particle fraction and thus the bootstrap current. This reduction in bootstrap current illustrated in Fig. 6 will increase the magnetic shear at the edge. Since in the equilibria considered here $p'$ is

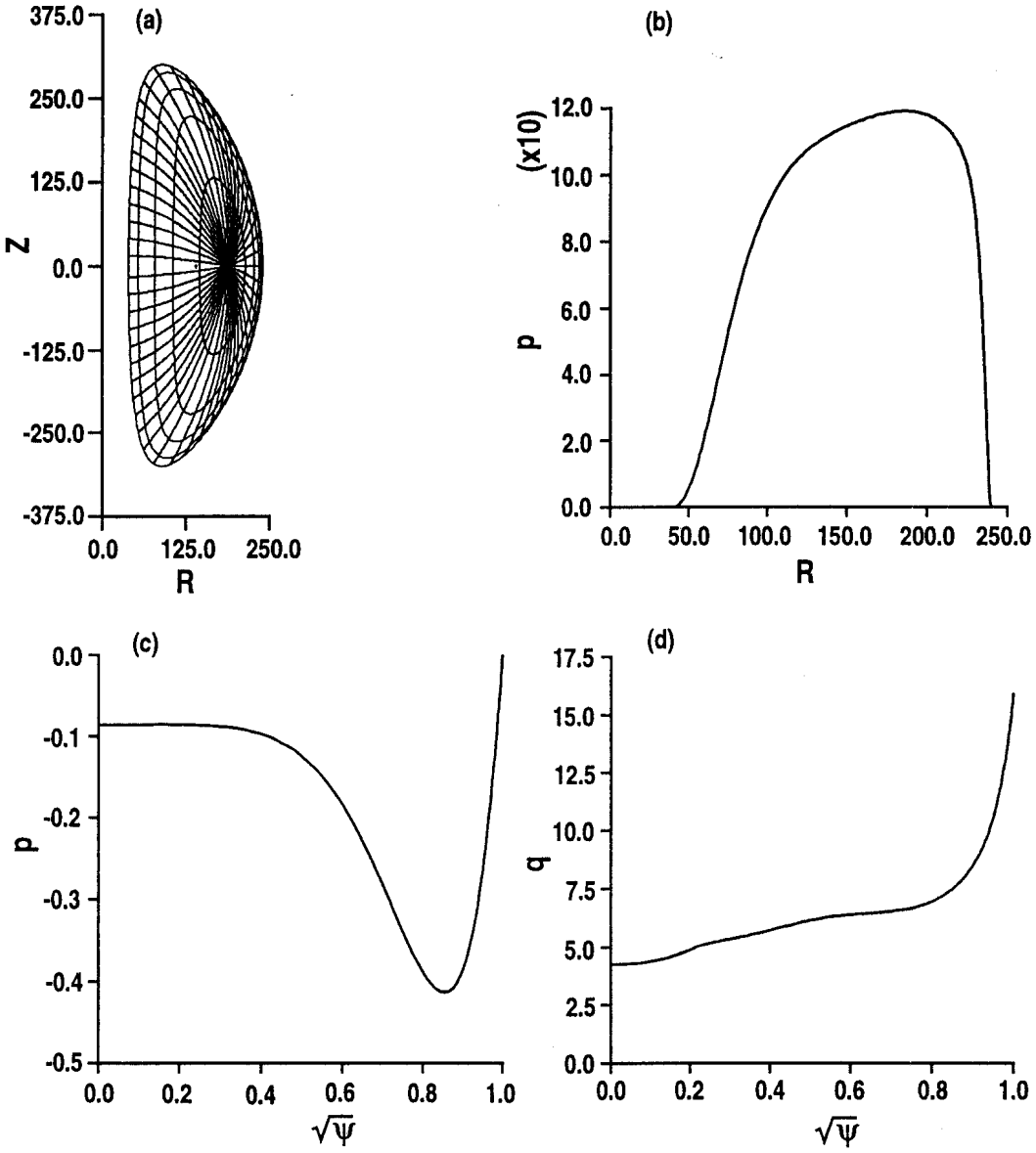


Fig. 1. Reference case equilibrium: $\kappa = 3.0$, $\delta = 0.5$, $L_p/L_T = 0.5$. (a) flux contours, (b) pressure profile across the midplane as a function of major radius, (c) $p'$ as a function of $(\tilde{\psi})^{1/2}$, (d) $q$ as a function of $(\tilde{\psi})^{1/2}$.

required to vanish at the plasma boundary, the larger magnetic shear will make the transition from the second stability region to the first regime more difficult, hence, the global $\beta$ limit is lowered. There is a tradeoff in triangularity effects between increasing the magnetic well and increasing the magnetic shear. This results in an optimum triangularity which increases modestly with elongation (see Fig. 3). For $\kappa = 2.5$, $\delta = 0.3$ to 0.4.

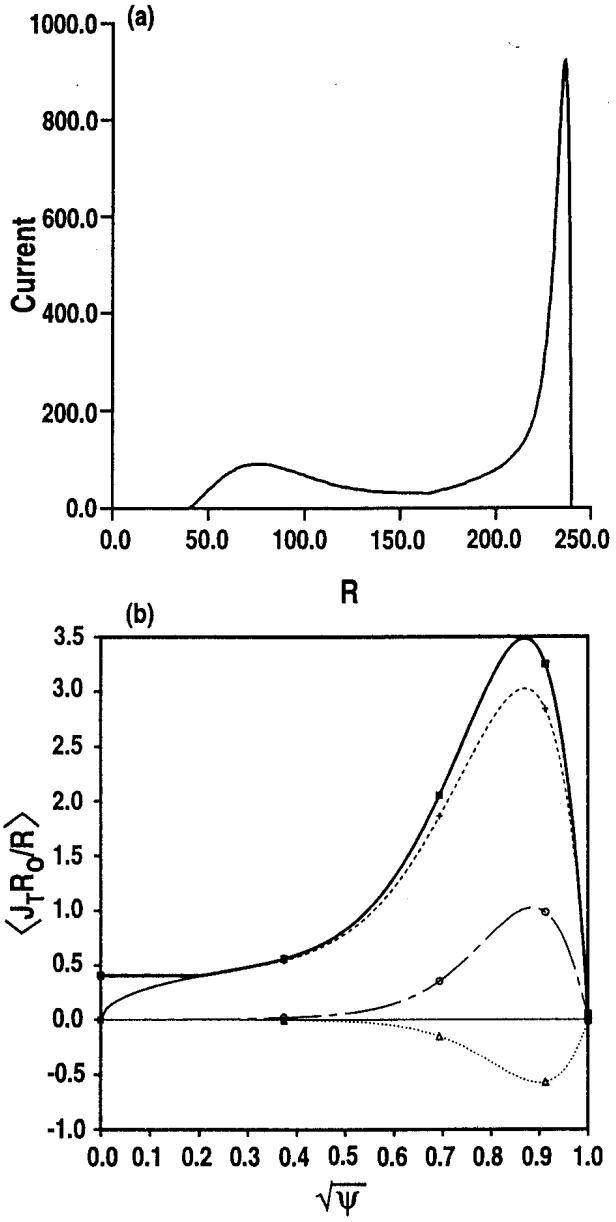


Fig. 2. Toroidal current density for equilibrium of Fig. 1. (a) toroidal current density across the midplane as a function of major radius and (b) $\langle JR_0/R \rangle$ versus $\tilde{\psi}$. The components of the "total bootstrap" current density are shown individually as bootstrap (dash), diamagnetic (long dash, short dash), and Pfirsch-Schluter contributions (dots).

Although the optimum triangularity is near 0.4, wall stabilization becomes easier as $\delta$ increases. For $\kappa = 3$, $r_{wall}/r_{plasma} = 1.15$ to stabilize $n = 1$, 2, and 3 at $\delta = 0.4$, while at $\delta = 0.5$, $r_{wall}/r_{plasma} \sim 1.3$. These wall locations are all adequate to stabilize the $n = 0$ mode for the respective equilibria.

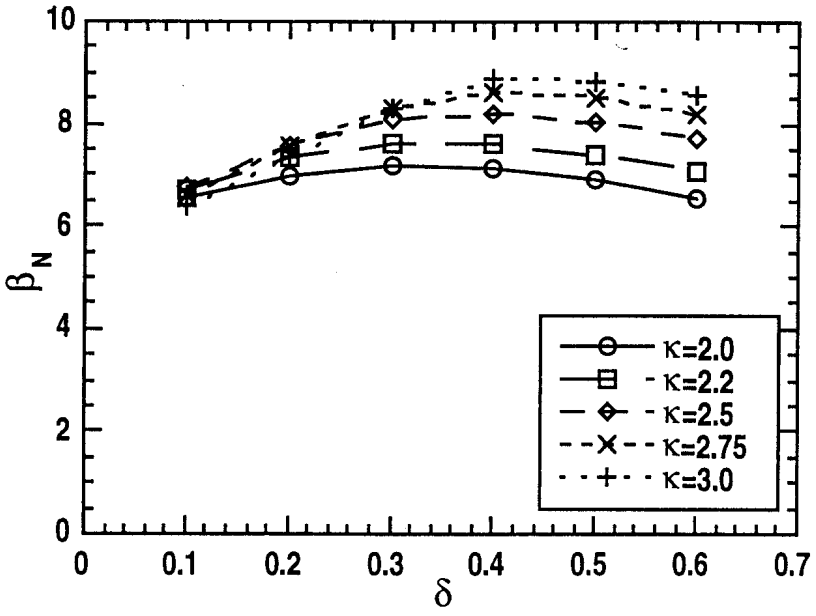


Fig. 3. Variation of $\beta_N$ with respect to triangularity $\delta$ for a range of elongations.

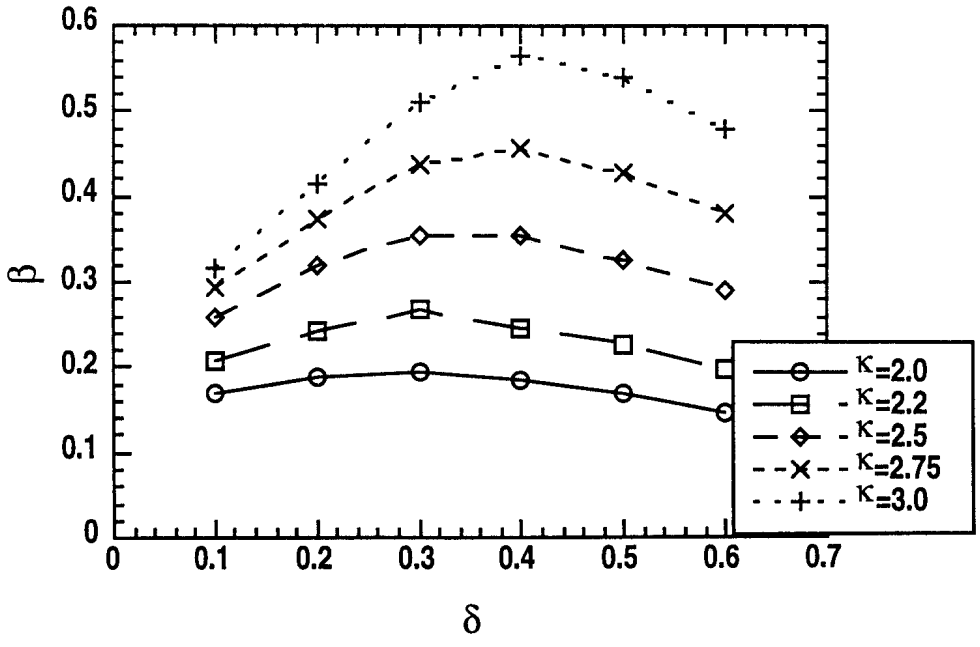


Fig. 4. Variation of $\beta$ with respect to triangularity $\delta$ for a range of elongations.

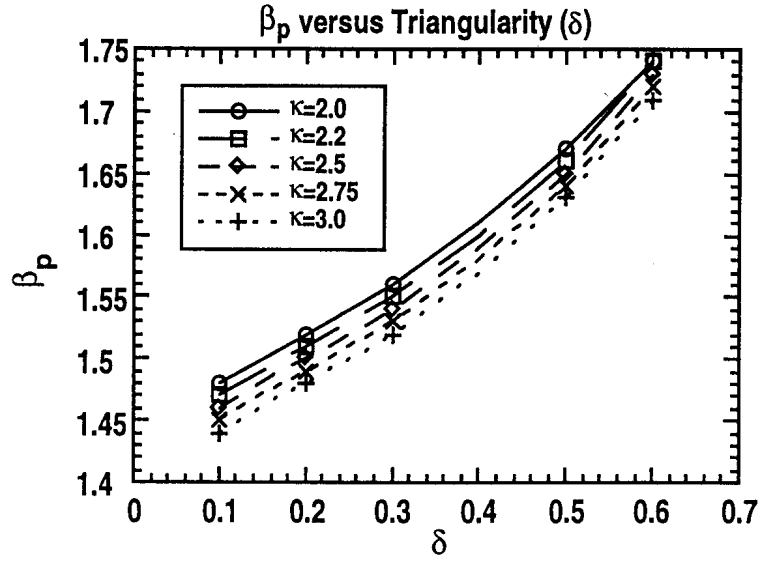


Fig, 5. $\beta_p$ increases modestly with increasing triangularity. This increase is necessary to maintain constant $f_{bs} \sim 100\%$.

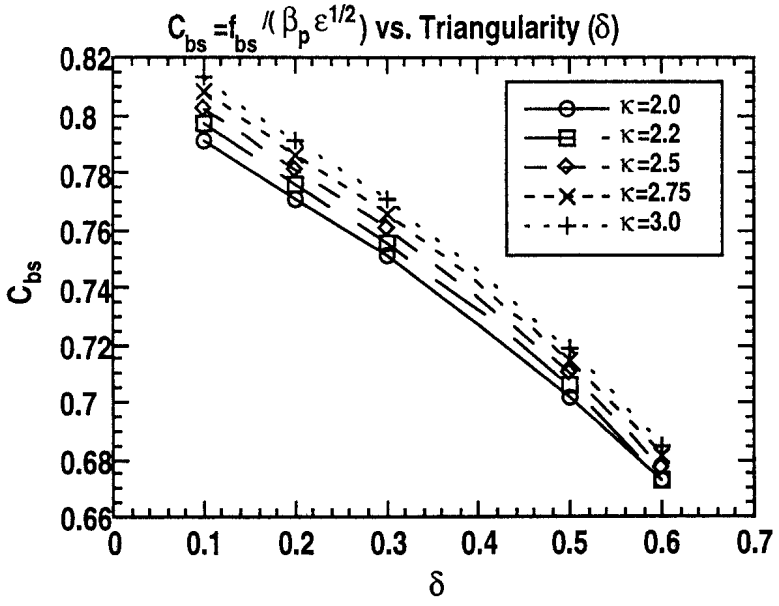


Fig. 6. The bootstrap coefficient $C_{bs} \equiv f_{bs}\sqrt{A}/\beta_p$ is seen to depend weakly upon elongation but decreases with triangularity. This higher $\beta_p$ is required at larger $\delta$ to maintain $f_{bs}$.

As mentioned in the previous section, Eq. (6) for $p'$ was found to be near optimal and Fig. 7 shows partial evidence for that. Here $p'$ is parameterized as

$$p' = C\left(0.025 + 0.975\,\tilde{\psi}^n - \tilde{\psi}^{n+1}\right),$$

and $n$ is varied from 1 to 4. The maximum magnitude of $p'$ occurs at $\tilde{\psi} = 0.975n/(n+1)$. The advantage of pushing the maximum towards the edge of the plasma is apparent from Fig. 7. The two different values of on-axis seed current in Fig. 7 show the advantage of raising $q$ on axis. Note that $q_{\text{axis}} \propto 1/\langle J \cdot B\rangle_{\text{axis}}$. Further reductions of seed current beyond that shown produce almost no effect.

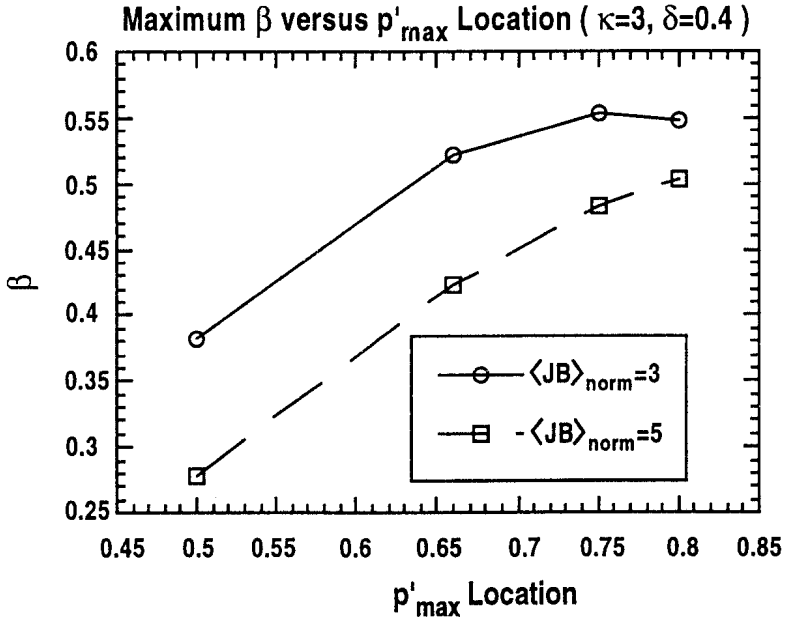


Fig. 7. Variation of $\beta_N$ and $\beta$ with respect to location of maximum $p'$ for $\kappa = 3$ and $\delta = 0.4$. $\langle J \cdot B\rangle_{\text{norm}} \equiv \langle J \cdot B\rangle_{\text{axis}}\, a / B_0^2$.

It is also of interest to ask what limits the ballooning $\beta$ to the values observed in this paper. This issue is addressed in Ref. 6 where $s - \alpha$ diagrams[12] are presented. It is shown that if $p'$ is allowed to be finite at the edge of the plasma, as is routinely found in equilibrium reconstruction of DIII–D data,[13] that $\beta_N \geq 10$ is possible. The equilibrium is in that case everywhere in the second stable regime.

Finally we consider the dependence of $\beta$ and $\beta_N$ upon aspect ratio. An attempt to study other $A$'s in as much detail as we have devoted to $A = 1.4$ would require extensive searches to determine an optimal $p'(\psi)$ at each $A$. We have taken the far more modest course of examining only ballooning stability and only for the $p'$ profile given by Eq. (6) for $A$ ranging from 1.2 to 2.8. We looked at a range of triangularities from 0.2 to 0.6 and at elongations of 2, 2.5, and 3. The results are shown in Figs. 8 and 9. Because we did not modify the profiles as we varied $A$, $f_{bs}$ falls off somewhat for some of the higher $A$ cases but is still always in excess of 80%. The triangularity yielding the highest $\beta$ does not vary much at $A$ Even at $A = 2.8$ it is $\sim 0.44$ at $\kappa = 2$ and $\sim 0.52$ at $\kappa = 3$.

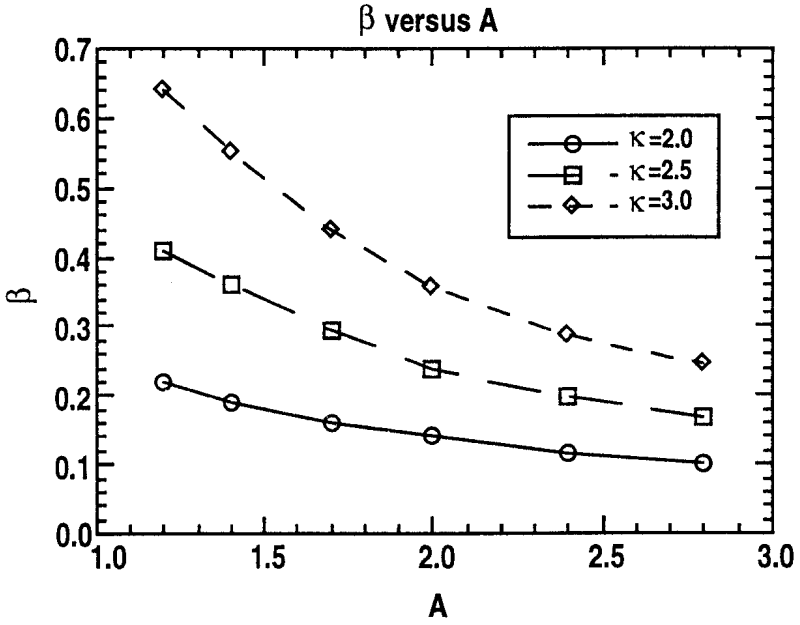


Fig. 8. Variations of $\beta$ with respect to $A$ for a range of elongations. Ballooning stability only.

Figures 8 and 9 show that higher elongation yields higher $\beta$ and even higher $\beta_N$ at every aspect ratio considered. The magnitude of $\beta_N \sim 6$ at $A = 2.8$ for $\kappa = 2$ is content with previous stability calculations[14] in this parameter regime despite the large $\beta_p$'s (1.7 to 2 at $A = 2.8$) being considered here. Also the fact that $\beta_N(A = 1.2) > \beta_N(A = 1.4)$ even though $p'$ was not optimized for $A = 1.2$ strongly suggests that $\beta_N$ increases with decreasing $A$. Nevertheless, the reader is reminded of the limitations of this restricted optimization and, in particular, that wall stabilization of the kink at reasonable wall

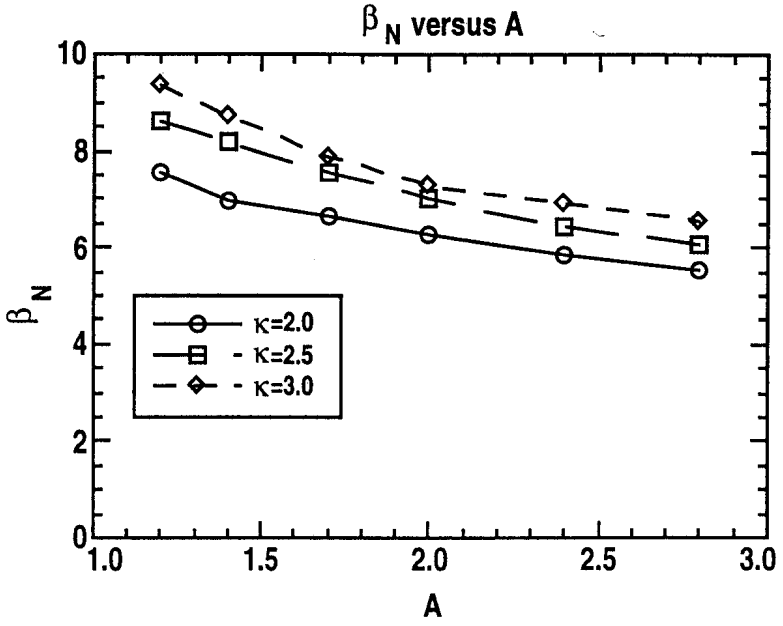


Fig. 9. Variations of $\beta_N$ with respect to $A$ for a range of elongations. Ballooning stability only.

distances has not yet been demonstrated except at $A = 1.4$.In summary, we have explored the dependence of $\beta$ and $\beta_N$ on shape and pressure profile for the high $\beta$ high bootstrap fraction tokamak regime at $A = 1.4$. We find with $f_{bs} \sim 99\%$ that ballooning mode instabilities limit $\beta_N$ to the rather high range of $\sim 8$ with $p' = 0$ at the plasma edge. The cases examined for kink stability indicate that these modes can be wall-stabilized. The case with $\kappa = 3.0$ and $\delta = 0.5$ had $\beta = 55\%$. A triangularity of $\delta \sim 0.4$ is optimal while $\beta$ increases significantly with elongation to the highest elongation studied ( $\kappa = 3$).

This study is a step towards determining shapes and profiles at low aspect ratio to yield high $\beta$ and high bootstrap fraction. Issues which remain to be addressed include: creating high $\beta$ strongly shaped free-boundary equilibria with a realistic field-shaping coil set, determining optimum pressure profiles consistent with a transport model, exploring effects of collisionality in the bootstrap current model, and assessing the need for current profile control.

This is a report of work sponsored by the U.S. Department of Energy under Grant No. DE-FG03-95ER54309 and Contract No. W-7405-ENG-48, and in part by the Swiss National Science Foundation.

## References

1. A. Sykes, Plasma Phys. and Contr. Fusion **35**, 1051 (1993).
2. Y.-K.M. Peng *et al.*, in *Plasma Physics and Controlled Nuclear Fusion Research* (Proc. 15th Int. Conf. Seville, 1994) (International Atomic Energy Agency, Vienna, 1995) Vol. 2, p. 643.
3. S.P. Hirshman, Phys. Fluids **31**, 3150 (1988).
4. R.D. Stambaugh *et al.*, "The Spherical Tokamak Path to Fusion Power," General Atomics Report GA-A22226, to be submitted to Fusion Technology.
5. F. Troyon *et al.*, Plasma Phys. and Contr. Fusion **26**, 209 (1984).
6. R.L. Miller *et al.*, "Stable Equilibria for Bootstrap-Current Driven Low Aspect Ratio Tokamaks," General Atomics Report GA-A22321, submitted to Physics of Plasmas.
7. R.L. Miller and J.W. VanDam, Nucl. Fusion **28**, 2101 (1987).
8. P.M. de Zeeuw, Centre for Mathematics & Computer Science, P.O. Box 4079, 1009 AB Amsterdam, The Netherlands.
9. L.C. Bernard *et al.*, Comput. Phys. Commun. **24**, 377 (1981).
10. H. Lütjens, A. Bondeson, and A. Roy, Comput. Phys. Commun. **69**, 287 (1992).
11. R. Gruber *et al.*, Comput. Phys. Commun. **21**, 323 (1981).
12. J.M. Greene and M.S. Chance, Nucl. Fusion **21**, 453 (1981).
13. P. Gohil *et al.*, Phys. Rev. Lett. **61**, 1603 (1988); L.L. Lao *et al.*, Plasma Phys. Contr. Fusion **31**, 509 (1989).
14. W. Howl *et al.*, Phys. Fluids B **4**, 1724 (1992).